Study on Cross Section Generation for BWR Pin-by-Pin Core Analysis

February 2015

Tatsuya FUJITA

Study on Cross Section Generation for BWR Pin-by-Pin Core Analysis

Contents

Figures

Tables

Chapter 1. Introduction

1.1. Background

In current core analysis using the advanced nodal method, calculations are carried out through three steps, (*i.e.*, a pin-cell, a lattice and a core calculations). At first, a pin-cell calculation is carried out and effective microscopic cross sections are calculated in a heterogeneous pin-cell geometry, in which about one hundred energy groups are used. Then, a lattice calculation using the transport calculation method, (*e.g.*, the current coupling collision probability (CCCP) method and the method of characteristics (MOC)), is carried out in heterogeneous structure of a fuel assembly using the several to several dozen energy group cross sections obtained in the previous step [1, 2]. Such heterogeneous cross sections are homogenized in a fuel assembly and the number of energy groups is reduced to 1 to 3. Finally, a core calculation is carried out, in which assembly homogenized cross sections with a few energy group are used.

In the above procedure, cross sections, which are necessary for core analysis, are approximately treated from the viewpoints of state variables of a core, neutron energy, and spatial distribution of neutron flux as follows:

(1) Core state variables

Cross sections provided to a core calculation depend on many state variables and their histories during depletion, (*e.g.*, exposure, void fraction, control rod position, and their histories). In order to generate cross sections at each core state throughout an operation cycle, calculations of cross sections for the all possible combinations of the state and history variables are desirable. However, such calculations would be unrealistic from the viewpoint of the computational time. Therefore, in the current core analysis, assembly averaged cross sections are calculated for the limited combinations of the state and history variables in lattice physics calculations, and are tabulated for the state and history variables in prior to a core calculation. Then, in a core calculation, cross sections are reconstructed from the tabulated cross section set with the state and history variables corresponding to the core state.

(2) Neutron energy

Cross sections depend on neutron energy. In order to exactly capture such dependence of cross sections, several tens of thousands of energy groups should be used in a core calculation. However,

such calculations are impractical from the viewpoint of the computational time. Therefore, in the current core analysis, the number of energy groups is reduced as the calculation geometry becomes large as described above.

(3) Spatial distribution of neutron flux

Coarse group cross sections for a core calculation are obtained by collapsing fine group cross sections through a lattice calculation in a single assembly geometry. However, in a core calculation, the spectral interference effect due to adjacent loading of different types of fuel assemblies, (*e.g.*, UO2 and mixed-oxide (MOX) fuel assemblies), should be taken into account. Coarse group cross sections are different in a single assembly and a core geometries since energetic and spatial distributions of neutron spectrum are different in these geometries due to the spectral interference effect. Therefore, in the current core analysis, the spectral index (SI), which is the ratio of fast to thermal neutron fluxes, has been traditionally used to correct coarse group cross sections [3].

Moreover, although cross sections are calculated on heterogeneous structure of a fuel assembly in a lattice calculation, they are homogenized in a fuel assembly and a fuel assembly is treated as homogeneous manner in a core calculation. Therefore, in order to estimate the detail pin-power distribution, the pin-power reconstruction method, which synthesizes the global smooth power distribution in a homogeneous node and the heterogeneous pin-by-pin power distribution obtained by the lattice physics calculation, is used [4, 5]. However, the accuracy of this method might be degraded in highly heterogeneous cores such as MOX fuel or high burn-up fuel loaded cores.

Recently, the pin-by-pin fine mesh core calculation method for BWR core analysis has been studied as a candidate of the next generation core analysis method [6, 7]. In this method, cross sections are homogenized in a fuel pin-cell. The pin-by-pin power distribution can be directly estimated and thus can reduce the error with the homogenization of cross sections. Therefore, the important core parameters, (*e.g.*, power peaking factor), would be more accurately calculated. However, there are some crucial issues to be addressed in order to apply the pin-by-pin fine mesh core calculation method for BWR core analysis in practical utilizations.

Tada focused on the neutronics and the thermal-hydraulic calculations in the pin-by-pin BWR core analysis [8]. He studied on the applicability of the simplified P3 (SP3) theory for the pin-by-pin BWR core analysis and confirmed the improvement of calculation accuracies compared with the

diffusion theory [9]. He also studied about treatment of staggered mesh, which is caused by existence of several geometries of fuel assemblies and is a specific issue for the pin-by-pin BWR core analysis. Moreover, he applied a quick sub-channel thermal-hydraulic analysis method on the pin-by-pin BWR core analysis. From his valuable efforts, several issues on practical application of the pin-by-pin fine mesh core calculation method for BWR core analysis were solved.

However, from the viewpoints of treatment of cross sections in core calculations, several unresolved issues still remain.

(1) Establishment of appropriate energy group structure

In the previous study, the pin-by-pin fine mesh core calculation method for BWR core analysis, in which 8-group structure is used, showed good accuracy to evaluate important parameters for highly heterogeneous cores [6, 7]. However, the number of energy groups and the energy group structure suitable for the pin-by-pin core analysis have not been fully investigated yet. Especially, there is significant energetic and spatial variation of neutron spectrum in BWR fuel assemblies since they have complicated geometries. Therefore, a generation method of appropriate energy group structure for the BWR pin-by-pin fine mesh core calculation is desirable.

(2) Development of cross section set

A cross section set has an important role from the viewpoints of calculation accuracy, required memory, and computational time in the pin-by-pin fine mesh core calculation method. However, the pin-by-pin fine mesh core calculation method requires large size of a cross section set since cross sections are independently tabulated for each pin-cell mesh. For PWR, pin-by-pin core analysis codes with a practical tabulation method have been developed [10]. On the other hand, for BWR, an efficient pin-by-pin tabulation method has not been investigated since a BWR fuel assembly has much more complicated geometries and neutronics behavior than those of PWR, (*e.g.*, large water rods, large enrichment splitting, large water gaps between fuel assemblies, and a control blade). Therefore, an efficient tabulation method is necessary.

(3) Consideration of spectral interference effect

Use of finer energy group structure enables to capture significant variation on energetic and spatial distribution of neutron spectrum in a BWR fuel assembly due to its complicated geometries.

However, number of energy groups would be limited due to computation time. Thus a correction method for cross section considering the spectral interference effect is still necessary when approximately 10 energy groups are used in core analysis. Unfortunately, the conventional spectral interference correction technique using SI, which is based on an engineering or an empirical approach, would not be valid for the BWR pin-by-pin calculations with finer energy group. Therefore, a new correction technique for variation of coarse group cross sections due to the spectral interference effect should be proposed for the BWR pin-by-pin calculations.

1.2. Overview of conventional boiling water reactor (BWR) core analysis

1.2.1. Outline of core analysis

In order to confirm the safety of designed core, several parameters (*e.g.*, core reactivity and power peaking factor) should be evaluated in BWR core analyses. Then, appropriate macroscopic cross sections, which are determined by types of fuel assemblies, neutron energies, and core state and depletion history parameters, are necessary as input datum for core analysis. However, macroscopic cross sections strongly depend on such parameters. For example, fuel assemblies have complicated geometries such as fuel pellets and claddings (*i.e.*, spatial heterogeneity). Microscopic cross sections of heavy nuclides strongly depend on neutron energy such as their behavior in resonance regions (*i.e.*, energetic dependency). Assembly-averaged exposures relate to nuclide compositions of fuel pins such as ^{235}U or Pu-fissile enrichments. Moreover, the core state and the depletion history parameters (*e.g.*, void fraction, fuel temperature, moderator temperature, and their histories) become different by loading patterns of fuel assemblies, control rod insertions during core operations, and so on. Thus, direct core analyses considering core geometries and state parameters are impractical since preparation of appropriate macroscopic cross sections is difficult from the viewpoint of computational time and required memory.

Therefore, in the conventional BWR core analysis, two types of calculations (*i.e.*, lattice physics and core calculations) are performed and cross section sets are tabulated in several conditions using the results of lattice physics calculations. The tabulated cross section set is provided to core calculations. During generation of the cross section set, spatial and energetic dependencies of cross sections are approximated (*i.e.*, spatial homogenization and energy collapsing are performed). The overview of conventional BWR core analysis is shown in **Figure 1.1**.

The details of lattice physics calculation, cross section set, and core calculation are shown in sections 1.2.1.1 to 1.2.1.3, respectively. The mathematical descriptions of spatial homogenization and energy collapsing are shown in section 1.2.2.

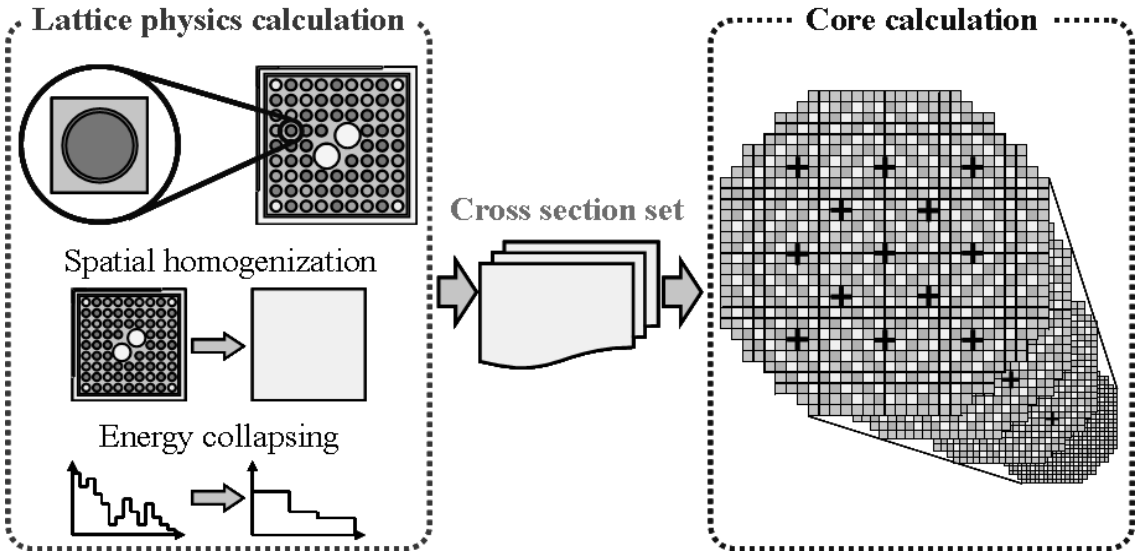

Figure 1.1 Overview of conventional BWR core analysis

1.2.1.1. Lattice physics calculation

The overview of lattice physics calculation is shown in **Figure 1.2**. As shown in Figure 1.2, in prior to lattice physics calculation, the evaluated nuclear data library (*e.g.*, JENDL-4.0 and ENDF-B/VII.1) is converted into a cross section library by a nuclear data processing code (*e.g.*, the NJOY code) [11-13]. The lattice physics calculations are carried out using the cross section library, where following information is required as input datum:

- Geometry of fuel assembly (*e.g.*, radius of fuel pin and thickness of channel box),
- Fuel pin enrichment of ^{235}U or Pu-fissile,
- Moderator density,
- Structure compositions,
- Fuel, moderator, and structure temperatures,
- Power density,
- Burnup step (assembly-averaged exposure),

and so on.

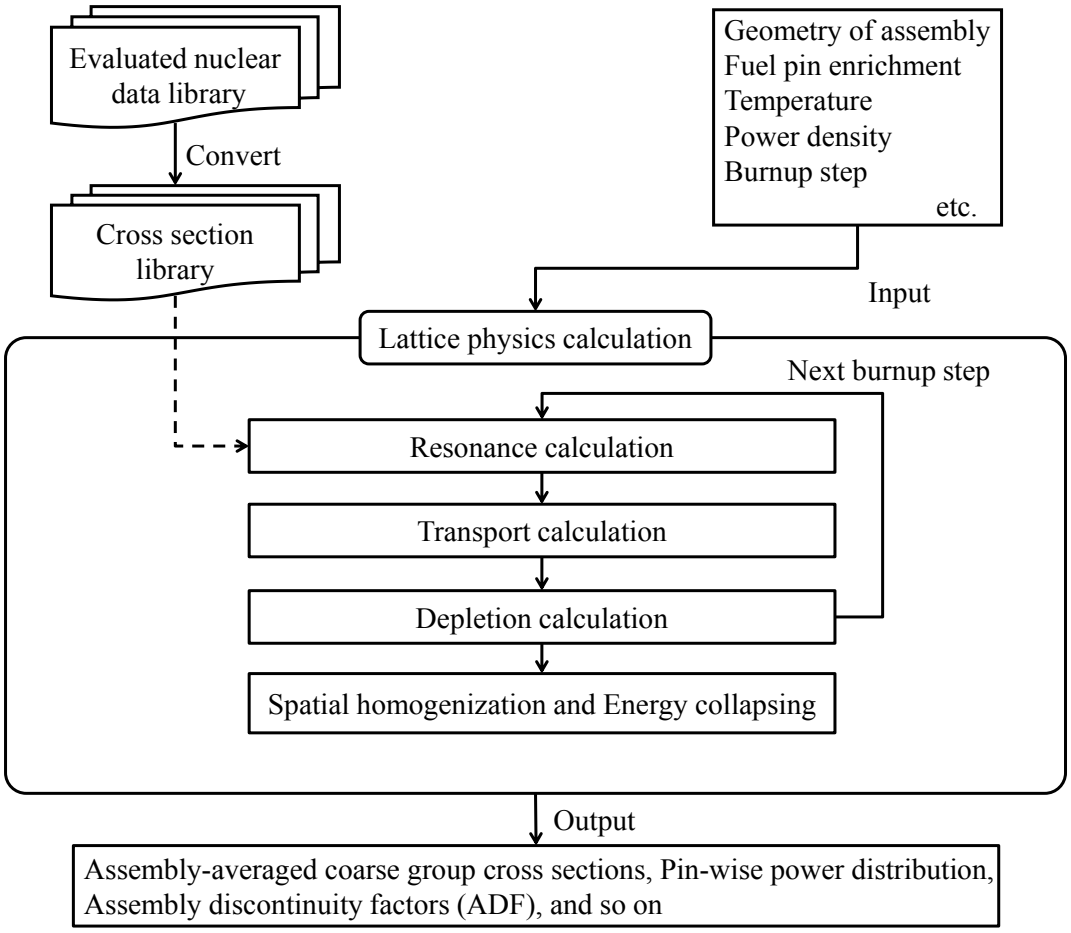

Figure 1.2 Overview of lattice physics calculation

In lattice physics calculations, firstly, resonance calculations are carried out to obtain effective microscopic cross sections. Then, neutron transport calculations, which are based on the MOC, are usually performed in single assembly geometries with the reflective boundary condition. Through the neutron transport calculations, fine group neutron fluxes are calculated in heterogeneous geometry. Next, by using the neutron fluxes, depletion calculations are performed to estimate the variations of nuclide components due to burnup of fuel assembly. Finally, macroscopic cross sections are averaged in fuel assembly and then they are collapsed into coarse group.

Through the lattice physics calculations, the following information is obtained at each burnup step as output datum:

- Assembly-averaged coarse group cross sections,
- Effective fission yields and number densities of ^{135}Xe and ^{149}Sm,
- Pin-wise power distribution,
- Exposure distribution,

- Assembly discontinuity factors (ADF),

and so on.

1.2.1.2. Cross section set

A cross section set provides assembly-averaged parameters (*e.g.*, coarse group cross sections) for core analyses.

In order to estimate core behaviors, macroscopic cross sections are necessary in core calculations. However, they depend on many parameters in a complicated manner:

- Exposure of fuel assemblies,
- Core parameters (void fraction, fuel temperature, moderator temperature, and control rod position),
- Depletion histories,
- Spatial and energetic distributions of neutron fluxes,

and so on. Therefore, it is not useful to prepare macroscopic cross sections considering all combinations of core conditions from the viewpoint of the computational loads.

It should be noted that there are two main different points on the calculation conditions between the lattice physics and the core calculations. The first point is the treatment of state parameters (*e.g.*, the void fraction, the fuel temperature, the moderator temperature, and the control rod). In the core calculations, such state parameters varies during the depletion of fuel assemblies. However, since such changes of state parameters depend on the loading pattern of fuel assemblies and the core operation, it is not practical to consider them in the lattice physics calculations from the viewpoint of the computational loads. Thus, the particular combinations of state parameters are considered in the lattice physics calculations, where the state parameters are assumed to be consistent with various operating conditions of a core. The second point is the calculation geometries. In the core calculations, many different types of fuel assemblies (*e.g.*, the low- and the high-enrichment or the flesh and the spent fuel assemblies) are loaded into a target core. When the different types of fuel assemblies are adjacently loaded in a core, the neutron spectrum of fuel assemblies interfere with each other and become different from those in single assembly geometries (*i.e.*, the lattice physics calculations). However, since the loading pattern of fuel assemblies is unknown in to the stage of lattice physics calculations, such interference of neutron spectrum cannot be simulated in the lattice physics

calculations. Thus, by combining several calculation results of lattice physics calculations, interference of neutron spectrum are corrected in the core calculations.

In order to tabulate a cross section set, two types of lattice physics calculations (*i.e.*, the depletion and the branch calculations) are performed.

In the depletion calculations, state parameters (*e.g.*, the void fraction, the fuel temperature, the moderator temperature, and the control rod) are constant during burnup and, and the neutron fluxes and the number densities are calculated in each burnup steps.

In the branch calculations, the number densities are not calculated and those obtained through the depletion calculations are used. In each burnup steps, state parameters are partially changed from those in the depletion calculations, and the neutron fluxes are recalculated. The concept of the branch calculation is shown in **Figure 1.3** [14].

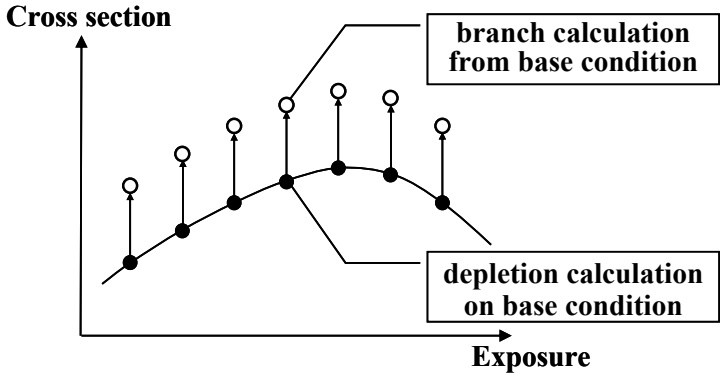

Figure 1.3 Concept of branch calculation

Let me show the simple example of tabulation of cross sections set. For example, cross sections are tabulated for the void fraction and the control rod position. In this case, the depletion and the branch calculations shown in **Table 1-1** are used.

Table 1-1 Depletion and branch calculation cases (void fraction (VOI) and control rod (CR) position)

No.	CR	VOI[%]	Depletion/Branch
0	out	40.0	Depletion(Base condition)
1	out	0.0	Branch from No. 0
2	out	70.0	Branch from No. 0
3	in	0.0	Branch from No. 0
4	in	70.0	Branch from No. 0
5	out	0.0	Depletion
6	out	70.0	Depletion
7	in	0.0	Depletion
8	in	70.0	Depletion

By combining these calculation results, which are obtained through the depletion and the branch calculation cases shown in Table 1-1, the cross sections are interpolated for the void fraction and the control rod. The overview of the interpolation of the cross sections is shown in **Figure 1.4**.

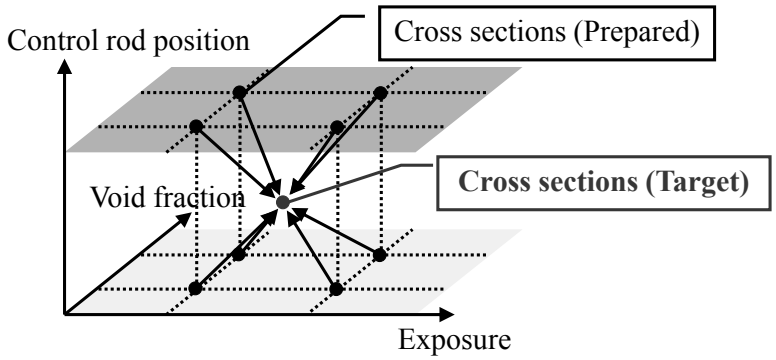

Figure 1.4 Overview of interpolation of cross sections

1.2.1.3. Core calculation

The overview of core calculation is shown in **Figure 1.5**.

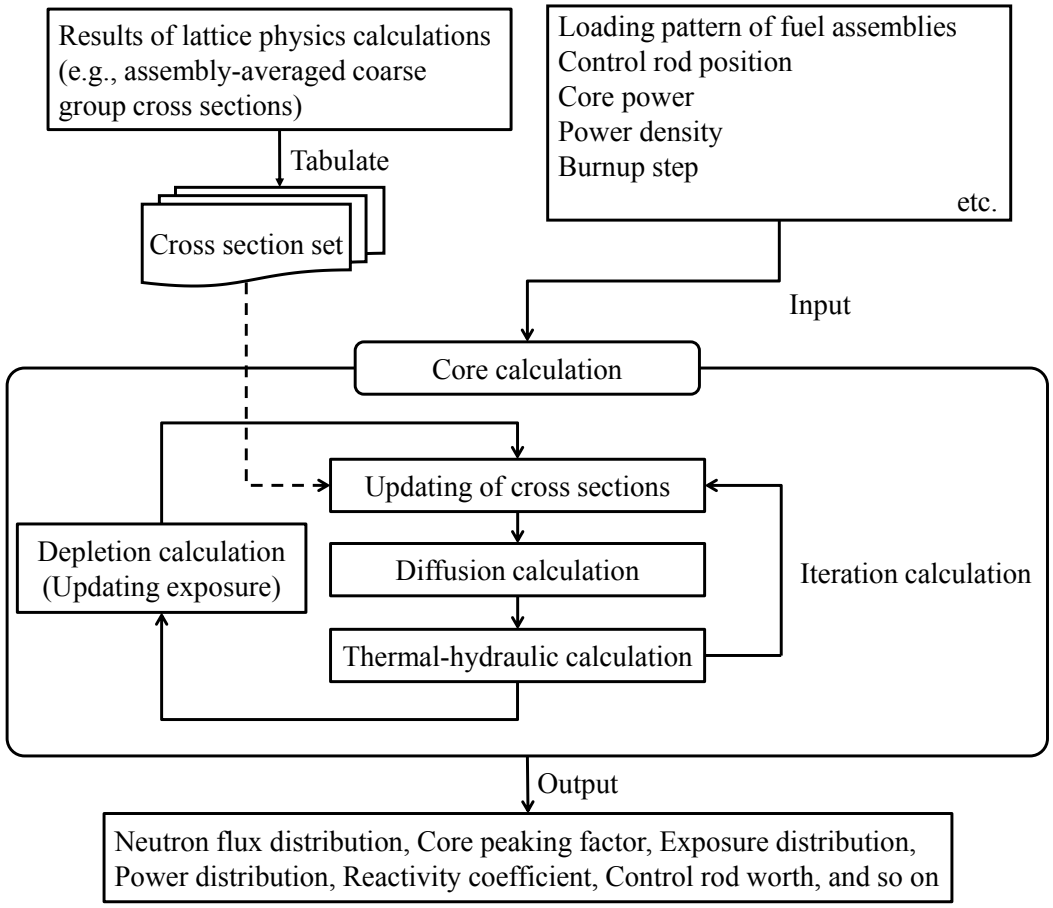

Figure 1.5 Overview of core calculation

As shown in Figure 1.5, in prior to core calculation, the cross section set is tabulated by calculations results in lattice physics calculations (*e.g.*, assembly-averaged coarse group cross sections, assembly discontinuity factors), which is described in section 1.2.1.2. The core calculations are carried out using the cross section set, where following information is required as input datum:

- Loading pattern of fuel assemblies,
- Control rod position,
- Core power,
- Power density,
- Burnup step (assembly-averaged exposure)

and so on.

In core calculations, firstly, cross sections are interpolated from the cross section set. Then, neutron diffusion calculations are performed in core geometries. Through the neutron diffusion calculations, power distributions are obtained. Next, by using the power distributions, the

thermal-hydraulic calculations are performed to calculate distributions of void fraction, fuel temperature, and moderator temperature. By the distributions of void fraction, fuel temperature, and moderator temperature, cross sections are updated from the cross section set. Update of cross sections, the neutron diffusion calculation, and the thermal-hydraulic calculations are iteratively performed until the calculation results (*e.g.*, the neutron flux distribution, the core peaking factor, and the reactivity coefficient) are converged. Finally, the exposures of fuel assemblies are calculated using the power distribution and burnup time.

Through the core calculations, following information is obtained at each burnup step as output datum:

- Neutron flux distribution,
- Core peaking factor,
- Exposure distribution,
- Power distribution,
- Reactivity coefficient,
- Control rod worth,

and so on.

1.2.2. Averaging of cross section

1.2.2.1. Spatial homogenization

In the lattice physics calculations, heterogeneous cross sections are homogenized for a fuel assembly as shown in **Figure 1.6**. Homogenized cross sections are used in core calculations.

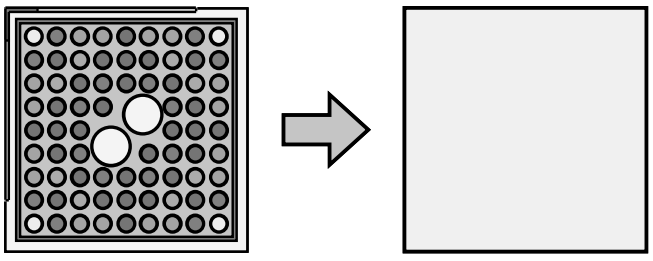

Figure 1.6 Homogenization of cross sections in the conventional advanced nodal method

The homogenization of cross sections are performed to preserve the reaction rates as:

$$\Sigma_{x,g,M} = \frac{\sum_{m \in M} \Sigma_{x,g,m} \phi_{g,m} V_m}{\sum_{m \in M} \phi_{g,m} V_m}, \tag{1.1}$$

$$\Sigma_{s,g \to g',M} = \frac{\sum_{m \in M} \Sigma_{s,g \to g',m} \phi_{g,m} V_m}{\sum_{m \in M} \phi_{g,m} V_m}, \tag{1.2}$$

$$\chi_{g,M} = \frac{\sum_{fm \in M} \chi_{fm,g} \left(\sum_{g'} \nu \Sigma_{f,fm,g'} \phi_{fm,g'} V_{fm} \right)}{\sum_{fm \in M} \sum_{g'} \nu \Sigma_{f,fm,g'} \phi_{fm,g'} V_{fm}}, \tag{1.3}$$

where, Σ, χ, ϕ, and V are the macroscopic cross section, the fission spectrum, the neutron flux, and region volume, respectively. The subscripts of x, g, m, fm, and M represent the reaction type (*e.g.*, fission and absorption), the energy group index, the heterogeneous region index, the heterogeneous fuel region index, and the homogeneous region index, respectively.

1.2.2.2. Energy collapsing

In the lattice physics calculations, several to several dozen energy group cross sections are used to calculated the neutron fluxes. Such fine energy groups are collapsed into coarse energy groups as shown in **Figure 1.7**.

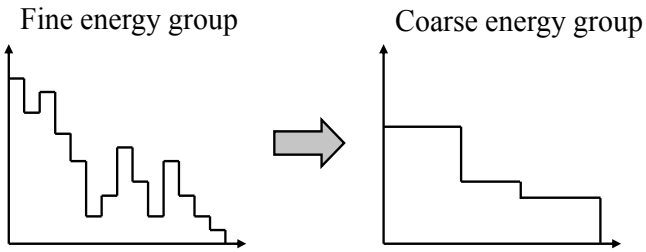

Figure 1.7 Energy collapsing of cross sections

The energy collapsing of cross sections are also performed to preserve the reaction rates as:

$$\Sigma_{x,G} = \frac{\sum_{g \in G} \Sigma_{x,g} \phi_g}{\sum_{g \in G} \phi_g}, \tag{1.4}$$

$$\Sigma_{s,G \to G'} = \frac{\sum_{g \in G} \sum_{g' \in G'} \Sigma_{s,g \to g'} \phi_g}{\sum_{g \in G} \sum_{g' \in G'} \phi_g}, \tag{1.5}$$

$$\chi_G = \sum_{g \in G} \chi_g , \tag{1.6}$$

where, Σ, χ, and ϕ are the macroscopic cross section, the fission spectrum, and the neutron flux, respectively. The subscripts of *x*, *g*, and *G* represent the reaction type (*e.g.*, fission and absorption), the fine group index, and the coarse group index, respectively.

1.3. Pin-by-pin fine mesh core analysis

1.3.1. Overview

The pin-by-pin fine mesh core calculation method, in which the cross sections are homogenized in each pin-cell, has been studied as a candidate of the next generation core analysis method. It can directly estimate the detailed pin-power distribution. Since the spatial homogenization is carried out only for pin-cell as shown in **Figure 1.8**, it is expected that the error associated with the spatial homogenization of cross sections will be reduced. Therefore, crucial core parameters (*e.g.*, power peaking factor) would be more accurately calculated with the pin-by-pin core analysis method.

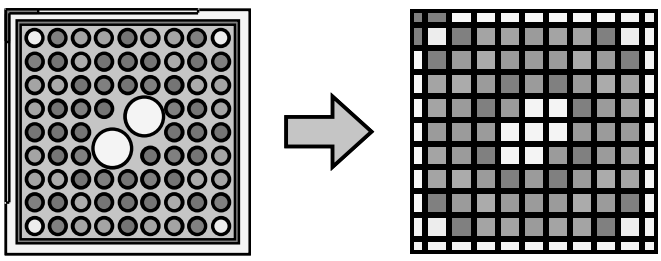

Figure 1.8 Homogenization of cross sections in the pin-by-pin fine mesh core calculation method

1.3.2. Issue of application on BWR pin-by-pin core analysis

There are some crucial issues to be addressed for practical application of the pin-by-pin fine mesh core calculation method for BWR core analysis.

Firstly, an appropriate energy group structure for the BWR pin-by-pin fine mesh core calculation should be establised. In the previous study, the pin-by-pin fine mesh core calculation method with 8 energy groups showed good accuracy for highly heterogeneous BWR cores. However, the number of energy groups and the energy group structure suitable for the pin-by-pin core analysis have not been fully investigated yet. Especially, in BWR, there is significant energetic and spatial distribution of neutron spectrum in a fuel assembly due to complicated geometries.

Secondly, the efficient and accurate tabulation method is a crucial issue. In the pin-by-pin fine mesh core calculation method, a cross section set has an important role from the viewpoints of calculation accuracy, required memory, and computational time. However, the pin-by-pin fine mesh core calculation method requires large size of a cross section set since cross sections are independently tabulated for each pin-cell mesh. For PWR, pin-by-pin core analysis codes with a practical tabulation method have been developed. However, for BWR, an efficient pin-by-pin tabulation method has not been investigated since a BWR fuel assembly has much more complicated geometries than those of PWR, (*e.g.*, large water rods, large enrichment splitting, large water gaps between fuel assemblies, and a control blade).

Finally, a new correction technique for variation of coarse group cross sections due to the spectral interference effect should be proposed for the BWR pin-by-pin calculations. Though spectral interference effect can be naturally incorporated by utilization of finer energy groups, number of energy groups is limited from the viewpoint of computational resources. Thus a correction method for cross section is still necessary. It should be reminded that the conventional SI correction method cannot be directly applied to the fine mesh BWR core analysis method since it adopts finer energy groups and spatial resolution.

1.4. Purpose of this thesis

In this thesis, the following three topics for BWR pin-by-pin fine mesh core calculation are addressed:

(1) An optimization approach to establish an appropriate energy group structure.

(2) A macroscopic depletion model to tabulate pin-cell averaged cross sections.

(3) A spectral interference correction technique for finer group cross sections.

In the first topic "An optimization approach to establish an appropriate energy group structure", I propose a new numerical approach, which is based on the steepest descent method to establish an appropriate energy group structure for the BWR pin-by-pin fine mesh core calculation. For this topic, the following points are investigated:

- Successive optimization approach to establish energy group structure
  - Optimization index
  - Number of candidates considered in successive procedure
- Relationship between number of energy group and calculation accuracy
- Performance of successive optimization approach

In the second topic "A macroscopic depletion model to tabulate pin-cell averaged cross sections", I focus on the fundamental development of the macroscopic cross section model for the BWR pin-by-pin core calculation method. For this topic, the following points are investigated:

- Macroscopic cross section model
  - Treatment of instantaneous effect
  - Treatment of history effect
- Verification for treatment of instantaneous and history effects
  - Impact of each instantaneous or history effect
  - Impact of cross-term effect among instantaneous or history effect

In the third topic "A spectral interference correction technique for coarse group cross sections", I focus on the spectral interference effect on the energy collapsing and propose a new correction technique for the coarse group cross sections, which is based on the generalized perturbation theory. Moreover, I combine the new correction technique, which reproduce the reference coarse group cross sections, and the superhomogenization (SPH) and the discontinuity factors (DF), which are used to reduce the energy collapsing error, For this topic, the following points are investigated:

- New correction technique using leakage index
  - Reproduction of reference coarse group cross sections
  - Comparison of calculation accuracies between different energy groups
- Combination of new correction technique with SPH factor or DF
  - Impacts of each technique on calculation accuracies
  - Comparison of calculation accuracies between new correction technique with SPH factor and that with DF

1.5. Contents of this thesis

This thesis adresses the crucial issues in practical application of the pin-by-pin fine mesh core calculation method for BWR core analysis. Detail explanations of the optimization approach to establish an appropriate energy group structure are described in Chapter 2. Chapter 3 is devoted for the establishment of pin-wise macroscopic cross section model and the investigations on impacts of instantaneous and history effects in the macroscopic cross sections. In Chapters 4 and 5, development of new correction technique for coarse group cross sections due to the spectral interference effect is described. The mathematical descriptions and the performance of new correction technique are shown in Chapter 4. Investigations on the combination of new correction technique with the SPH factor or the DF, followed by the numerical verifications, are shown in Chapter 5. Finally, conclusions are written in Chapter 6.

Reference

[1] M. Tatsumi, A. Gihou, T. Takeda, "Space and Angular Dependence of Interface Currents in the Multiband-CCCP Method," *J. Nucl. Sci. Technol.*, **37**[7], pp. 572-580, (2000).

[2] J. R. Askew, "A Characteristics Formulation of the Neutron Transport Equation in Complicated Geometries," *AEEW-M1108*, UKAEA, Winfrith, (1972).

[3] S. Palmtag, K. Smith, "Two-Group Spectral Corrections for MOX Calculations," *Proc. Int. Conf. on Physics of Reactors (PHYSOR98)*, Oct. 5-8, 1998, Long Island, New York, (1998). [CD-ROM].

[4] K. R. Rempe, K. S. Smith, "SIMULATE-3 Pin Power Reconstruction: Methodology and Benchmarking," *Nucl. Sci. Eng.*, **10**, pp. 334-342, (1989).

[5] T. Iwamoto, M. Yamamoto, "Pin Power Reconstruction Methods of the Few-Group BWR Core Simulator NEREUS," *J. Nucl. Sci. Technol.*, **36**[12], pp. 1141-1152, (1999).

[6] K. Tada, A. Yamamoto, Y. Yamane *et al.*, "Applicability of the Diffusion and Simplified P3 Theories for Pin-by-Pin Geometry of BWR," *J. Nucl. Sci. Technol.*, **45**[10], pp. 997-1008, (2008).

[7] K. Tada, A. Yamamoto, Y. Yamane, "Treatment of Staggered Mesh for BWR Pin-by-Pin Core Analysis," *J. Nucl. Sci. Technol.*, **46**[2], pp. 163-174, (2009).

[8] K. Tada, *Study on Pin-by-Pin Fine Mesh Core Calculation Method for BWR Core Analysis*, Ph.D. Thesis, Nagoya University, (2012).

[9] E. W. Larsen, J. E. Morel, J. M. McGhee, ''Asymptotic derivation of the multigroup P1 and simplified PN equations with anisotropic scattering,'' *Nucl. Sci. Eng.*, **123**, pp.328-342, (1996).

[10] M. Tatsumi, A. Yamamoto, "Advanced PWR Core Calculation Based on Multi-group Nodal-transport Method in Three-dimensional Pin-by-Pin Geometry," *J. Nucl. Sci. Technol.*, **40**[6], pp. 376-387, (2003).

[11] K. Shibata, O. Iwamoto, T. Nakagawa *et al*, "JENDL-4.0: A new library for nuclear science and technoliogy," *J. Nucl. Sci. Technol.*, **48**[1], pp. 1-30, (2011).

[12] M. B. Chadwicka, M. Hermanb, P. Obložinský *et al*, "ENDF/B-VII.1 Nuclear Data for Science and Technology: Cross Sections, Covariances, Fission Product Yields and Decay Data," *Nucl. Data Sheets*, **112**, pp. 2887-2996, (2011).

[13] R. E. MacFarlane, D. W. Muir, *The NJOY Nuclear Data Processing System, Version 91*, LA-12740-M, Los Alamos National Laboratory, (1994).

[14] K. Okumura, T. Kugo, K. Kaneko *et al*, *SRAC2006: A Comprehensive Neutronics Calculation Code System*, JAEA-Data/Code 2007-004, Japan Atomic Energy Agency, (2007).

Chapter 2. A optimization approach to establish an appropriate energy group structure

2.1. Introduction

Nuclear cross sections strongly depend on neutron energy (*e.g.*, their behaviors in resonance regions). In order to directly capture such energy dependence of cross sections, several tens of thousands of energy groups should be used in core calculations. However, such ultra-fine group calculations are impractical for core calculations from the view point of the computational time and the required memory. Therefore, in a conventional core analysis, the number of energy groups is reduced as the calculation geometry becomes large.

In the current BWR core analysis using the advanced nodal method, mostly three-step calculation (*i.e.*, pin-cell, lattice, and core calculations) are carried out. At first, in a pin-cell calculation, dozens to a few hundred energy groups are used and effective microscopic cross sections are calculated. The number of energy groups of the effective microscopic cross sections is reduced to several to several dozen in prior to a lattice calculation. Then, a lattice calculation is carried out in heterogeneous fuel assembly geometry with several to several dozen energy group the cross sections obtained in the previous step. Heterogeneous cross sections are homogenized within a fuel assembly and the number of energy groups is reduced to a few numbers. Finally, a core calculation is carried out with a few energy groups using the assembly homogenized cross sections obtained in the previous step [1, 2]. In general, the energy group structures used in the above calculations have been empirically determined.

In a highly heterogeneous core (*e.g.*, a mixed-oxide (MOX) fuel or a high burn-up fuel loaded core), the spatial behavior of neutron spectrum becomes more complicated. Therefore, in order to accurately capture such complicated neutron spectrum variation and to precisely evaluate important core parameters (*e.g.*, core reactivity and power peaking factor), various efforts have been devoted to improve core calculation methods. For example, a sub-meshing of fuel assembly or an on-the-fly boundary condition adjustment through iteration of lattice physics calculations has been studied [3, 4]. In the sub-meshing of fuel assembly, each fuel assembly is divided into N×N homogenized rectangular meshes in core calculations while each fuel assembly is homogenized into a 1×1 mesh in conventional BWR core calculations. In the on-the-fly boundary condition adjustment, heterogeneous assembly calculations with

albedo boundary conditions are performed and the homogeneous cross sections are recalculated in core calculations (*i.e.*, lattice physics calculations are embedded into core calculations).

For the highly heterogeneous core calculation, a finer energy group structure is desirable to accurately consider the spatial variation of neutron spectrum. However, if the number of energy groups becomes larger, the determination of an appropriate energy group structure based on an engineering or an empirical approach would become more difficult due to the large freedom on the choice of energy group boundaries. For example, when an 8 energy group structure is determined by collapsing a 40 energy group structure, there are approximately 15 million possible combinations of the energy group structure. Therefore, to establish a theoretical or a numerical approach is necessary to determine an appropriate energy group structure for core calculations.

Recently, a pin-by-pin approach is studied and is applied for BWR core calculations as a candidate of the next generation core analysis methods [5-8]. However, the number and the structure of energy groups, which are suitable for the pin-by-pin core analysis, have not been extensively investigated yet. For example, the validity of the 8-group structure used in the previous study for the BWR pin-by-pin core analysis are not fully confirmed [5, 6]. Especially, in BWR, there is a significant variation of energetic and spatial distribution in neutron spectrum in a fuel assembly since BWR fuel assemblies have complicated geometries (*e.g.*, a large water rod/channel, a large enrichment splitting, and a control blade). Therefore, it is necessary to establish an appropriate energy group structure for the BWR pin-by-pin fine mesh core calculation.

In recent studies, various theoretical and numerical approaches to determine an appropriate energy group structure have been investigated. For example, a multi-group cross section collapsing code YGROUP has been developed as a theoretical approach [9]. In this code, the “contribution” theory is used to directly construct an optimum coarse energy group structure. In the contribution theory, the forward and adjoint fluxes in fine energy groups are used to estimate contributions from fine groups (*i.e.*, the importance of the fine groups) and then the coarse energy group boundaries are chosen so as the summation of the fine group contributions in each coarse energy group are approximately same [10]. In addition, for an example of the numerical approaches, an adaptive energy mesh constructor has been developed for a lattice physics analysis [11]. In this work, in order to construct an optimum coarse energy group structure, the particle swarm optimization is applied to estimate the performances of

several coarse energy group structures. The neutron flux is approximately estimated during the optimization process.

In this Chapter, I propose a numerical approach, which is based on the steepest descent method to establish an appropriate energy group structure for the BWR pin-by-pin fine mesh core calculation. The present approach has three main features, which are different from the previous works:

(1) The target energy group structure is constructed through a successive calculation (*i.e.*, a successive collapsing or expanding of cross sections). Here the successive collapsing or expanding means that the number of energy groups is reduced or increased one by one, respectively.

(2) The difference of the k-infinity or the pin-by-pin fission rate distribution due to energy collapsing is directly used as an optimization index since the k-infinity and the pin-by-pin fission rate distribution are important to evaluate important core parameters (*e.g.*, core reactivity and power peaking factor).

(3) The appropriate energy group structures for various numbers of energy groups are suggested by the present approach.

This Chapter focuses on the development of an optimization algorithm to establish an appropriate coarser energy group structure. Therefore, a sensitivity analysis and a verification calculation are carried out in simple configurations instead of actual full core configurations. In this context, the applicability of the coarse energy group structure is not fully verified for actual cores. In practical application, the coarse energy group structure will be established by the present approach by considering fuel types that are loaded in the target cores.

The remainder of this Chapter is organized as follows. In section 2.2, some theoretical descriptions related to this Chapter (*i.e.*, the cause of energy collapsing error and the calculation procedure of the proposed methodology) are described. In this Chapter, I use 2×2 multi-assembly geometries, in which different types of fuel assemblies (*e.g.*, UO_2 and MOX fuel assemblies) are adjacently loaded, to establish an appropriate energy group structure and to verify the applicability of the present approach. In section 2.3, I compare and discuss the calculation results obtained by the present approach with various calculation conditions (*e.g.*, difference of the calculation procedure (collapsing or expanding)). In section 2.4, appropriate energy group structures are established by the present approach

considering various 2×2 multi-assembly geometries. Performance of the established energy group structures are confirmed under various lattice conditions. Finally, conclusions and remarks are shown in section 2.5.

2.2. Methodology

2.2.1. Energy collapsing error due to spectral interference effect

There are two major reasons for the energy collapsing error of the cross sections. These are briefly reviewed in this section.

One reason for the energy collapsing error of the cross sections is explained from the viewpoint of the preservation of reaction rates in single assembly geometry.

Multi-group cross sections used in a core calculation are obtained by collapsing fine group cross sections through a lattice physics calculation in single assembly geometry as follows:

$$\Sigma_{x,G} = \frac{\sum_{g \in G} \Sigma_{x,g} \phi_g}{\sum_{g \in G} \phi_g} . \tag{2.1}$$

In Equation (2.1), Σ and ϕ are the macroscopic cross section and the neutron flux, respectively. The subscripts of x, g, and G represent the reaction type (*e.g.*, fission and absorption), the fine group index, and the coarse group index, respectively. In general, a neutron flux obtained in a coarse group calculation is not identical to the summation of fine group neutron fluxes as follows:

$$\phi_G \neq \sum_{g \in G} \phi_g . \tag{2.2}$$

Therefore, reaction rates obtained by a coarse group calculation do not exactly reproduce reference (fine) reaction rates obtained by a fine group calculation as follows:

$$\Sigma_{x,G} \phi_G \neq \sum_{g \in G} \Sigma_{x,g} \phi_g . \tag{2.3}$$

In Equations (2.2) and (2.3), neutron fluxes obtained in a coarse group and a fine group calculations are normalized (*e.g.*, the system total absorption reaction rates are equal to unity).

In order to mitigate the error of reaction rates due to the energy collapsing, the superhomogenization (SPH) method is utilized in this Chapter [12]. By using the SPH method, reaction rates obtained by a coarse group calculation can be consistent with those obtained by a fine group calculation in a single assembly geometry as follows:

$$\mu_G \Sigma_{x,G} \phi_G = \sum_{g \in G} \Sigma_{x,g} \phi_g \,. \tag{2.4}$$

In Equation (2.4), μ is the SPH factor and is calculated by

$$\mu_G = \frac{\sum_{g \in G} \phi_g}{\phi_G}. \tag{2.5}$$

The other reason for the energy collapsing error of the cross sections is explained from the viewpoint of the existence of the spectral interference effect on multi-assembly geometry.

Reaction rates are preserved by using the SPH method in a single assembly geometry as described in the previous section. However, in a multi-assembly or a core geometry, the spectral interference effect among fuel assemblies should be taken into account since different types of fuel assemblies (*e.g.*, UO_2 and MOX fuel assemblies) are adjacently loaded. Due to the spectral interference effect, the neutron spectrum in a multi-assembly or a core geometry is different from that in a single assembly geometry.

For example, as shown in **Figure 2.1**, let us assume the 2×2 multi-assembly geometry, which consists of UO_2 (9×9 with two large water rods) and MOX (10×10 with a large water channel) fuel assemblies, with the perfect reflective condition. The variation of the neutron spectrum between the single assembly and the 2×2 multi-assembly geometries is calculated by

$$\Delta_i = \sqrt{\frac{\sum_{g=1}^{40}\left(w_{i,g}^{multi} - w_{i,g}^{single}\right)^2}{40}}, \tag{2.6}$$

and is qualitatively shown in **Figure 2.2**. In Equation (2.6), Δ is an index to represent the variation of neutron spectrum. The subscripts of i and g represent the mesh and the energy group indexes, respectively. The superscripts *single* and *multi* represent the results obtained by the single assembly and the 2×2 multi-assembly calculations, respectively. w is the neutron flux, which is normalized in each mesh, and is defined by

$$w_{i,g} \equiv \frac{\phi_{i,g}}{\sum_{g=1}^{40}\phi_{i,g}}. \tag{2.7}$$

The single assembly and the 2×2 multi-assembly calculations are performed in 40 energy groups.

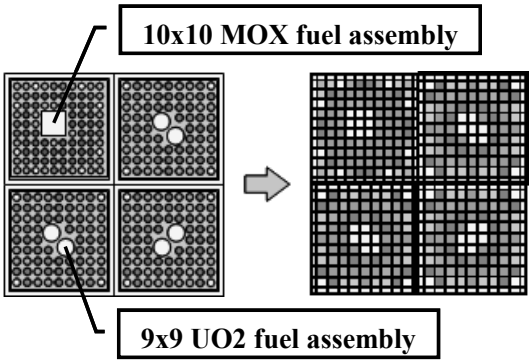

Figure 2.1 Geometry of 2×2 multi-assembly

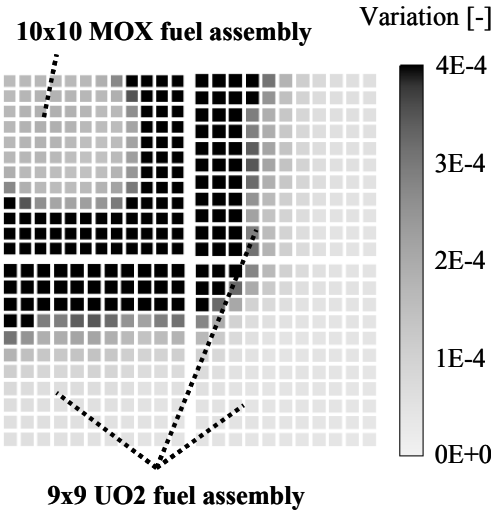

Figure 2.2 Variation of neutron spectrum due to spectral interference effect

As shown in Figure 2.2, the variation of the neutron spectrum is mainly observed in the assembly peripheral regions. Such spectral interference effect is the one of the main reasons for the energy collapsing error of the cross sections and it should be considered to establish an appropriate energy group structure.

The insertion of the control blade significantly affects the neutron spectrum in the core geometry. In order to appropriately consider the insertion of the control blade, larger geometries (*e.g.*, 4×4 multi-assembly geometries) may be necessary. However, in this Chapter, I focus on the spectral interference effect among fuel assemblies. When the control blade is inserted, neutrons are absorbed by the control blade that is located among fuel assemblies. Thus the spectrum interference effect becomes smaller when the control blade is inserted. Due to the above reason, the insertion of the control blade is not considered in this Chapter and the 2×2 multi-assembly geometry is used.

2.2.2. Optimization procedure

2.2.2.1. Overview

The energy collapsing error can be eliminated in a single assembly geometry by using the SPH method that can preserve reaction rates in each region. However, the spectrum interference effect in a multi-assembly geometry cannot be taken into account by using the SPH method since the SPH factor shown in Equation (2.5) is usually calculated in a lattice calculation assuming a single assembly geometry. Therefore, in order to establish an appropriate energy group structure, the variation of the

coarse group cross sections due to the spectrum interference effect in a multi-assembly geometry should be taken into account.

This Chapter has the following three features. Firstly, both of the calculation results, which are obtained before and after energy collapsing conditions, are considered to exactly capture the variation of the reaction rates. Namely, not only finer group calculations but also coarser group calculations are carried out to directly estimate the variation of the reaction rates. Secondly, the difference of the k-infinity or the pin-by-pin fission rate distribution due to the energy collapsing is directly used as an index to construct an appropriate energy group structure. Finally, the energy group structures for various number of energy groups are provided through the calculations based on the present approach.

In this Chapter, I propose two different methods to establish an appropriate energy group structure. The first one is the successive decreasing of the number of energy groups from fine to coarse (*i.e.*, the successive "collapsing" of cross sections). Let us assume the number of energy groups at the current calculation step is N. In the successive collapsing method, the differences of the k-infinity or the pin-by-pin fission rate distribution in a multi-assembly geometry between an (N-1)-group calculation and a reference (fine) group calculation are compared to establish an appropriate (N-1)-group structure. Another is the successive increasing of the number of energy groups from coarse to fine (*i.e.*, the successive "expanding" of cross sections). In the successive expanding method, the differences of the k-infinity or the pin-by-pin fission rate distribution between an (N+1)-group calculation and a reference (fine) group calculation are compared to establish an appropriate (N+1)-group structure. The details of these methods are described in the following sections.

The present approach may provide different energy group structures from the conventional ones. Such results might suggest a potential drawback of the conventional energy group structures for the BWR pin-by-pin fine mesh core analysis. Therefore, no additional constraint, which forces to adjust the energy boundaries to the conventional ones, is taken into account.

2.2.2.2. Successive collapsing method

Firstly, I describe the detail of the successive collapsing method. In the successive collapsing method, the number of energy groups is decreased one by one from the reference (fine) group to the coarse group by removing an energy group boundary and the cross sections are collapsed into fewer

energy groups. In this Chapter, starting from 40 groups, the number of energy groups are reduced to 39, 38, 37, ..., 4, 3, and 2 groups. Consequently, all energy group structures from 40 to 2 energy groups are obtained through the above procedure. The concept of the successive collapsing method as described above is shown in **Figure 2.3**.

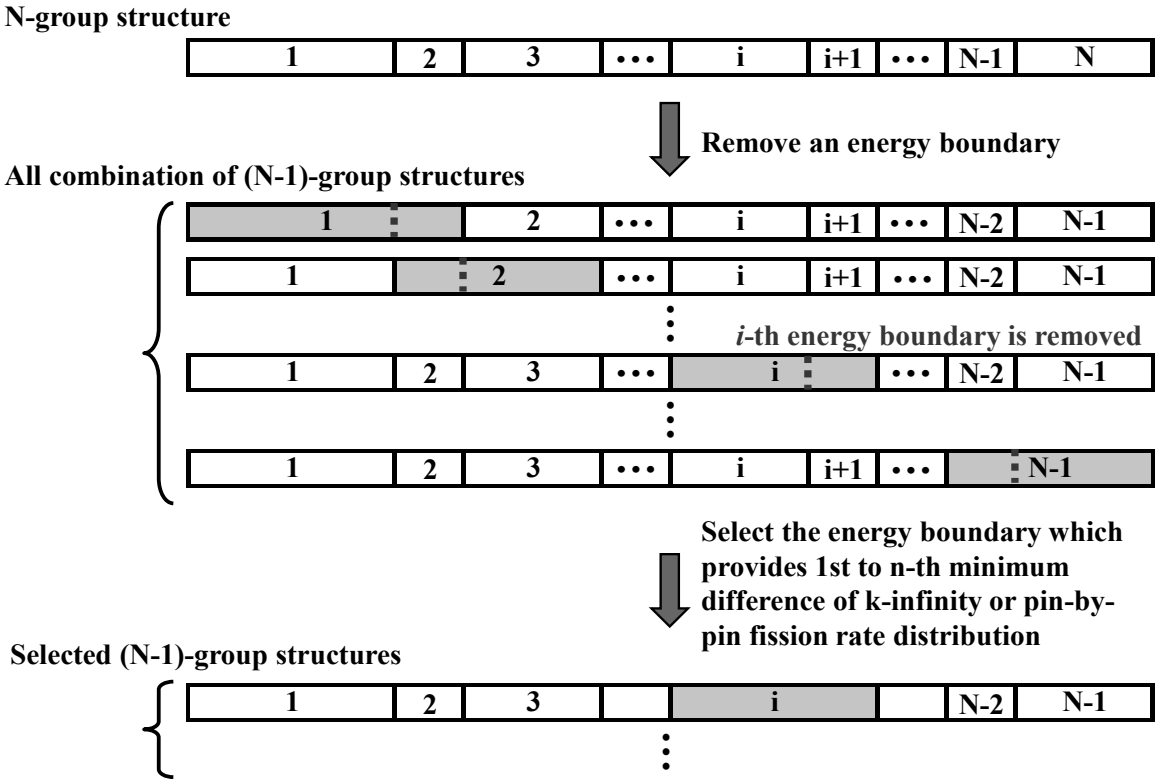

Figure 2.3 Concept of successive collapsing method

For example, let us assume that I have an N-group structure and I amoing to collapse it into an (N-1)-group structure. In this case, there are N-1 possible candidates of (N-1)-group structure since there are N-1 energy group boundaries in an N-group structure. In other words, I can generate an (N-1)-group structure by removing one of the N-1 energy boundaries. Once I have an (N-1)-group structure, the SPH method is utilized for the (N-1)-group cross sections to preserve the reaction rates in the 40-group calculation. The spectrum calculation, collapsing of cross sections from 40 to N-1 groups, and the application of the SPH method are carried out in the single assembly geometry. Then, (N-1)-group multi-assembly calculations are carried out N-1 times using the candidates of (N-1)-group structure and (N-1) group cross sections, which are obtained in the single assembly calculation. The differences of the

k-infinity and the pin-by-pin fission rate distribution between the (N-1)-group calculation and the 40-group calculation in the 2×2 multi-assembly are estimated for each (N-1)-group structure. Finally, the energy group boundary, which provides the minimum difference of the k-infinity or the pin-by-pin fission rate distribution in the above comparison, is removed to obtain an appropriate (N-1)-group structure. In the above procedure, either the difference of the k-infinity or that of the pin-by-pin fission rate distribution is used as the index to choose a removed energy boundary. The above procedure is repeated until the number of energy group reaches to the target value.

However, I may obtain a local minimum solution for energy group structure in the above optimization method since I only consider the minimum difference of the k-infinity or the pin-by-pin fission rate distribution, which is equivalent to the steepest descent search. It is well known that the steepest descent search may be trapped in local optimum for multi-modal problems. Therefore, in this Chapter, I consider not only the minimum difference of the k-infinity or the pin-by-pin fission rate distribution but also the n smallest differences (*i.e.*, the n best candidate energy group structures) in each successive collapsing step. For example, when the value of the candidate number n is 5, 5 candidate energy group structures are retained for the next collapsing step.

2.2.2.3. Successive expanding method

Next, I describe the detail of the successive expanding method. In the successive expanding method, I estimate all possible two group structures at first and establish the best two group structure from the 40 group structure. After that, the number of energy groups is increased one by one and the cross sections are expanded from coarse to fine energy groups (*i.e.*, the successive expanding method is a backward method of the successive collapsing method). The calculation procedure is almost identical with the successive collapsing method, except for the energy group boundary is added instead of removing it. The concept of the successive expanding method as described above is shown in **Figure 2.4**.

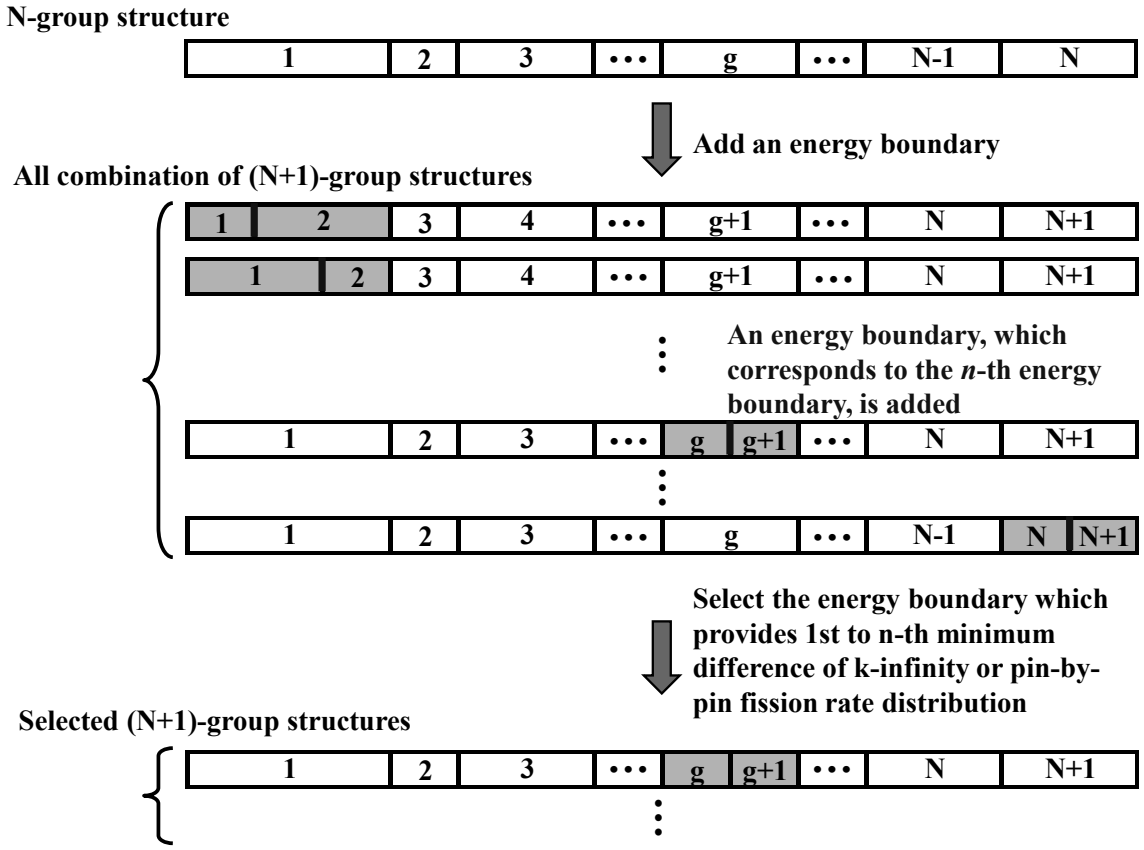

Figure 2.4 Concept of successive expanding method

Note that the added energy group boundary is taken from the original 40 group structure and is determined to provide the minimum difference of the k-infinity or the pin-by-pin fission rate distribution from the 40-group calculation in 2×2 multi-assembly. For example, let us consider to add an energy group boundary to an N-group structure. I have 40-N choices for adding energy boundary. Among these choices, an energy group boundary, which provides the minimum difference of the k-infinity or the pin-by-pin fission rate distribution between the (N+1)-group calculation and the 40-group calculation in 2×2 multi-assembly, is finally selected. Moreover, I also consider not only the minimum difference of the k-infinity or the pin-by-pin fission rate distribution but also the n smallest differences in each successive expanding step as in the successive collapsing method.

2.3. Preliminary sensitivity analysis

In this section, I independently investigate the various calculation conditions - the optimization index (the k-infinity or the pin-by-pin fission rate distribution), the successive procedure (collapsing or expanding), and the number of candidates during collapsing or expanding. At first, I compare the

calculation results obtained with the various calculation conditions. After that, I discuss on the calculation conditions to establish an appropriate energy group structure by applying the present approach.

2.3.1. Calculation conditions

In this section, I use the three types of the 2×2 multi-assembly geometries shown in **Figure 2.5**, which consist of the three types of typical BWR fuel assemblies shown in **Figure 2.6**, to take into account the spectral interference effect among fuel assemblies. The geometrical configurations of these BWR fuel assemblies are given by References [13] and [14], and the fuel rod enrichment distributions are manually decided.

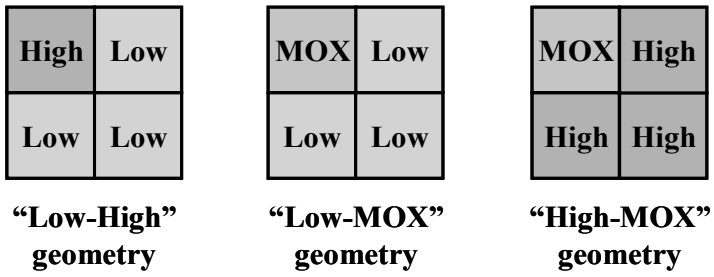

Figure 2.5 Geometries of three types of 2×2 multi-assembly

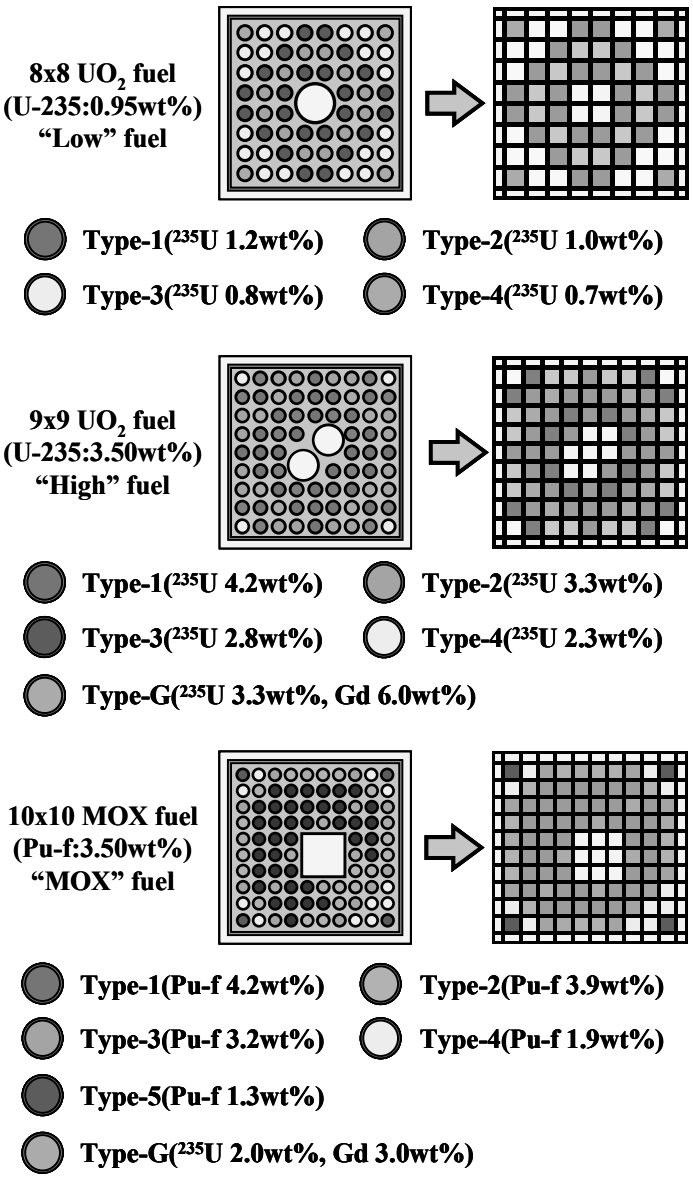

Figure 2.6 Geometries of three types of typical BWR fuel assemblies

The pin-cell averaged cross sections used in this Chapter are calculated in 40 energy groups, in which the up-scattering is considered up to 4eV. The 40 energy group structure is established by adding one energy group into the 39 energy group shown in the reference [15]. The 40 energy group structure well reproduces the results of the finer energy group calculations (*e.g.*, the 70 energy group calculation on the CASMO-4 code). In order to mitigate the error of the reaction rates due to the energy collapsing, the SPH method is utilized in a single assembly geometry [12]. I also utilize the SPH method to generate the 40-group pin-by-pin homogenized cross sections in order to reproduce the reference (fine) heterogeneous results. Therefore, the calculation results with the 40 energy groups are comparable to the reference results.

The assembly averaged void fraction is 40% since it is the averaged value of the axial void fraction in typical BWR cores. In this Chapter, I do not take into account the void fraction distribution within the channel box in the fuel assembly, thus I assume that the void distribution inside a fuel assembly is uniform. The exposure of the fuel assembly is 0GWd/t in order not to consider the reduction of the spectral interference effect by the burn-up feedback effect.

The single assembly and the 2×2 multi-assembly calculations are performed by the SUBARU code, which is a pin-by-pin core analysis code for BWR under development and utilizes the semi-analytic nodal method with the simplified P3 (SP3) theory [16].

In order to remove or to add energy group boundaries, the differences of the k-infinity and the pin-by-pin fission rate distribution in the 2×2 multi-assembly calculations are estimated since the k-infinity and the pin-by-pin fission rate distribution are important to evaluate important core parameters (*e.g.*, core reactivity and power peaking factor). Since I focus on the pin-by-pin core calculation method in which the depletion and the feedback calculations are carried out in each pin, the pin-by-pin fission rate distribution is considered to be rather important than the local peaking factor itself. The root-mean-square (RMS) difference of the pin-by-pin fission rate distribution and the difference of k-infinity are calculated by

$$\Delta R_{f,RMS} = \sqrt{\frac{\sum_{i \in fuel\,mesh} \left(R_{f,i}^{N-group} - R_{f,i}^{40-group} \right)^2}{N_{fuel\,mesh}}}, \tag{2.8}$$

$$\Delta k_{inf} = \frac{k_{inf}^{N-group} - k_{inf}^{40-group}}{k_{inf}^{40-group}}. \tag{2.9}$$

In Equations (2.8) and (2.9), $\Delta R_{f,RMS}$, $R_{f,i}$, $N_{fuelmesh}$, and Δk_{inf} are the RMS difference of the pin-by-pin fission rate distribution, the fission rate on the fuel mesh i, the total number of the fuel mesh, and the difference of the k-infinity, respectively. The superscripts *N-group* and *40-group* represent the results obtained by the N-group and the 40-group calculations, respectively.

2.3.2. Calculation results and remarks

2.3.2.1. Optimization indexes used to determine energy group structures

Firstly, I compare the results obtained by the two optimization indexes used in the present approach (*i.e.*, the differences of the k-infinity and the pin-by-pin fission rate distribution) and discuss the efficiencies of the two optimization indexes for the choice of the removed or added energy group boundary. For the above comparison, I carried out four types of calculations, which are the successive collapsing while minimizing the difference of the k-infinity or the pin-by-pin fission rate distribution and the successive expanding while minimizing the difference of the k-infinity or the pin-by-pin fission rate distribution, and these calculations are performed in the Low-High, the Low-MOX, and the High-MOX (2×2 multi-assembly) geometries shown in Figure 2.5.

Figure 2.7 shows the absolute difference of the k-infinity and the RMS difference of the pin-by-pin fission rate distribution from the reference (40-group) results for the four types of calculations in the Low-High geometry. Similarly, **Figures 2.8** and **2.9** show the absolute difference of the k-infinity and the RMS difference of the pin-by-pin fission rate distribution from the reference (40-group) results for the four types of calculations in the Low-MOX and the High-MOX geometries, respectively.

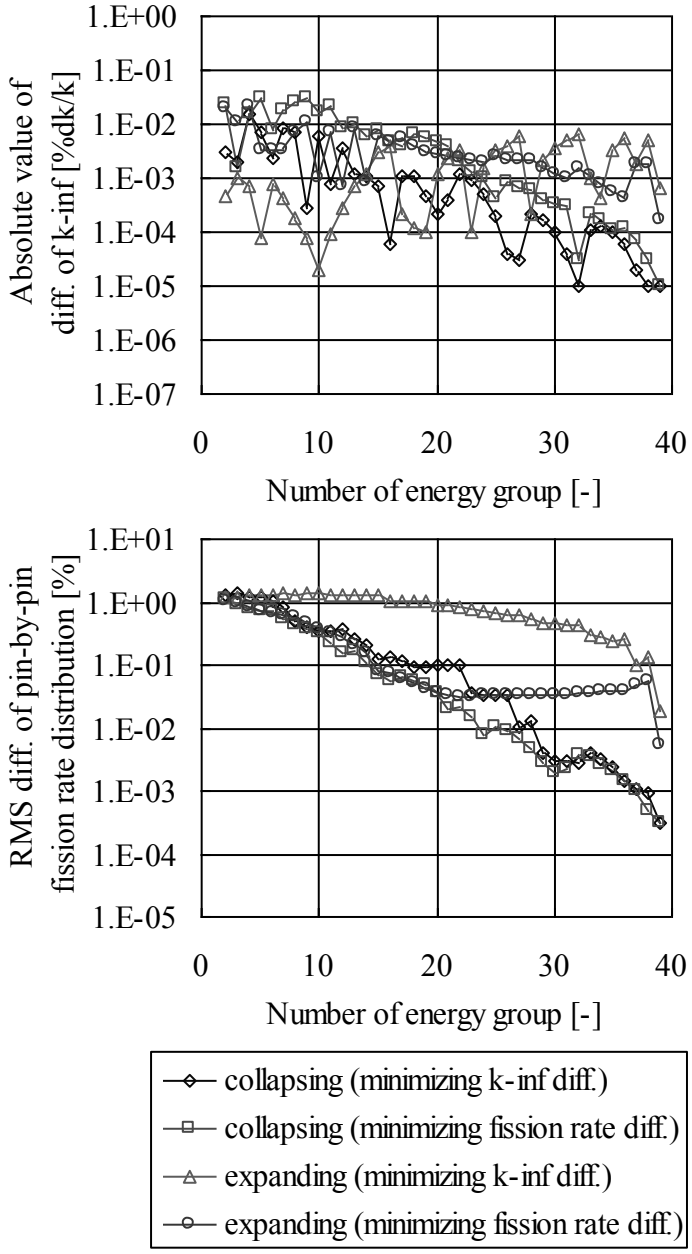

Figure 2.7 Differences of k-infinity and pin-by-pin fission rate distribution in Low-High geometry using the energy group structures obtained by various calculation methods

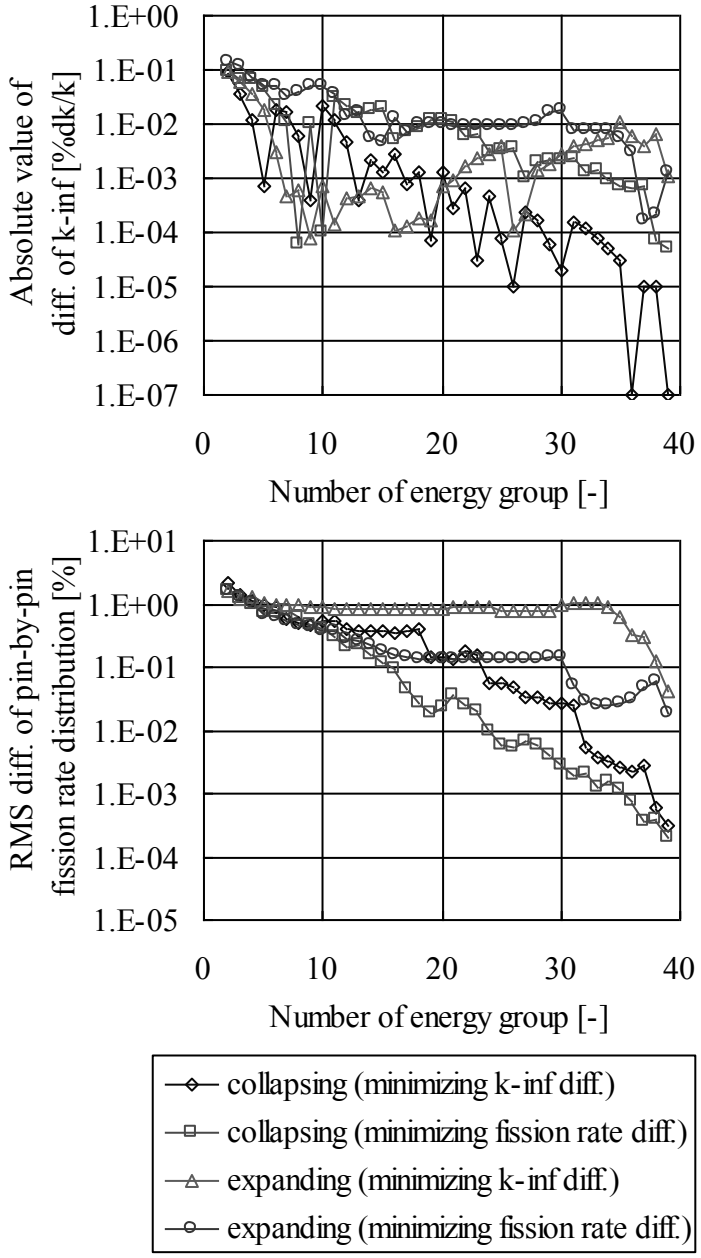

Figure 2.8 Difference of k-infinity and pin-by-pin fission rate distribution in Low-MOX geometry using the energy group structures obtained by various calculation methods

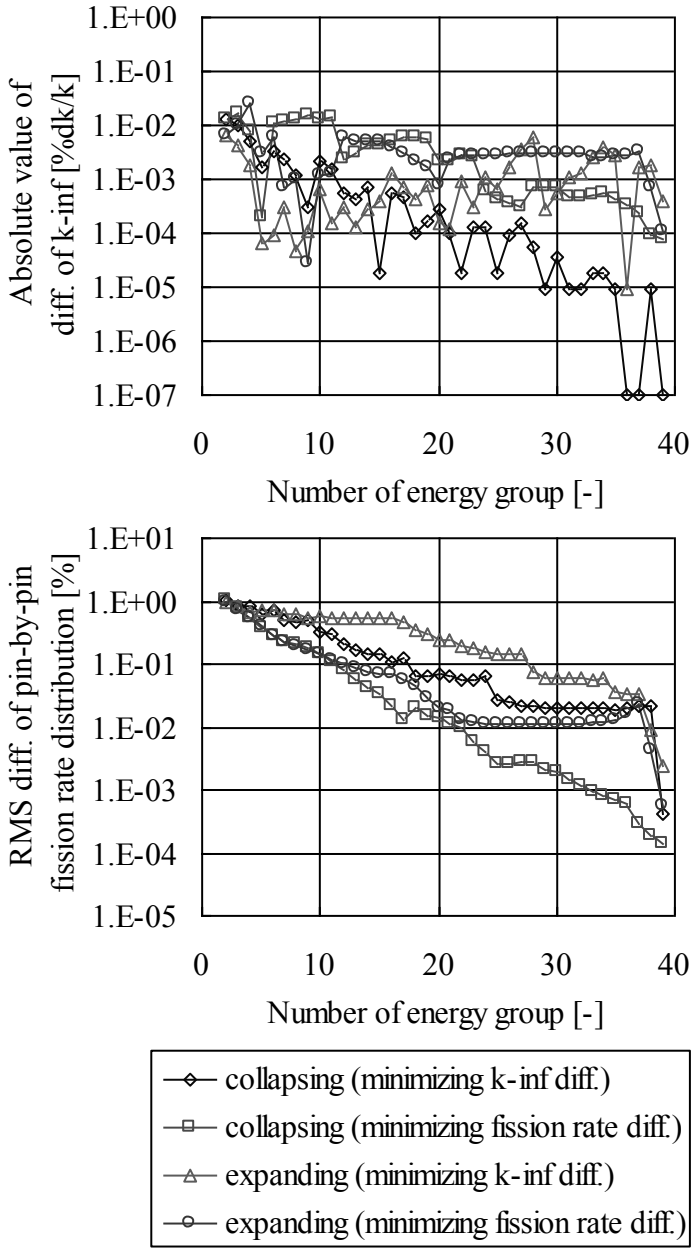

Figure 2.9 Difference of k-infinity and pin-by-pin fission rate distribution in High-MOX geometry using the energy group structures obtained by various calculation methods

From Figures 2.7 to 2.9, the differences of the k-infinity become smaller when they are minimized, which is reasonable. When the number of energy groups is larger than 10, the differences of the k-infinity are sufficiently smaller than about 0.01%dk/k regardless of the methods and the optimization indexes used in the procedure. The differences of the pin-by-pin fission rate distribution becomes smaller when they are minimized, which is, again, reasonable. The differences of the pin-by-pin fission rate distribution gradually become larger as the number of energy groups becomes smaller.

Let us consider about the efficiency of the optimization indexes. From Figures 2.7 to 2.9, the differences of the k-infinity do not show large dependence on the optimization indexes from the practical point of view (*e.g.*, they are smaller than 0.1%dk/k in any group calculations). On the other hand, the differences of the pin-by-pin fission rate significantly depend on the optimization indexes from the practical point of view (*e.g.*, there are about from 0.2 to 0.5% in 10-group calculations).

Therefore, the above results suggest that the present approach using the difference of the pin-by-pin fission rate distribution as the optimization index is useful to establish an appropriate energy group structure from the practical point of view.

The difference of the pin-by-pin fission rate distribution obtained by the successive expanding method is much larger than that obtained by the successive collapsing method when the number of energy groups is larger than 10. When the number of energy groups is smaller than 10, these methods provide similar results, which is practically same. Consequently, the successive collapsing method (minimizing the difference of the pin-by-pin fission rate distribution) shows better performance than the successive expanding method (minimizing the difference of the pin-by-pin fission rate distribution).

2.3.2.2. Comparison of energy group structure

Secondly, I compare the energy group structures obtained by the two approaches (*i.e.*, the successive collapsing and expanding methods shown in section 2). The variation of the energy group structures during successive collapsing is shown in **Figure 2.10**, in which only the minimum difference of the pin-by-pin fission rate distribution is considered as the optimization index in the Low-High geometry. **Figure 2.11** shows similar results obtained by the successive expanding method. **Figures 2.12** to **2.15** show the variations of the energy group structures with the successive collapsing and expanding methods in the Low-MOX and the High-MOX geometries, respectively. In Figures 2.10 to 2.15, the 2, 5,

10, 15, 20, 25, 30, 35, and 40 group structures are shown, and the arrows indicate that the corresponding energy group boundary is removed or added.

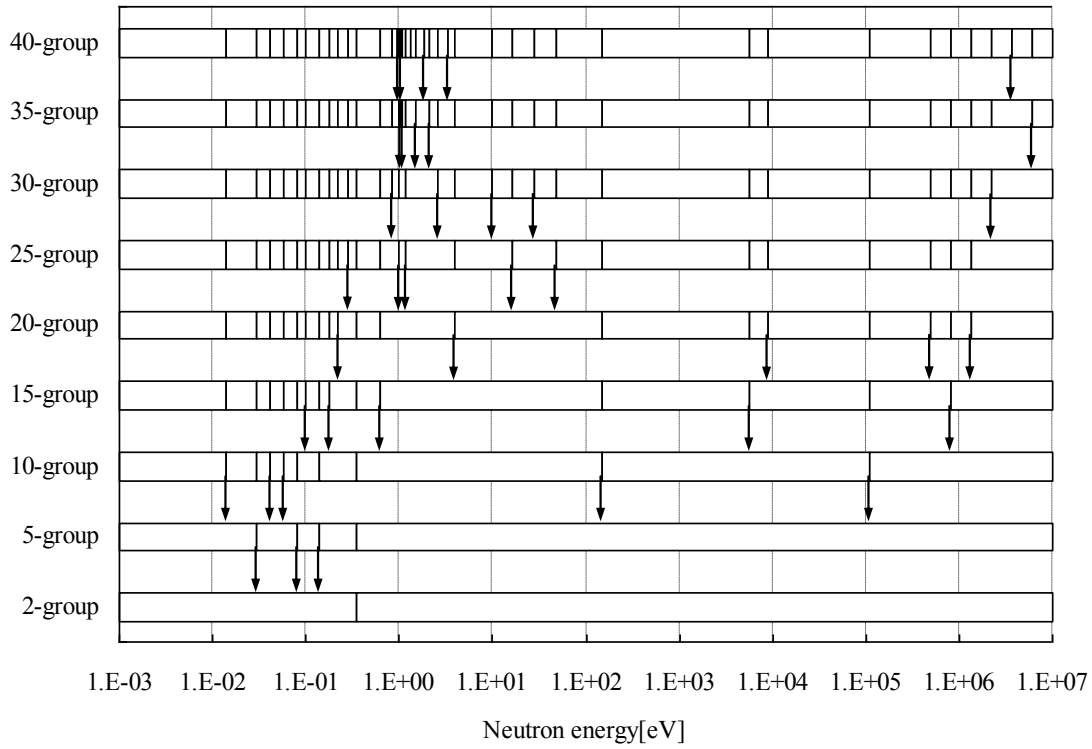

Figure 2.10 Energy group structure obtained by the successive collapsing method in Low-High geometry

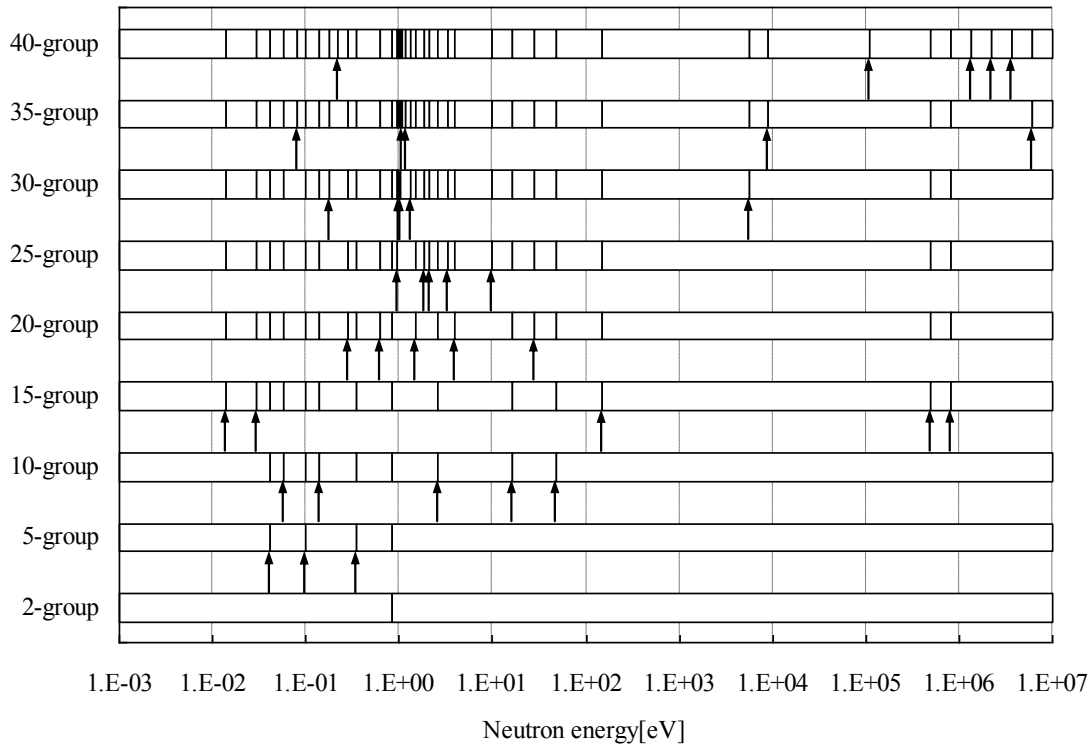

Figure 2.11 Energy group structure obtained by the successive expanding method in Low-High geometry

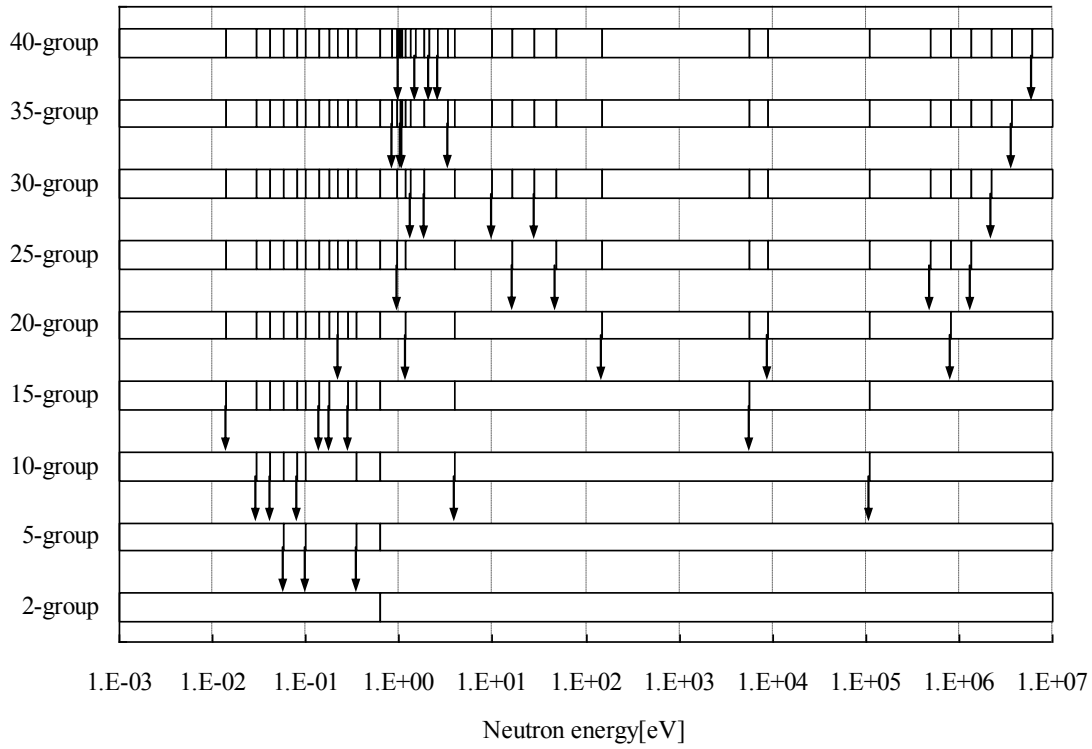

Figure 2.12 Energy group structure obtained by the successive collapsing method in Low-MOX geometry

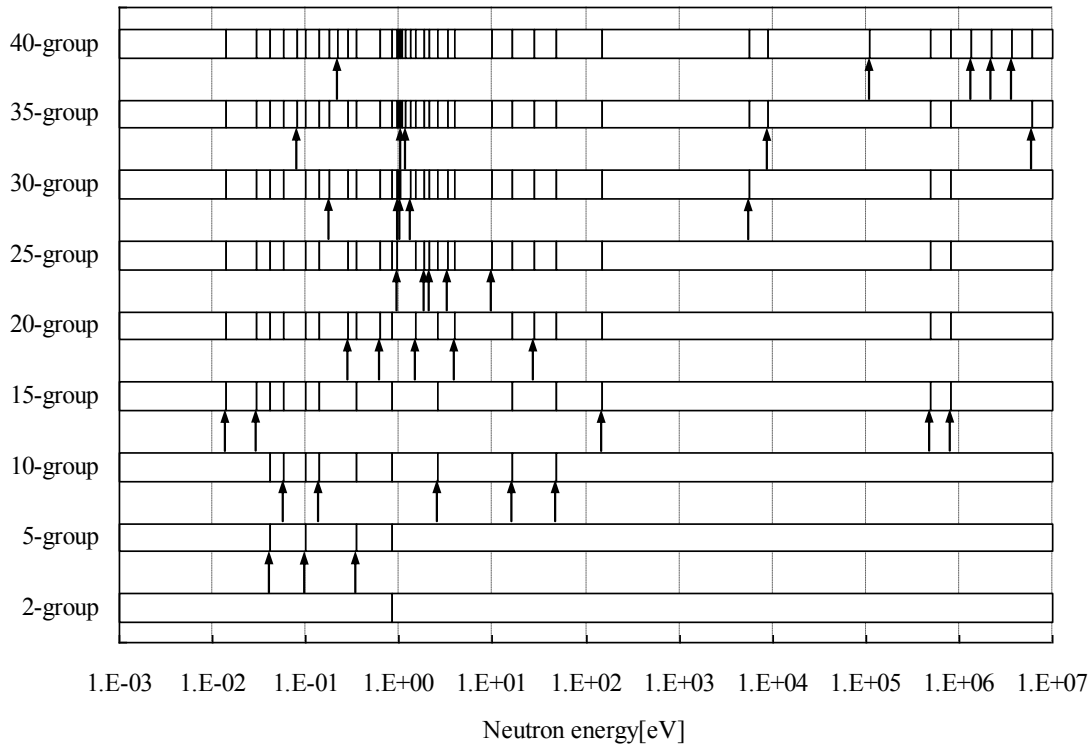

Figure 2.13 Energy group structure obtained by the successive expanding method in Low-MOX geometry

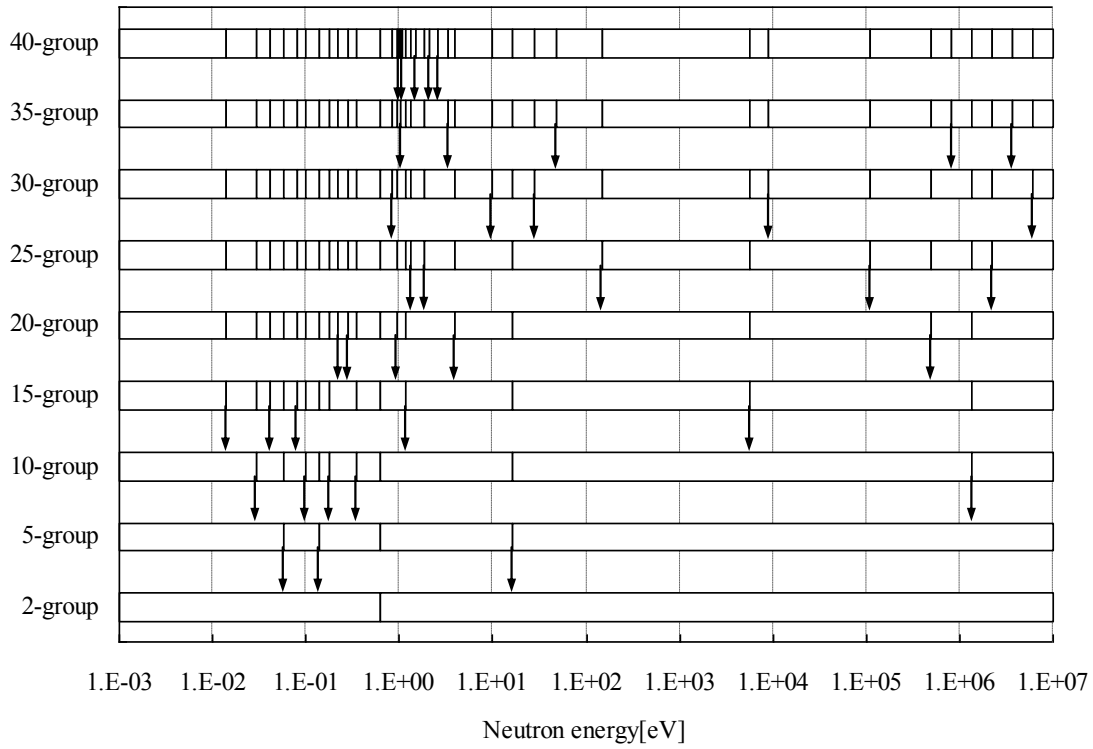

Figure 2.14 Energy group structure obtained by the successive collapsing method in High-MOX geometry

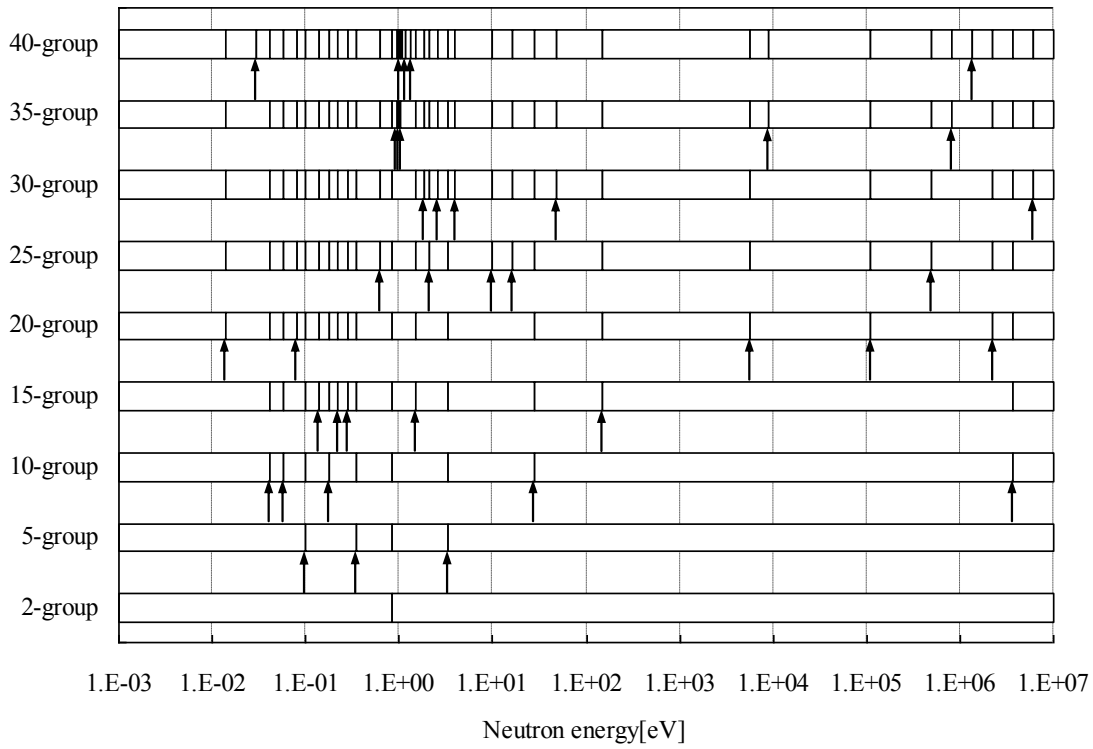

Figure 2.15 Energy group structure obtained by the successive expanding method in High-MOX geometry

From Figures 2.10, 2.12, and 2.14, the energy groups around 1eV, which have narrow energy widths to consider a resonance of Pu-240, are collapsed at the beginning stage of the process and those at the lower energy less than 1eV are collapsed in the latter stage of the process. From Figures 2.11, 2.13, and 2.15, the energy boundaries at the lower energy less than 1eV are expanded in the beginning stage of the process and those around 1eV are expanded in the latter stage of the process. Moreover, the 10, 15, 20, and 25 group structures in Figures 2.10 to 2.15 have similar energy group boundaries though their derivation processes are different.

The 2-group structures shown in Figures 2.11, 2.13, and 2.15 (*i.e.*, obtained by the successive expanding method) give the optimum 2-group structures for each geometries. The 2-group structures are also obtained by the successive collapsing method. With the successive collapsing method, the obtained 2-group results would not be the optimum results due to the limitation of the optimization method. However, the 2-group structures obtained by the successive collapsing method (Figures 2.10, 2.12, and 2.14) are similar to the optimum structures, which suggests the validity of the successive collapsing method. This observation is supported by the results that the 2-group calculation results shown in Figures 2.7 to 2.9 do not have significant differences.

2.3.2.3. Number of candidates considered in successive procedures

Finally, I compare the results obtained by the different number of candidates considered in the present approach. In the previous comparisons, the best energy group structure, which minimizes the difference of the k-infinity or the pin-by-pin fission rate distribution, is chosen during the calculation process. In other words, the steepest descent or the greedy strategy is adopted. In this comparison, I discuss effectiveness of the greedy strategy.

Instead of taking the best candidate in each choice, n best candidate structures, which give the n smallest differences of the k-infinity or the pin-by-pin fission rate distribution, are chosen in each calculation step. In this Chapter, the value of n is 1, 5, or 10. When the value of n is set to be 5, 25 candidate structures (5 candidates for the present calculation step, 5 candidates for the next calculation step) are evaluated. Calculation results are shown in **Figures 2.16** to **2.18**. Figure 2.16 indicates the results obtained by the successive collapsing and expanding methods in the Low-High geometry. Similarly, Figures 2.17 and 2.18 indicate the results obtained by the successive collapsing and expanding

methods in the Low-MOX and the High-MOX geometries, respectively. In both of the successive collapsing and expanding methods, the difference of the pin-by-pin fission rate distribution is used as the optimization index.

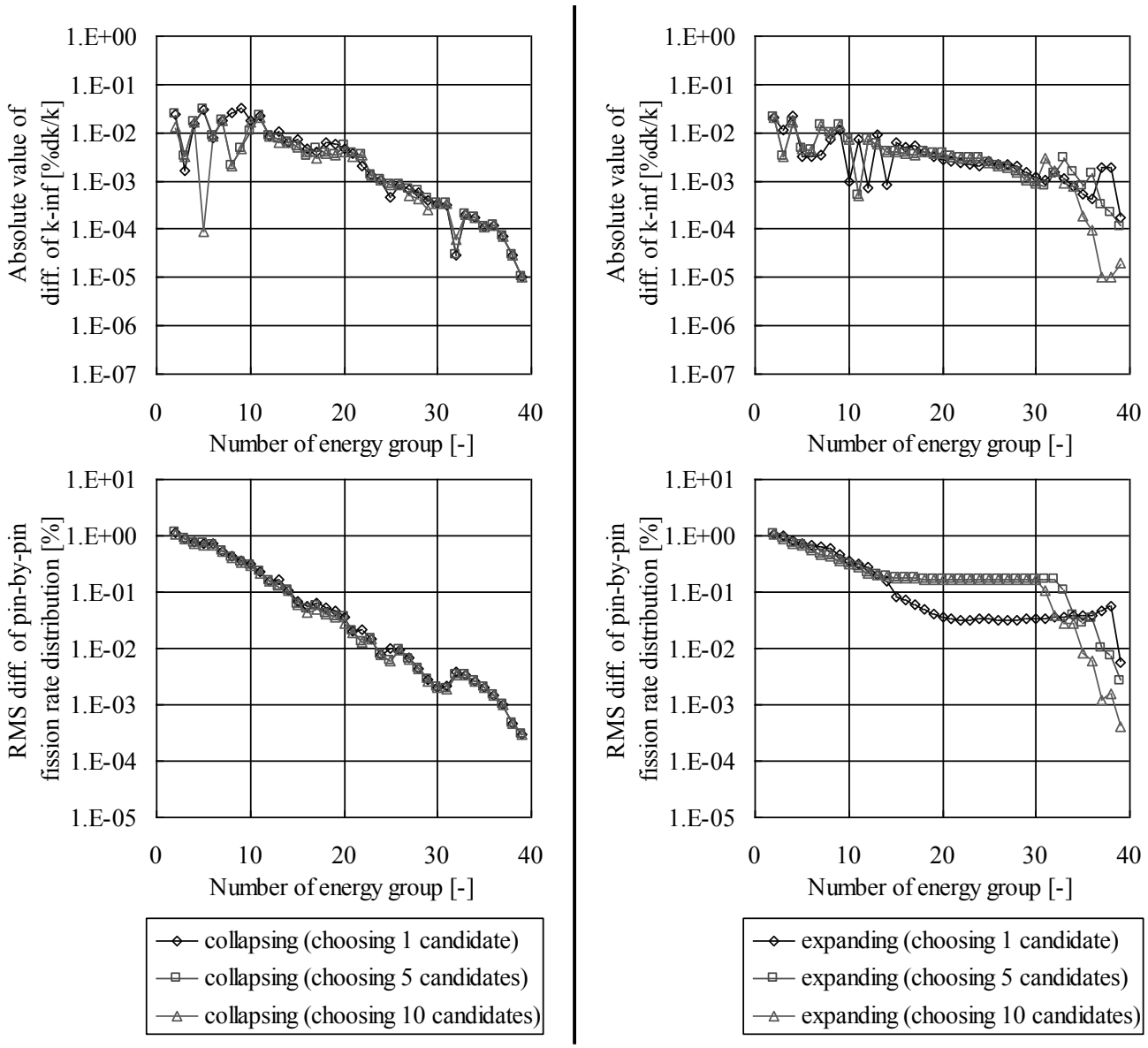

Figure 2.16 Difference of k-infinity and pin-by-pin fission rate distribution in Low-High geometry using the energy group structures obtained with various numbers of candidates

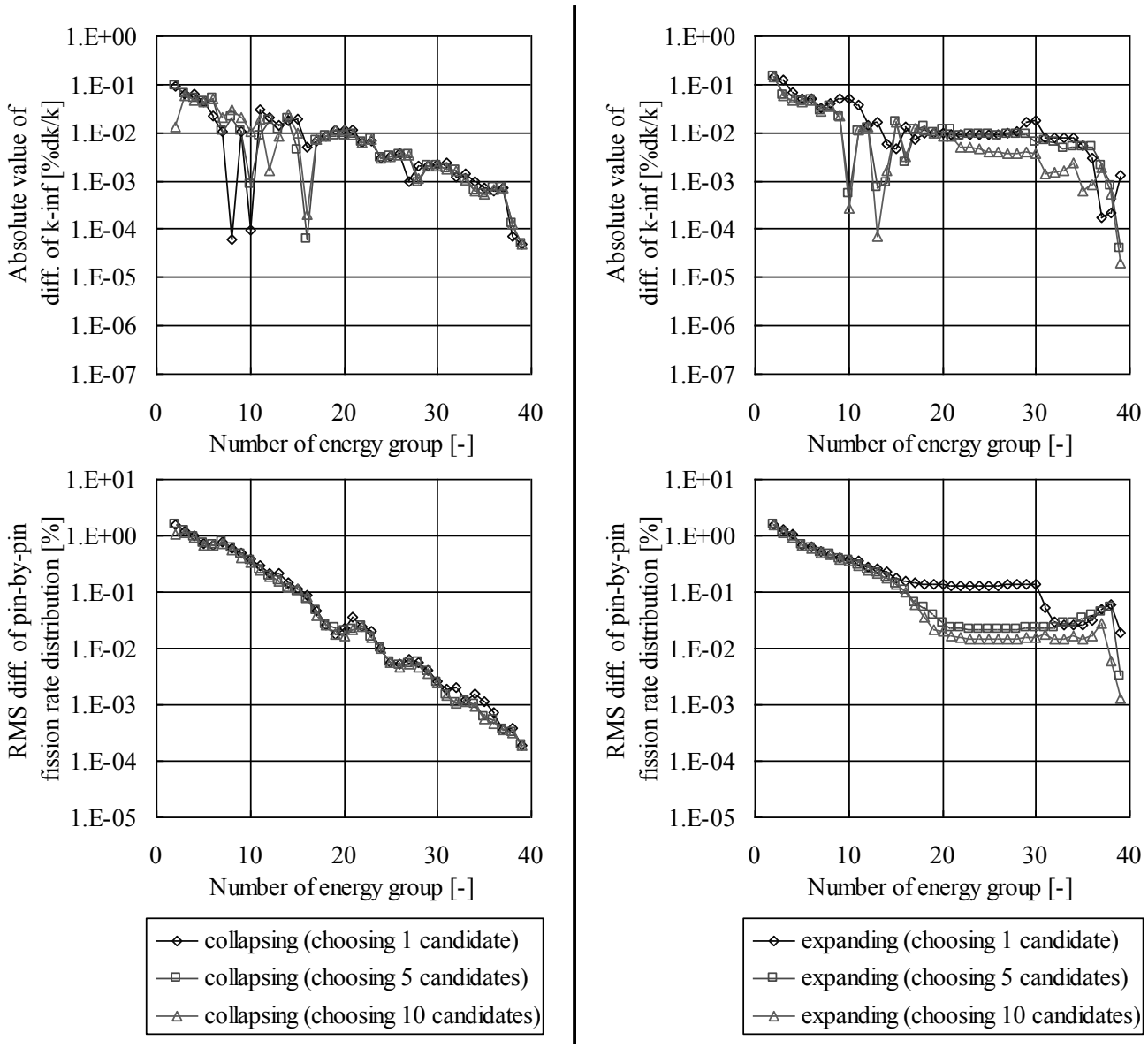

Figure 2.17 Difference of k-infinity and pin-by-pin fission rate distribution in Low-MOX geometry using the energy group structures obtained with various numbers of candidates

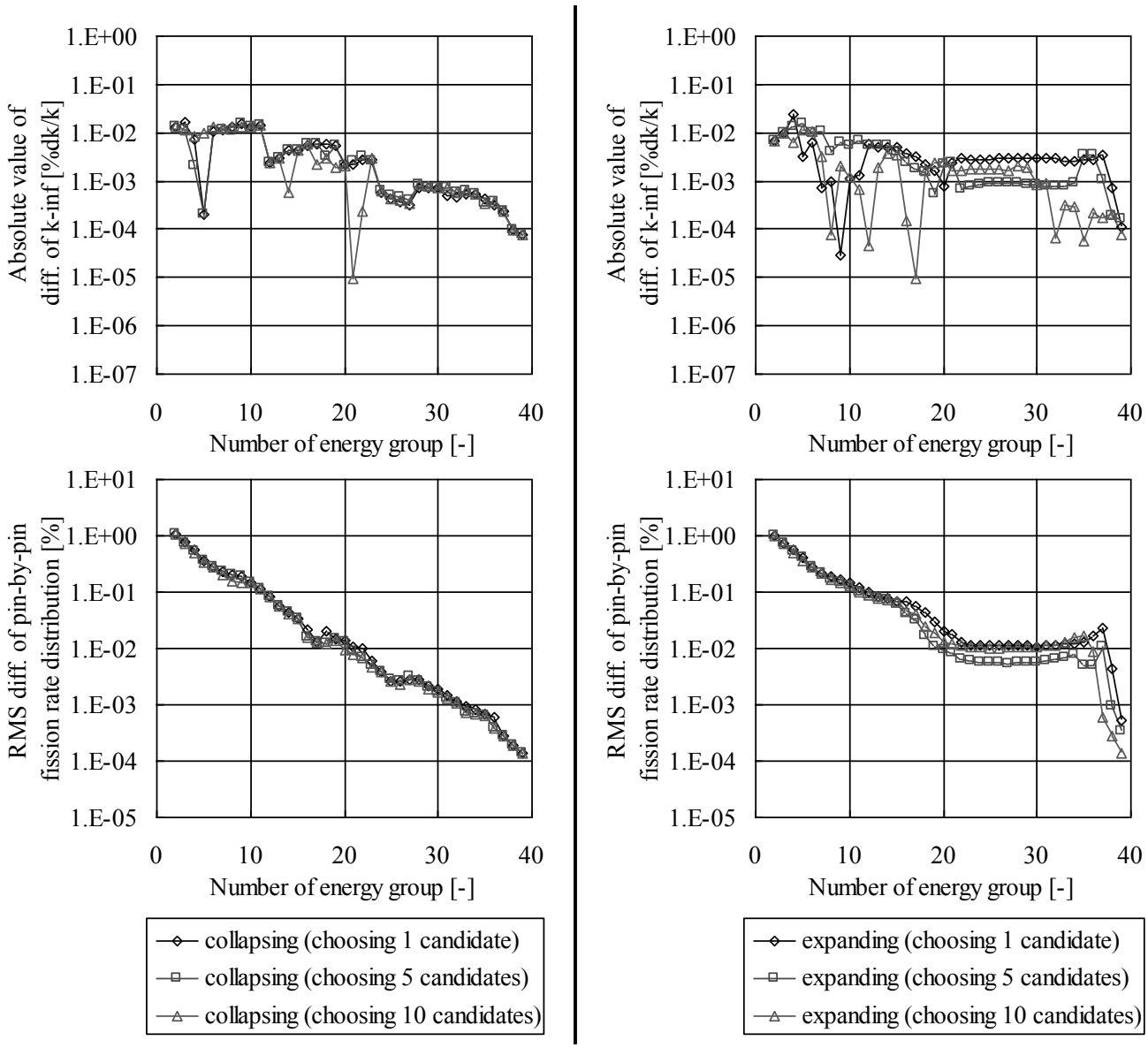

Figure 2.18 Difference of k-infinity and pin-by-pin fission rate distribution in High-MOX geometry using the energy group structures obtained with various numbers of candidates

Figures 2.16 to 2.18 show that the results are fairly insensitive to the number of candidates when the number of energy groups is approximately less than 15. Namely, the greedy strategy typically works well in the present optimization for energy group structures.

Therefore, the above results suggest that the greedy strategy, in which only the best candidate giving the minimum difference of the pin-by-pin fission rate distribution is chosen, is effective in both of the successive collapsing and expanding methods.

2.4. Evaluation of energy group structures

In the previous section, I compare the calculation results and the energy group structures obtained with the various calculation conditions - the optimization procedure (collapsing or expanding), the optimization index (the k-infinity or the pin-by-pin fission rate distribution), and the number of candidates during the optimization procedure. The results suggest that the successive collapsing method is efficient to construct an appropriate energy group structure. The greedy (steepest descent) strategy, which minimizes the difference of the pin-by-pin fission rate distribution, is efficient to establish an appropriate energy group structure.

Although a unified energy group structure is necessary for core calculations, the obtained energy group structures in the previous section depend on calculation configurations. Therefore, in this section, I simultaneously apply the present approach in various 2×2 multi-assembly geometries to determine a unified energy group structure, which is independent of calculation configurations. Then, I compare the results of the reference (40-group) and the coarse group calculations using the determined energy group structures to verify the usefulness of the present approach.

2.4.1. Construction of an appropriate energy group structure

2.4.1.1. Calculation conditions

I also use the three types of the 2×2 multi-assembly geometries shown in Figure 2.5, which consist of the three types of typical BWR fuel assemblies shown in Figure 2.6 [13, 14]. The pin-cell averaged cross sections and the 40 energy group structure, which is the reference (fine) energy group structure, are the same as those described in the section 2.3.1. The assembly averaged void fraction and the exposure of fuel assemblies are chosen from the combination of 0, 40, or 80% and 0, 10, 20, 30, 40,

50, or 60GWd/t. The assembly averaged void fraction and the exposure of fuel assemblies for the four fuel assemblies, which construct the 2×2 multi-assembly geometry, are the same. Namely, I use 63 calculation geometries (3 types of the 2×2 multi-assembly geometries, 3 different patterns for the assembly averaged void fraction, 7 different patterns for the exposure of fuel assemblies). The radial void distribution inside a fuel assembly is assumed to be uniform. The single assembly and the 2×2 multi-assembly calculations are performed by the SUBARU code [16]. In order to remove energy group boundaries, the RMS difference of the pin-by-pin fission rate distribution in the 2×2 multi-assembly geometry, which is evaluated by Equation (2.8), is used as the optimization index since the difference of the pin-by-pin fission rate distribution is more efficient than that of the k-infinity as discussed in the section 2.3.

2.4.1.2. Energy group structures and their calculation accuracies

In order to establish an appropriate unified energy group structure, I simultaneously consider the 63 types of the 2×2 multi-assembly geometries during the optimization of energy group structures to take into account the typical situations of the fuel loading in BWR cores. More specifically, I obtain the 63 RMS differences of the pin-by-pin fission rate distribution for each energy group boundary at first. Then, the maximum RMS difference of the pin-by-pin fission rate distribution among the 63 RMS differences is chosen as the optimization index. Finally, the energy group boundary, which minimizes the maximum RMS difference among the 63 RMS differences, is removed. The concept of above calculation procedure is shown in **Figure 2.19**.

Current optimization step:

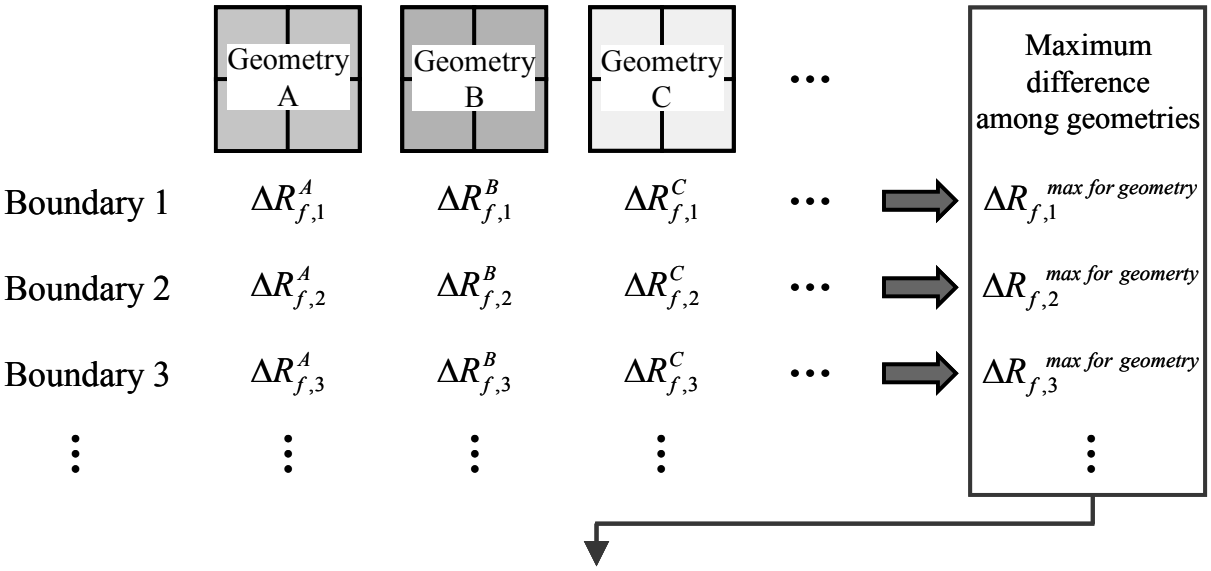

$\Delta R_{f,min\ for\ boundary}^{max\ for\ geometry}$ is considered to determine energy boundary to remove

$$\Delta R_{f,min\ for\ boundary}^{max\ for\ geometry} = \min\left(\Delta R_{f,1}^{max\ for\ geometry}, \Delta R_{f,2}^{max\ for\ geometry}, \Delta R_{f,3}^{max\ for\ geometry}, \cdots\right)$$

Move to next optimization step after removing energy boundary

Figure 2.19 Concept of simultaneous application of the present approach for various configurations

The variation of energy group structures during successive collapsing is shown in **Figure 2.20**, in which 2, 5, 10, 15, 20, 25, 30, 35, and 40 group structures are shown. **Figure 2.21** shows the absolute difference of the k-infinity and the RMS difference of the pin-by-pin fission rate distribution from the reference (40-group) results.

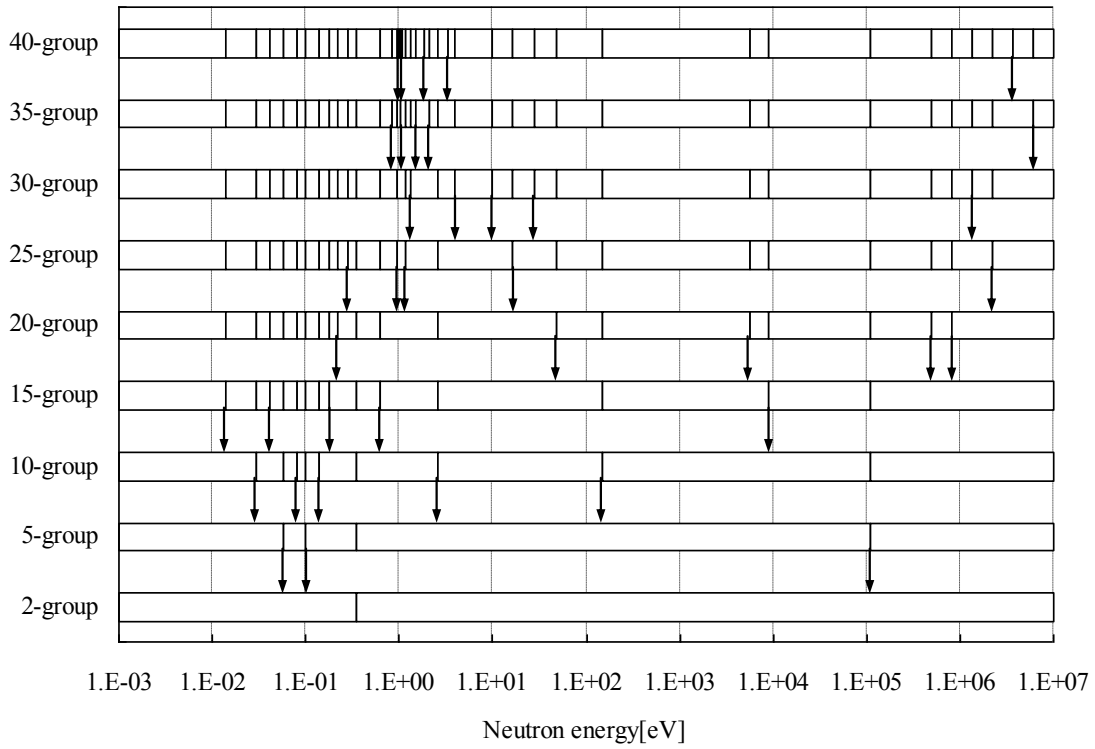

Figure 2.20 Energy group structures obtained by the successive collapsing method (simultaneously applied in 63 configurations)

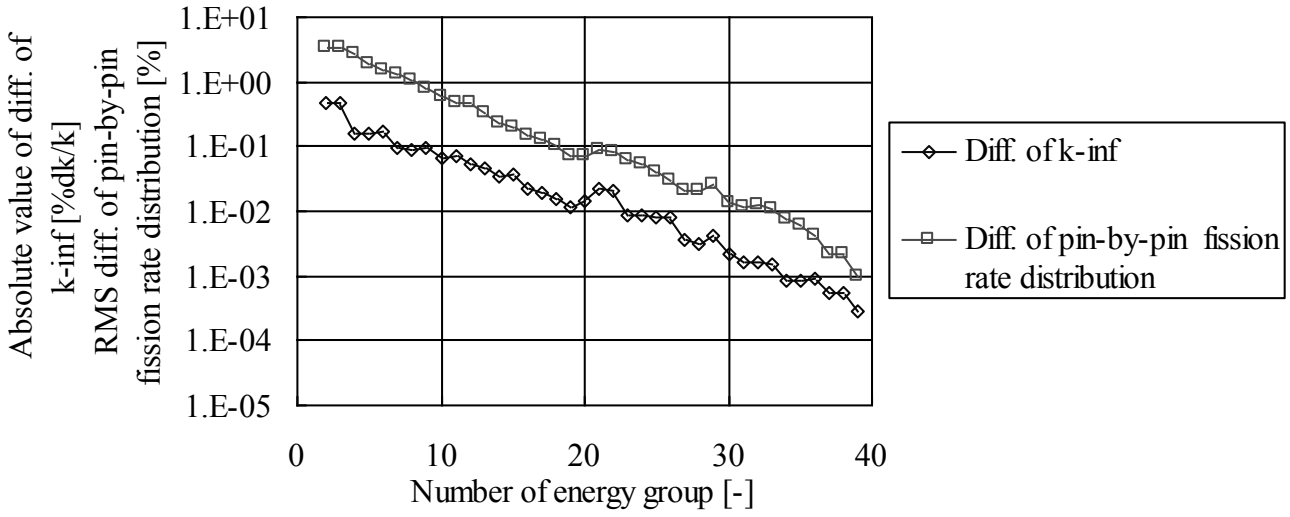

Figure 2.21 Difference of k-infinity and pin-by-pin fission rate distribution in multi-assemblies geometry using the energy group structures obtained by the successive collapsing method (simultaneously applied in 63 configurations)

From Figure 2.20, the energy groups around 1eV, which have narrow energy widths, are removed in the beginning stage of the process and those on the lower energy less than 1eV are removed in the latter stage of the process. These tendencies are similar to Figures 10, 12, and 14, in which the successive collapsing method is applied in the Low-High, the Low-MOX, and the High-MOX geometries. When the successive collapsing method is applied, the differences of the k-infinity and the pin-by-pin fission rate distribution typically decrease as the number of energy groups increases as shown in Figure 2.21.

The RMS difference of the pin-by-pin fission rate distribution and the absolute difference of k-infinity, which are obtained in the evaluation process of the successive collapsing method, are summarized in **Table 2-1**.

Table 2-1 Differences of k-infinity and pin-by-pin fission rate distribution for various energy group structures obtained in the process of the successive collapsing method

		2-group	5-group	8-group	15-group
Absolute value of difference of k-infinity [%dk/k]	Average value	0.07	0.02	0.02	0.01
	Maximum value	0.47	0.16	0.09	0.04
RMS difference of pin-by-pin fission rate distribution [%]	Average value	1.29	0.68	0.35	0.10
	Maximum value	3.41	1.88	1.02	0.20

In Table 2-1, the maximum and average values of the differences of the pin-by-pin fission rate distribution and the k-infinity among the 63 differences are shown. In the verification of the energy group structures shown in the next section, I carry out various 2×2 multi-assembly calculations and calculation accuracies are statistically estimated. Therefore, the values shown in Table 2-1 are considered as the baseline and are used as the quantitative indexes to evaluate the adequacy of the energy group structures.

2.4.2. Verification in colorset assembly geometries

In the previous section, the energy group structures for the various numbers of energy groups are established by the successive collapsing method, in which the 2×2 multi-assembly geometries with the various fuel types, the assembly averaged void fraction, and the exposure of fuel assemblies are simultaneously taken into account.

In this section, I verify the validity of the energy group structures that are obtained by the successive collapsing method. Extensive 2×2 multi-assembly calculations with various conditions are carried out with the established energy group structures and the calculation results are compared with those of the reference (40-group) calculations.

2.4.2.1. Calculation conditions

I carry out various 2×2 multi-assembly calculations, which consist of the three types of typical BWR fuel assemblies shown in Figure 2.6 [13, 14]. The fuel assemblies in the 2×2 multi-assembly geometry are selected to consider all possible combinations of the four fuel assemblies, in which the Low-High, the Low-MOX, and the High-MOX geometries shown in Figure 2.5 are also included. The pin-cell averaged cross sections and the 40 energy group structure, which is the reference (fine) energy group structure, are the same as those described in the section 2.3.1. The numbers of the coarse energy group structures are 2, 5, 8, and 15 and their energy group structures are shown in **Table 2-2**. These energy group boundaries in Table 2-2 are obtained in the previous section.

Table 2-2 Energy group structures determined by the successive collapsing method

	2-group structure		5-group structure		8-group structure		15-group structure	
Group	Upper[eV]	Lower[eV]	Upper[eV]	Lower[eV]	Upper[eV]	Lower[eV]	Upper[eV]	Lower[eV]
1	1.00E+07	3.50E-01	1.00E+07	1.11E+05	1.00E+07	1.11E+05	1.00E+07	1.11E+05
2	3.50E-01	1.00E-05	1.11E+05	3.50E-01	1.11E+05	1.48E+02	1.11E+05	9.12E+03
3			3.50E-01	1.00E-01	1.48E+02	3.50E-01	9.12E+03	1.48E+02
4			1.00E-01	5.80E-02	3.50E-01	1.40E-01	1.48E+02	2.60E+00
5			5.80E-02	1.00E-05	1.40E-01	1.00E-01	2.60E+00	6.25E-01
6					1.00E-01	5.80E-02	6.25E-01	3.50E-01
7					5.80E-02	3.00E-02	3.50E-01	1.80E-01
8					3.00E-02	1.00E-05	1.80E-01	1.40E-01
9							1.40E-01	1.00E-01
10							1.00E-01	8.00E-02
11							8.00E-02	5.80E-02
12							5.80E-02	4.20E-02
13							4.20E-02	3.00E-02
14							3.00E-02	1.50E-02
15							1.50E-02	1.00E-05

The assembly averaged void fraction is chosen from 0, 40, or 80%. The radial void distribution inside a fuel assembly is assumed to be uniform. In order to assume typical BWR core conditions in the beginning of cycle, the exposure of fuel assemblies is chosen from 0, 15, or 30GWd/t. The void fractions and the exposure of the four fuel assemblies constructing the 2×2 multi-assembly geometry may be different. Namely, I also consider all possible combinations of the void fraction and the exposure in the 2×2 multi-assembly geometries.

The single assembly and the 2×2 multi-assembly calculations are performed by the SUBARU code [16]. In order to verify the calculation accuracy of the coarse energy group structure, I compare the differences of the pin-by-pin fission rate distribution and the k-infinity between the reference (fine) group and the coarse group calculations. The differences of the pin-by-pin fission rate and the k-infinity are calculated by Equations (2.8) and (2.9), respectively. The calculation results with 40-group calculation are considered as the reference results.

2.4.2.2. Calculation results and remarks

Figure 2.22 summarizes the differences obtained by the 2×2 multi-assembly calculations considering all possible combinations of types of fuel assemblies, the void fraction, and the average exposure. In Figure 2.22, the thick solid and dotted lines indicate the maximum and the average values of the differences obtained in the process of the successive collapsing method, which are shown in Table 2-1, respectively. The average and the maximum values of the differences in Figure 2.22 are summarized in **Table 2-3**.

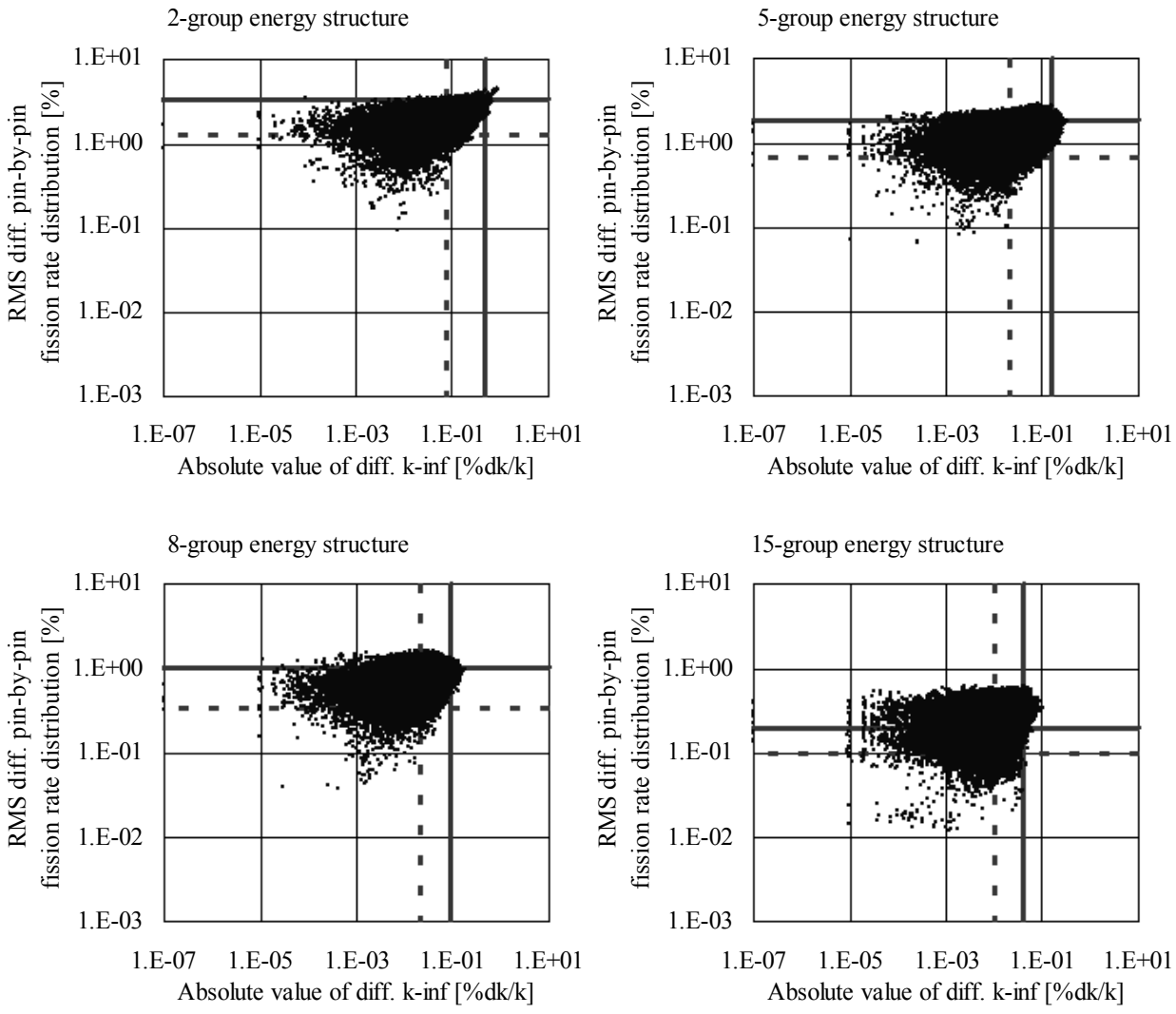

Figure 2.22 Differences of k-infinity and pin-by-pin fission rate obtained with the determined 2, 5, 8, and 15-group energy structure

Table 2-3 Average values and maximum values of differences of k-infinity and pin-by-pin fission rate distribution in the verification calculation

		2-group	5-group	8-group	15-group
Absolute value of difference of k-infinity [%dk/k]	Average value	0.09	0.04	0.02	0.02
	Maximum value	0.88	0.32	0.18	0.09
RMS difference of pin-by-pin fission rate distribution [%]	Average value	1.83	1.15	0.66	0.27
	Maximum value	4.65	2.87	1.61	0.63

From Figure 2.22, the RMS differences of the pin-by-pin fission rate distribution and the absolute differences of the k-infinity are generally smaller than the solid lines, which indicate the maximum differences shown in Table 2-1. The 2×2 multi-assembly geometries shown in Figure 2.5 is used in the evaluation of Table 2-1, which is performed in the section 2.4.1.2. The 2×2 multi-assembly geometries shown in Figure 2.5 have the significant spectral interference effect. On the other hand, since all possible combinations of fuel assemblies are considered in the present verification calculation, similar fuel assemblies would be loaded in the 2×2 multi-assembly geometries in this verification calculation. Therefore, the spectral interference effect is generally smaller than the previous calculation shown in Table 2-1. Consequently, the differences of pin-by-pin fission rate and the k-infinity appeared in Figure 2.22 are generally smaller than the maximum differences shown in Table 2-1.

In order to evaluate the adequacy of the determined energy group structures, I compare the calculation results obtained by the 8-group structure determined in this Chapter and the 8-group structure used in the previous study [5, 6]. The 8-group structure used in the previous study is manually optimized. Note that the 8-group structure in the previous study is slightly modified in order to be consistent with the energy boundaries used in this Chapter. Both of the 8-group structures are shown in **Table 2-4**. The average and the maximum values of the differences, which are obtained by the 2×2 multi-assembly calculations considering all possible combinations of types of fuel assemblies, the void fraction, and the average exposure, are described in **Table 2-5**.

Table 2-4 8-group structures determined in Chapter 2 and that used in the previous study

	Determined in the present study		Used in the previous study	
Group	Upper[eV]	Lower[eV]	Upper[eV]	Lower[eV]
1	1.00E+07	1.11E+05	1.00E+07	8.21E+05
2	1.11E+05	1.48E+02	8.21E+05	5.53E+03
3	1.48E+02	3.50E-01	5.53E+03	4.00E+00
4	3.50E-01	1.40E-01	4.00E+00	1.02E+00
5	1.40E-01	1.00E-01	1.02E+00	6.25E-01
6	1.00E-01	5.80E-02	6.25E-01	1.40E-01
7	5.80E-02	3.00E-02	1.40E-01	5.80E-02
8	3.00E-02	1.00E-05	5.80E-02	1.00E-05

Table 2-5 Average values and maximum values of differences of k-infinity and pin-by-pin fission rate distribution in the 8-group calculations

		Determined in the present study	Used in the previous study
Absolute value of difference of k-infinity [%dk/k]	Average value	0.02	0.04
	Maximum value	0.18	0.17
RMS difference of pin-by-pin fission rate distribution [%]	Average value	0.66	0.75
	Maximum value	1.61	1.97

From Table 2-5, most results obtained by the determined 8-group structure in this Chapter are better than those obtained by the 8-group structure used in the previous study. For the maximum value of the difference of the k-infinity, the result obtained by the determined 8-group structure is slightly worse than that obtained by the 8-group structure used in the previous study. However, the difference between them is about 0.04%dk/k and is very small from the practical point of view. Therefore, I conclude that the present approach (*i.e.*, the successive collapsing method) is very efficient to establish an appropriate energy group structure for BWR pin-by-pin core analysis.

2.5. Conclusions

In this Chapter, an optimization approach to establish an appropriate energy group structure for BWR pin-by-pin fine mesh core analysis is proposed and its performance is confirmed through the verification calculations with the use of various 2×2 multi-assembly geometries.

Firstly, I investigate two different methods to establish an appropriate energy group structure (*i.e.*, the successive collapsing and expanding methods). In the successive collapsing method, the number of energy groups is decreased one by one and cross sections are collapsed into coarser energy groups in this process. In the successive expanding method, the number of energy groups is increased one by one and cross sections are expanded into finer energy groups in this process. In these methods, energy group boundaries, which provide the n smallest differences of the k-infinity or the pin-by-pin fission rate distribution between the coarse group calculation and the reference (40-group) calculation in the 2×2 multi-assembly, are removed or added.

Secondly, the sensitivity analyses of the present approach are carried out focusing on the following points:

- Approach to establish energy group structure (collapsing or expanding),
- Optimization index (difference of k-infinity or pin-by-pin fission rate distribution),
- Number of candidates considered in the successive collapsing/expanding procedure.

From the sensitivity analyses, the following points are confirmed:

(1) The successive collapsing method can determine the optimum or quasi-optimum energy group structures since the 2-group energy group structures and the 2-group calculation results obtained by the successive collapsing and expanding methods do not have significant differences even though the successive expanding method gives the optimum solution in the case of the 2-group problem.

(2) The successive collapsing method is superior to the successive expanding method to determine an appropriate energy group structure.

(3) The difference of the k-infinity from the reference (fine) group result gradually decreases as the number of energy groups becomes larger.

(4) The difference of the pin-by-pin fission rate distribution from the reference (fine) group result gradually decreases as the number of energy groups becomes larger and is more

sensitive than that of the k-infinity.

(5) The greedy (steepest decent) strategy, in which the best candidate providing the minimum difference of the k-infinity or the pin-by-pin fission rate distribution is chosen, works well in both of the successive collapsing and expanding methods.

(6) The above tendencies are observed in all three types of the 2×2 multi-assembly geometries considered in this Chapter (*i.e.*, the Low-High, the Low-MOX, and the High-MOX geometries shown in Figure 2.5).

From the above results of the sensitivity analyses, I decide the calculation conditions of the present approach as shown in follows:

- Successive collapsing method (optimization procedure),
- Pin-by-pin fission rate distribution (optimization index),
- Considering only the best candidate of the energy group structure, (*i.e.*, the greedy or steepest decent strategy) (the number of candidates considered in the successive procedure).

Finally, in order to verify the applicability of the present approach, I simultaneously apply the present approach in the various 2×2 multi-assembly geometries to establish unified coarse energy group structures that are suitable for BWR pin-by-pin core analysis. Then the performance of the established coarse energy group structures is confirmed through the statistical analyses on the differences of the k-infinity and the pin-by-pin fission rate distribution in the various configurations, which simulate typical BWR core conditions in the beginning of cycle. The comparison of statistical analysis results with the coarse energy group structure, which is used in the previous study and is manually optimized, is also carried out.

The following points are confirmed through the verification calculations:

(1) The successive collapsing method can determine the appropriate energy group structures for the various numbers of energy groups when I simultaneously apply it in the various 2×2 multi-assembly geometries.

(2) Accuracy of the 8-group structure determined in this Chapter is better than that obtained by the 8-group structure used in the previous study.

The present approach would be applicable to establish an appropriate multi-group energy structure from finer energy group (*e.g.*, more than 100 groups), although the computational time and the

required memory become larger as the number of energy groups becomes larger. For example, if the number of reference (fine) energy groups is 100, approximately 20~30 times longer computational time will be necessary, compared to the calculation conditions described in this Chapter.

Moreover, the present approach can generate energy group structures of arbitrary number of energy groups. Therefore, the relationship between the number of energy groups and the calculation accuracy is obtained and the number of energy groups and the energy group structure suitable for the pin-by-pin core analysis can be decided considering significant energetic and spatial distribution of neutron spectrum in BWR fuel assemblies due to complicated geometries.

References

[1] K. R. Rempe, K. S. Smith, "SIMULATE-3 Pin Power Reconstruction: Methodology and Benchmarking," *Nucl. Sci. Eng.*, **10**, pp. 334-342, (1989).

[2] T. Iwamoto, M. Yamamoto, "Pin Power Reconstruction Methods of the Few-Group BWR Core Simulator NEREUS," *J. Nucl. Sci. Technol.*, **36**[12], pp. 1141-1152, (1999).

[3] T. Bahadir, S-Ö Lindahl, S. Palmtag, "SIMULATE-4 Multigroup Nodal Code with Microscopic Depletion Model," *Proc. Mathematics and Computation, Supercomputing, Reactor Physics and Nuclear and Biological Applications (M&C 2005)*, Sep. 12-15, 2005, Avignon, France, (2005). [CD-ROM].

[4] K. Yamaji, H. Matsumoto, M. Nakano, "Development of the New Pin-by-pin Core Calculation Method with Embedded Heterogeneous Assembly Calculation," *Proc. Int. Conf. on Physics of Reactors (PHYSOR 2006)*, Sep. 10-14, 2006, Vancouver, Canada, (2006). [CD-ROM].

[5] K. Tada, A. Yamamoto, Y. Yamane *et al.*, "Applicability of the Diffusion and Simplified P3 Theories for Pin-by-Pin Geometry of BWR," *J. Nucl. Sci. Technol.*, **45**[10], pp. 997-1008, (2008).

[6] K. Tada, A. Yamamoto, Y. Yamane, "Treatment of Staggered Mesh for BWR Pin-by-Pin Core Analysis," *J. Nucl. Sci. Technol.*, **46**[2], pp. 163-174, (2009).

[7] M. Tatsumi, A. Yamamoto, "Advanced PWR Core Calculation Based on Multi-group Nodal-transport Method in Three-dimensional Pin-by-Pin Geometry," *J. Nucl. Sci. Technol.*, **40**[6], pp. 376-387, (2003).

[8] F. Hoareau, M. Fiscounakis, D. Couyras *et al.*, "A Pin by Pin Microscopic Depletion Sheme Using an Homogeneous Core Calculation with Pin-Power Reconstruction," *Proc. 2009 Int. Congress on the Advances in Nuclear Power Plants (ICAPP '09)*, May 10-14, 2009, Tokyo, Japan, (2009). [CD-ROM].

[9] C. Yi, G. Sjoden, J. Mattingly *et al.*, "Computationally Optimized Multi-group Cross Section Data Collapsing using the YGROUP Code," *Proc. Int. Conf. on the Physics of Reactors (PHYSOR 2010)*, May 9-14, 2010, Pittsburgh, Pennsylvania, (2010). [CD-ROM].

[10] M. L. Williams, "Generalized Contribution Response Theory," *Nucl. Sci. Eng.*, **108**, pp. 355-383, (1991).

[11] P. Mosca, C. Mounier, R. Sanchez *et al.*, "An Adaptive Energy Mesh Constructor for Multigroup

Library Generation for Transport Codes," *Nucl. Sci. Eng.*, **167**, pp. 40-60, (2011).

[12] A. Hébert, "A Consistent Technique for the Pin-by-Pin Homogenization of A Pressurized Water Reactor Assembly," *Nucl. Sci. Eng.*, **113**, pp. 227-238, (1991).

[13] H. Okuno, Y. Naito, K. Suyama, *OECD/NEA Burnup Credit Criticality Benchmarks Phase IIIB: Burnup Calculations of BWR Fuel Assemblies for Storage and Transport*, JAERI-Research 2002-001, Japan Atomic Energy Research Institute (JAERI), (2002).

[14] A. Yamamoto, T. Ikehara, T. Ito *et al.*, "Benchmark Problem Suite for Reactor Physics Study of LWR Next Generation Fuels," *J. Nucl. Sci. Technol.*, **39**[8], pp. 900-912, (2002).

[15] F. Tani, F. Jatuff, R. Chawla, "Study of Spectral Heterogeneities for the Interpretation of Calculational Trends in Predicting Pin Power Distributions in a SVEA-96+ BWR Assembly," *Ann. Nucl. Energy*, **33**, pp. 490-498, (2006).

[16] K. Tada, A. Yamamoto, S. Kosaka *et al.*, "Development of a Prototype Pin-by-pin Fine Mesh Calculation Code for BWR Core Analysis," *Proc. Int. Conf. on Physics of Reactors (PHYSOR '08)*, Sep. 14-19, 2008, Interlaken, Switzerland, (2008). [CD-ROM].

Chapter 2 is based on an Accepted Manuscript of an article published by Taylor & Francis in Journal of Nuclear Science and Technology on June 22th, 2012, available online: http://wwww.tandfonline.com/10.1080/00223131.2012.693890.

Chapter 3. A macroscopic depletion model to tabulate pin-cell averaged cross sections

3.1. Introduction

A cross section set, which is provided for a BWR core simulator, depends on many core state and depletion history variables (*e.g.*, exposure, void fraction, fuel temperature, control rod insertion, and related histories of them). In order to exactly reproduce appropriate cross sections for a core simulator, all possible combinations of the core state and depletion history variables would be tracked in the cross section preparation through lattice physics calculations. However, such calculation procedure would be impractical due to the limitation on computation time since the number of possible combinations of core state variables becomes huge. Thus, in current core analysis, assembly-averaged cross sections are calculated for the limited combinations of the core state and the depletion history variables and they are tabulated for the subsequent use by core calculations. In the core calculations, therefore, the cross sections are reconstructed for a node with the particular combination of the core state and the depletion history variables from the tabulated cross section set.

In the current BWR core analysis using the advanced nodal method, calculations are carried out through two subsequent steps. Firstly, heterogeneous structure of fuel assemblies is homogenized through lattice physics calculations and then core calculations are carried out using the assembly-averaged cross sections. Since fuel assemblies are treated in a homogeneous manner in core calculations, the pin-power reconstruction method, which synthesizes the global smooth power distribution in a homogeneous node and the heterogeneous pin-power distribution obtained by the lattice physics calculations, is used to estimate the detail pin-power distribution [1, 2]. However, the accurate estimation of the detail pin-power distribution in a highly heterogeneous core (*e.g.*, a mixed-oxide fuel loaded, a heavily poisoned, or a large enrichment splitting core) might be difficult. Therefore, various efforts (*e.g.*, sub-meshing of fuel assembly, on-the-fly boundary condition adjustment through iteration of lattice physics calculations) have been developed for this issue [3-5].

Recently, as a candidate of the next generation core analysis method, the pin-by-pin fine mesh core calculation method, in which the cross sections are homogenized in each pin-cell, has been studied [6-9]. It is possible to directly estimate the detailed pin-power distribution in the pin-by-pin fine mesh

core calculation method. Since the spatial homogenization is carried out only for pin-cell, it is expected that the error associated with the spatial homogenization of cross sections will be reduced. Therefore, crucial core parameters (e.g., power peaking factor) would be more accurately calculated with the pin-by-pin core analysis method.

In the pin-by-pin fine mesh core calculation method, the cross section set used for core analysis is a crucial point from the viewpoints of the calculation accuracy, the required memory, and the computation time. The pin-by-pin fine mesh core calculation method naturally requires larger size of the cross section set since the cross sections for each pin-cell should be independently tabulated in the cross section set. Therefore, an efficient cross section model (*i.e.*, a cross section tabulation method) is very important for a practical pin-by-pin core simulator. Pin-by-pin core analysis codes have been developed for PWR and thus there are practical cross section models for them [8]. However, BWR fuel assemblies are much more complicated than those of PWR since they have large water rods, a large enrichment splitting, large water gaps between fuel assemblies, and a control rod insertion. In this context, I should newly develop a cross section model for the BWR pin-by-pin fine mesh core calculation method, which has not been investigated so far.

This Chapter focuses on the fundamental development of the cross section model on BWR normal operations, which is based on a macroscopic depletion model, used in the BWR pin-by-pin core calculation method. Section 3.2 is devoted for the description of the cross section model used in this Chapter. Verifications of the present cross section model are shown in section 3.3 through numerical benchmark calculations. Finally, concluding remarks are given in section 3.4.

3.2. Methodology

3.2.1. Overview

In the pin-by-pin core calculation method, pin-cell averaged cross sections are calculated for many combinations of the core state and depletion history variables, which have influences on the cross sections, and are tabulated prior to the core calculations. The appropriate cross sections for the target core state are interpolated, synthesized, and reconstructed during the core calculations. In the conventional method, the cross sections are homogenized for a fuel assembly as shown in **Figure 3.1**. On the other hand, in the pin-by-pin fine mesh core calculation method, the cross sections are homogenized

for each pin-cell as shown in **Figure 3.2**.

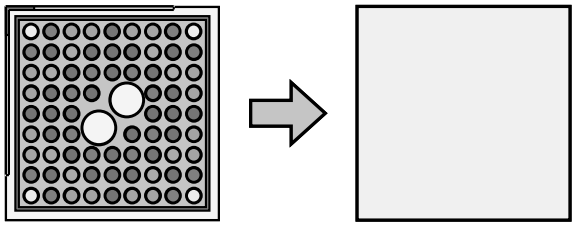

Figure 3.1 Homogenization of cross sections in the conventional advanced nodal method

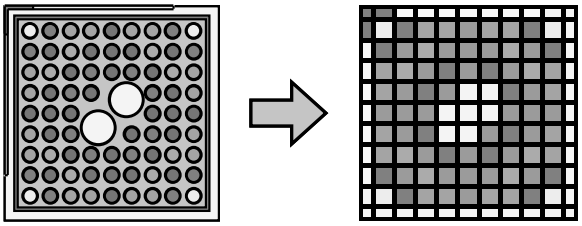

Figure 3.2 Homogenization of cross sections in the pin-by-pin fine mesh core calculation method

The cross sections for each pin-cell are different due to the variations of exposure and neutron flux in each position within fuel assemblies even if fuel rod types are the same. When the variations among fuel rods are not very large, the cross sections for a particular fuel rod type may be tabulated in a unified set and it can be applied to all fuel rods of the same type in a fuel assembly. However, in BWR fuel assemblies, heterogeneity is much larger than that of PWR due to the existence of the channel box, the water rods, the large enrichment splitting, and the control rod insertion. Therefore, in this Chapter, the cross sections for each pin-cell are independently tabulated, even if there are several identical types of fuel rods in fuel assemblies.

There are two major approaches on the cross section model (*i.e.*, the macroscopic depletion and the microscopic depletion models) [3, 10, 11]. In the macroscopic depletion model, since the macroscopic cross sections needed as one of the input datum to carry out the core calculations are mainly tabulated, the computational load can be saved. On the other hand, in the microscopic cross section model, the differences of nuclide compositions in each fuel pin can be directly estimated through the depletion of nuclides. However, the larger size of the computational memory is necessary since the microscopic cross sections and the number densities of major nuclides (*e.g.*, ^{235}U, ^{238}U, ^{239}Pu, ^{155}Gd, and ^{157}Gd) should be tabulated and maintained in the computational memory. Therefore, in this Chapter, I focus on the macroscopic depletion model since the pin-by-pin fine mesh core calculation method

naturally requires larger size of the cross section set (*e.g.*, for an 8×8 fuel assembly, the number of homogenized meshes in the pin-by-pin fine mesh core calculation method is about fifty times larger than that in the conventional core calculation method) and the application of the microscopic cross section model for the pin-by-pin fine mesh core calculation method might be difficult from the viewpoints of the required memory especially for routine (or production) design calculations.

The macroscopic cross sections in BWR cores have the dependence on many core state and depletion history variables (*e.g.*, exposure, void fraction, fuel temperature, moderator temperature, control rod insertion, and related history of them) as:

$$\Sigma = \Sigma\left(EXP, VOI, TFU, TMO, CR, HVOI, HTFU, HTMO, HCR\right), \tag{3.1}$$

where, Σ, *EXP*, *VOI*, *TFU*, *TMO*, *CR*, *HVOI*, *HTFU*, *HTMO*, *HCR* are the macroscopic cross section, the exposure, the void fraction, the fuel temperature, the moderator temperature, the control rod insertion, the void history, the fuel temperature history, the moderator temperature history, and the control rod history, respectively. These core state and depletion history variables are continuously changing during the reactor operation thus the macroscopic cross sections are also varied.

Note that the following relationships between the void fraction and the moderator temperature were assumed in this Chapter:

(1) The void fraction in the subcooled boiling condition is not considered, thus the void fraction is constant at 0% when the moderator temperature is below the saturation temperature (559K) at the reactor pressure on BWR normal operation (about 70MPa).

(2) When the void fraction is higher than 0%, the moderator temperature is constant at 559K.

The variations of cross sections in core calculations are classified into two different types of phenomena (*i.e.*, the instantaneous and the history effects). The instantaneous effect is caused by the instantaneous changes of the core state variables. For example, the variations of cross sections are caused when the void fraction changes. In this effect, the fuel composition is fixed. Therefore, the instantaneous effect is captured by the branch calculations in lattice physics calculations, in which the fuel composition is fixed and particular core state variables (*e.g.*, the void fraction and the fuel temperature) are changed. The history effect is caused by the variation of the fuel composition due to the

changes in the core state variables during the burnup. For example, when fuel rods are depleted under a high void fraction condition, the harder neutron spectrum promotes the production of plutonium generation thus the reduction of the k-infinity during the burnup becomes smaller. In BWR core calculations, it is very important to accurately capture the history effect due to the large variation of the void fraction and the control rod insertion. Therefore, the history effect is captured by a series of history depletion calculations, in which particular core state variables are changed from the base calculation case (*e.g.*, the void fraction in the base calculation case is 40% while that in the history depletion calculation is 80%).

As shown in Equation (3.1), the macroscopic cross sections have the dependence on many core state and depletion history variables. However, it is difficult to directly tabulate the macroscopic cross sections in this form since it would require the calculations on all possible combinations of the core state and depletion history variables. Thus, several approximations are necessary to efficiently tabulate the macroscopic cross sections.

In this Chapter, I tabulate the macroscopic cross sections in the following manner:

(1) The macroscopic cross sections are independently tabulated for different exposure points since the exposure has dominant effect on the macroscopic cross sections through the variations of number densities of fuel materials. The detail for this is described in the next section.

(2) The macroscopic cross sections for each pin-cell are independently tabulated, even if there are identical types of fuel rods in fuel assemblies, since the heterogeneity of BWR fuel assemblies is much larger than that of PWR due to the existence of the channel box, the water rods, the large enrichment splitting, and the control rod insertion.

(3) The macroscopic cross sections are approximated by a linear combination of the macroscopic cross sections on a specific condition (*i.e.*, a base state condition) and the variations of macroscopic cross sections for the instantaneous and the history effects.

(4) The cross term effect among the instantaneous and the history effects is not considered since the variations of microscopic cross sections and number densities of moderator and structure materials are mainly caused by the instantaneous effect while the variations of those of fuel materials are mainly caused by the history effects.

The validity of them is discussed in the section 3.3.

By the above tabulation manner, the macroscopic cross sections shown in Equation (3.1) are approximated as:

$$\begin{aligned}&\Sigma(EXP,VOI,TFU,TMO,CR,HVOI,HTFU,HTMO,HCR)\\&\approx \Sigma_{base}(EXP,VOI_{base},TFU_{base},TMO_{base},CR_{base})\\&\quad+\Delta\Sigma_{inst}(EXP,VOI,TFU,TMO,CR)\\&\quad+\Delta\Sigma_{hist}(EXP,HVOI,HTFU,HTMO,HCR)\end{aligned}, \tag{3.2}$$

where, the subscripts *base*, *inst*, and *hist* represent the base condition, the instantaneous and the history effects, respectively. The first, second, third terms in the right hand side denote the macroscopic cross section on the base condition, the variation of macroscopic cross section for the instantaneous effect, and that for the history effect, respectively. Note that each term in the right hand side incorporates the dependence on the exposure and is separately tabulated for the exposure since the exposure has dominant effect on the macroscopic cross sections through the variations of number densities of nuclides.

Essentially, the above approximation for macroscopic cross sections can be applied to reproduce the macroscopic cross sections on every core conditions. If the variations of macroscopic cross sections become larger (*i.e.*, the range of application is expanded), the error due to the interpolation of macroscopic cross sections becomes larger, thus, an appropriate choice of macroscopic cross sections used as tabulation points is important to reduce the interpolation error.

In this study, as discussed later, tabulation and verification conditions are chosen to cover BWR operation conditions (*e.g.*, void fractions and control rod insertion). Thus, it is expected that the approximation for macroscopic cross sections in Equation (3.2) can be applied on BWR operation conditions. In order to confirm such applicability, verifications by core tracking calculations are necessary, however, core tracking calculations are not carried out in this study since core tracking datum are unavailable.

In this Chapter, the following condition is considered as the base state condition, which corresponds to BWR normal operations:

- Void fraction is 40%, which is the typical core average value.
- Fuel temperature is 800K, which is the typical core average value.

- Moderator temperature is 559K, which is the saturation temperature at the reactor pressure (about 70MPa).
- Control rod is withdrawn since majority of control rods are withdrawn during full power operations.

The second term is the correction term for the instantaneous effect and is calculated by the polynomial interpolations of the macroscopic cross sections for the core state variables. Note that this term has complicated dependences for the core state variables (*i.e.*, the cross term effects among several core state variables are caused). For example, when the void fraction changes from 40% to 50%, the variations of the macroscopic cross sections due to the change of the void fraction would also depend on the fuel temperature or the control rod insertion. The detail treatments of the cross term effect are discussed in the section 3.2.3.

The third term is the correction term for the history effect and is calculated by the polynomial interpolations of the macroscopic cross sections for the depletion history variables. Note that the cross term effects among several depletion history variables are occurred in this term similar to the correction term for the instantaneous effect. The detail treatments are discussed in the section 3.2.4.

3.2.2. Pin-wise exposure

The exposure has dominant effect on the macroscopic cross sections through the variations of number densities of nuclides. For example, the macroscopic absorption cross sections in Gd-bearing fuel pin-cell are rapidly changing until most of Gd is depleted. Thus, in the present macroscopic cross section model, the instantaneous and the history effects and the xenon feedback are considered for each exposure points used in the lattice physics calculations.

The pin-wise exposures depend on the depletion histories. Namely, the pin-wise exposures calculated in core calculations are different from those in the lattice physics calculations to generate the pin-wise cross sections. Moreover, the pin-wise exposures, which are obtained by various depletion calculations in a case matrix calculation in a lattice physics code, would be significantly different from each other. Therefore, the pin-wise cross sections obtained by lattice physics calculations should be tabulated on standard exposure points.

The macroscopic cross sections are interpolated for standard exposure points by utilizing the

cubic spline interpolation (CSI), which is one of piece-wise polynomial approximations [12]. Since the CSI requires some boundary conditions on limits of interpolation, second order differential coefficients of macroscopic cross sections with respect to exposure are assumed to be zero, which is called the natural boundary condition, in the present macroscopic cross section model.

The verifications of the interpolation of macroscopic cross sections for the exposure, which utilizes the CSI, are described in the section 3.3.2.1.

3.2.3. Instantaneous effect

The core state variables that have the influences on the macroscopic cross sections are continuously changing during the operations of reactor cores. The instantaneous effect, which is caused by the instantaneous changes of the core state variables, is incorporated by the variations of macroscopic cross sections. The variations of macroscopic cross sections due to the variation of fuel composition are not considered in the instantaneous effect.

The correction term for the instantaneous effect is described as the second term in the right hand side of Equation (3.2). This term is estimated by the branch calculations from several depletion points of the depletion calculation on the base condition. The concept of the branch calculation is shown in **Figure 3.3**. In the branch calculations, a (or a few) core state variable(s) is (or are) changed while fixing the fuel composition, which depends on the exposure.

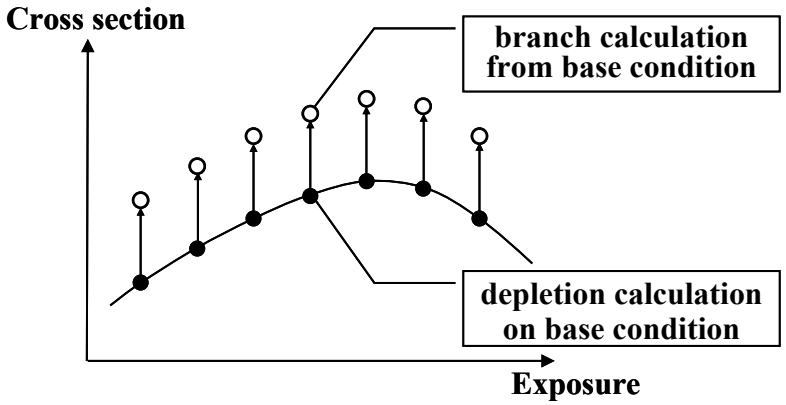

Figure 3.3 Concept of branch calculation

The macroscopic cross sections after the instantaneous variations of core state variables are estimated in lattice physics calculations. When one of the core state variables instantaneously changes

from the base condition, the variations of macroscopic cross sections (i.e., the delta cross sections) are estimated by:

$$\Delta\Sigma_{inst}\left(EXP, X_{base} \rightarrow X'\right) = \Sigma_{branch}\left(EXP, X'\right) - \Sigma_{base}\left(EXP, X_{base}\right), \tag{3.3}$$

where, X is one of the core state variables and the subscript *branch* represents the branch calculation from the base depletion calculation. Note that, in this Chapter, I independently tabulate the macroscopic cross sections for each pin-cell mesh. Therefore, *EXP* is the pin-wise exposure if the pin-cell mesh includes a fuel rod; otherwise *EXP* is the assembly-averaged exposure. In Equation (3.3), the left hand side denotes the delta cross section due to the instantaneous change of the core state variable X from the base condition X_{base} to the perturbed condition X'. The first term in the right hand side denotes the macroscopic cross section calculated by the branch calculation with X'. The second term denotes the macroscopic cross section calculated by the depletion calculation on the base condition with X_{base}.

Note that the variations of macroscopic cross sections depend not only on the corresponding core state variable but also on other core state variables, as described in the previous section. Therefore, the cross term effect should be considered if it considerably affects the macroscopic cross sections. In this Chapter, I consider the dependences of macroscopic cross sections on the void fraction, the fuel temperature, the moderator temperature, and the control rod insertion, which are the typical core state variables in BWR cores. However, it is impractical to directly treat such dependences of macroscopic cross sections (*i.e.*, a four dimensional tabulation of macroscopic cross sections) since the macroscopic cross section model would become complicated. Therefore, it is necessary to approximate the dependences of macroscopic cross sections on the core state variables in order to simplify the macroscopic cross section model.

On BWR normal operation, I can separate the cross term effect for the following conditions:

(1) The moderator temperature is constant at 559K, which is the bulk boiling condition. In this condition, the void fraction, the fuel temperature, and the control rod insertion would change.

(2) The moderator temperature is lower than 559K. In this condition, I assume that the void fraction is constant at 0% and the fuel temperature, the moderator temperature, and the

control rod insertion would change.

By separating the cross term effect as described above, I can tabulate the macroscopic cross sections for the instantaneous effect in the following two types of three dimensional tabulations:

- Void fraction, fuel temperature, and control rod insertion (Moderator temperature: fixed to 559K).
- Fuel temperature, moderator temperature, and control rod insertion (Void fraction: fixed to 0%).

Then, I can approximate the second term in the right hand side of Equation (3.2) as:

$$\begin{aligned}&\Delta\Sigma_{inst}(EXP,VOI,TFU,TMO,CR)\\&\approx\Delta\Sigma(EXP,VOI_{base}\rightarrow VOI,TFU_{base}\rightarrow TFU,TMO_{base},CR_{base}\rightarrow CR)\end{aligned}\tag{3.4}$$

or

$$\begin{aligned}&\Delta\Sigma_{inst}(EXP,VOI,TFU,TMO,CR)\\&\approx\Delta\Sigma(EXP,VOI_{0\%},TFU_{base}\rightarrow TFU,TMO_{base}\rightarrow TMO,CR_{base}\rightarrow CR)\end{aligned}\tag{3.5}$$

If the moderator temperature is constant at 559K, I use Equation (3.4) to approximate the second term in the right hand side of Equation (3.2). The term in the right hand side of Equation (3.4) considers the cross term effect among the void fraction, the fuel temperature, and the control rod insertion, in which the moderator temperature is fixed to 559K. If the moderator temperature is lower than 559K, I use Equation (3.5) instead of using Equation (3.4). The term in the right hand side of Equation (3.5) considers the cross term effect among the fuel temperature, the moderator temperature, and the control rod insertion, in which the void fraction is fixed to 0%.

In order to accurately estimate the variations of macroscopic cross sections due to the instantaneous effect, several branch calculations, in which some core state variables are simultaneously changed from the base condition, are carried out and the cross term effects among the core state variables are considered. The branch calculation cases used in this Chapter are shown in **Table 3-1**.

Table 3-1 Branch calculation cases used in Chapter 3

No.	Type	CR	VOI[%]	TFU[K]	TMO[K]	Depletion/Branch
0	BASE	out	40.0	800.0	559.0	Depletion
1	VOI	out	0.0	800.0	559.0	Branch from No. 0
2	VOI	out	30.0	800.0	559.0	Branch from No. 0
3	VOI	out	50.0	800.0	559.0	Branch from No. 0
4	VOI	out	80.0	800.0	559.0	Branch from No. 0
5	VOI/TFU	out	0.0	600.0	559.0	Branch from No. 0
6	VOI/TFU	out	0.0	1100.0	559.0	Branch from No. 0
7	VOI/TFU	out	30.0	600.0	559.0	Branch from No. 0
8	VOI/TFU	out	30.0	1100.0	559.0	Branch from No. 0
9	VOI/TFU	out	50.0	600.0	559.0	Branch from No. 0
10	VOI/TFU	out	50.0	1100.0	559.0	Branch from No. 0
11	VOI/TFU	out	80.0	600.0	559.0	Branch from No. 0
12	VOI/TFU	out	80.0	1100.0	559.0	Branch from No. 0
13	CR/VOI	in	0.0	800.0	559.0	Branch from No. 0
14	CR/VOI	in	30.0	800.0	559.0	Branch from No. 0
15	CR/VOI	in	50.0	800.0	559.0	Branch from No. 0
16	CR/VOI	in	80.0	800.0	559.0	Branch from No. 0
17	CR/VOI/TFU	in	0.0	600.0	559.0	Branch from No. 0
18	CR/VOI/TFU	in	0.0	1100.0	559.0	Branch from No. 0
19	CR/VOI/TFU	in	30.0	600.0	559.0	Branch from No. 0
20	CR/VOI/TFU	in	30.0	1100.0	559.0	Branch from No. 0
21	CR/VOI/TFU	in	50.0	600.0	559.0	Branch from No. 0
22	CR/VOI/TFU	in	50.0	1100.0	559.0	Branch from No. 0
23	CR/VOI/TFU	in	80.0	600.0	559.0	Branch from No. 0
24	CR/VOI/TFU	in	80.0	1100.0	559.0	Branch from No. 0
25	VOI/TMO	out	0.0	800.0	540.0	Branch from No. 0
26	VOI/TFU/TMO	out	0.0	600.0	540.0	Branch from No. 0
27	VOI/TFU/TMO	out	0.0	1100.0	540.0	Branch from No. 0
28	CR/VOI/TMO	in	0.0	800.0	540.0	Branch from No. 0
29	CR/VOI/TFU/TMO	in	0.0	600.0	540.0	Branch from No. 0
30	CR/VOI/TFU/TMO	in	0.0	1100.0	540.0	Branch from No. 0

In Table 3-1, the case of No. 0 is the depletion calculation on the base condition. The cases from No. 1 to No. 30 are the branch calculations from the case of No. 0 and the core state variables described in the "Type" column are changed. The core state variables of the cases from No. 1 to No. 12 and from No. 13 to No. 24, and from No. 25 to No. 27 and from No. 28 to No. 30 are the same except for the control rod insertion, respectively. The cases from No. 0 to No. 24 in Table 3-1 are used to estimate the second term in the right hand side of Equation (3.2) with Equation (3.4). On the other hand, the cases of No. 0 and from No. 25 to No. 30 in Table 3-1 are used to estimate the second term in the right hand side of Equation (3.2) with Equation (3.5).

The verifications and the discussions of the treatment of cross term effects among the core state variable, which are shown in this section, are described in the section 3.3.2.2.

3.2.4. History effect

The core state variables are continuously changing during the burnup and have influence on the variations of fuel composition as described in section 3.2.3. Thus, the macroscopic cross sections may be different due to the variations of fuel composition even if the core state variables are the same at one exposure point. Such cumulative effect of core state variables is called as the history effect.

In order to capture the history effect, some exposure-averaged core state variables are considered as the indices as:

$$\overline{X}(EXP) = \frac{\int_0^{EXP} X(EXP')\, w(EXP', EXP)\, dEXP'}{\int_0^{EXP} w(EXP', EXP)\, dEXP'}, \tag{3.6}$$

where, $\overline{X}$ is the exposure-averaged value of the core state variable X. In particular, the void fraction, the fuel temperature, the moderator temperature, and the control rod insertion depend on the exposure [13]. In Equation (3.6), w is the weight function, which reflects the decay effect of the core state variable X, especially for the control rod insertion. Note that I have not yet considered the decay effect, thus I use $w(EXP', EXP) = 1$ in this Chapter. Improvement of the weight function in Equation (3.6) would be an open issue to be addressed in future study.

The neutron spectrum also depends on the exposure. Therefore, in the conventional advanced nodal methods and the pin-by-pin core calculations for PWR, the spectral history (SH) has been successfully used as the history indices to capture the history effect. The SH is defined as:

$$SH(EXP) \equiv \frac{\int_0^{EXP} \frac{SI(EXP')_{off-nominal}}{SI(EXP')_{nominal}} dEXP'}{\int_0^{EXP} dEXP'}, \tag{3.7}$$

where, the subscripts *nominal* and *off-nominal* represent the depletion calculations on the base and other conditions, respectively [1, 2]. *SI* is the spectral index and is defined as:

$$SI(EXP) \equiv \frac{\phi_{fast}(EXP)}{\phi_{thermal}(EXP)}, \tag{3.8}$$

where, the subscripts *fast* and *thermal* represent the fast and the thermal energies, respectively, in which 0.625eV has been traditionally used as the energy boundary between the fast and the thermal energies. From Equations (3.7) and (3.8), the SH is the exposure-averaged value of the SI.

In the conventional advanced nodal methods and the pin-by-pin core calculations for PWR, the variations of macroscopic cross sections due to the history effect are treated by a unified approach using the exposure and the SH (e.g., the variations of macroscopic cross sections are expressed as the function of the exposure and the SH) [1, 2, 8]. In this manner, the third term in the right hand side of Equation (3.2) is described as:

$$\begin{aligned} &\Delta\Sigma_{hist}(EXP, HVOI, HTFU, HTMO, HCR) \\ &\approx \Delta\Sigma(EXP, SH) \end{aligned}. \tag{3.9}$$

However, in the BWR pin-by-pin fine mesh core calculations, the unified approach using the SH may have some difficulties described as follows. In BWR cores, there is the large variation of the neutron spectrum due to the void fraction and the exposure distributions within fuel assemblies and the control rod insertion into the water gaps between fuel assemblies.

In nature, several history effects (*e.g.*, the void history, the fuel temperature history, the moderator temperature history, and the control rod history) are included in the SH. Therefore, I can consider the variation of macroscopic cross sections for the history effect, which corresponds the third term in the right hand side of Equation (3.2), as the function of the cumulative effects of core state variables, which are represented by the exposure-averaged core state variables as:

$$\begin{aligned}&\Delta\Sigma_{hist}\left(EXP, HVOI, HTFU, HTMO, HCR\right)\\&\approx \Delta\Sigma\left(EXP, \overline{VOI}, \overline{TFU}, \overline{TMO}, \overline{CR}\right)\end{aligned}, \tag{3.10}$$

where, $\overline{VOI}$, $\overline{TFU}$, $\overline{TMO}$, and $\overline{CR}$ are the exposure-averaged void fraction, fuel temperature, moderator temperature, and control rod insertion, respectively, and they are calculated by Equation (3.6).

The correction term for the history effect, which is the third term in the right hand side of Equation (3.2), is estimated by the depletion and the branch calculations. The overview of the relationship between the correction term for the history effect and the depletion and the branch calculations is shown in **Figure 3.4**. In Figure 3.4, the core state variables of the depletion calculation on other condition and the branch calculation are the same.

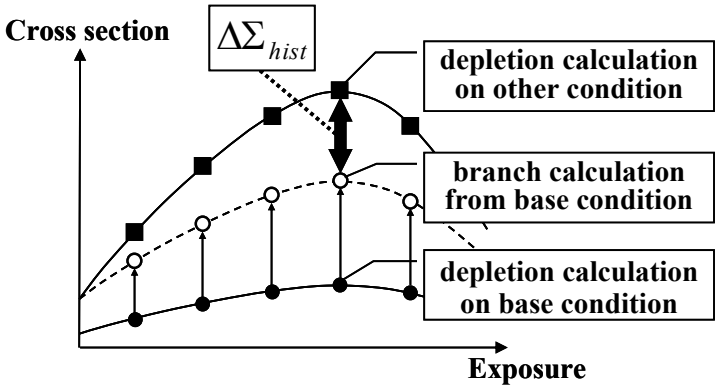

Figure 3.4 Overview of relationship between correction term for history effect and depletion and branch calculations

When one of the cumulative effects of core state variables is different from the base condition, the variations of macroscopic cross sections (i.e., the delta cross sections) are estimated by:

$$\Delta\Sigma_{hist}\left(EXP,\overline{X'}\right)=\Sigma_{depletion}\left(EXP,\overline{X'}\right)-\Sigma_{branch}\left(EXP,X'\right), \tag{3.11}$$

where, the subscripts *depletion* and *branch* represent the depletion calculation and the branch calculation from the base depletion calculation, respectively. The left hand side of Equation (3.11) is the delta cross section due to the variation of the cumulative effect of core state variable X from the base condition X_{base}. The first term in the right hand side is the macroscopic cross section calculated by the depletion calculation with the core state variable X'. The second term is the macroscopic cross section calculated by the branch calculation with the core state variable X'.

In BWR cores, the void and the control rod histories are the most dominant history effects. The cumulative effects of core state variables depend not only on the history of corresponding core state variable but also on that of other core state variables. Namely, the cross term effect is also considered for the history effect. Therefore, in order to estimate the variations of macroscopic cross sections for the history effect, several depletion calculations, in which some core state variables are simultaneously changed from the base condition, are carried out in addition to the branch calculations shown in Table 3-1. The depletion calculation cases used in this Chapter are shown in **Table 3-2**.

Table 3-2 Depletion calculation cases used in Chapter 3

No.	Type	CR	VOI[%]	TFU[K]	TMO[K]	Depletion/Branch
0	BASE	out	40.0	800.0	559.0	Depletion
1	HVOI	out	0.0	800.0	559.0	Depletion
2	HVOI	out	30.0	800.0	559.0	Depletion
3	HVOI	out	50.0	800.0	559.0	Depletion
4	HVOI	out	80.0	800.0	559.0	Depletion
5	HVOI/HTFU	out	0.0	600.0	559.0	Depletion
6	HVOI/HTFU	out	0.0	1100.0	559.0	Depletion
7	HVOI/HTFU	out	30.0	600.0	559.0	Depletion
8	HVOI/HTFU	out	30.0	1100.0	559.0	Depletion
9	HVOI/HTFU	out	50.0	600.0	559.0	Depletion
10	HVOI/HTFU	out	50.0	1100.0	559.0	Depletion
11	HVOI/HTFU	out	80.0	600.0	559.0	Depletion
12	HVOI/HTFU	out	80.0	1100.0	559.0	Depletion
13	HCR/HVOI	in	0.0	800.0	559.0	Depletion
14	HCR/HVOI	in	30.0	800.0	559.0	Depletion
15	HCR/HVOI	in	50.0	800.0	559.0	Depletion
16	HCR/HVOI	in	80.0	800.0	559.0	Depletion
17	HCR/HVOI/HTFU	in	0.0	600.0	559.0	Depletion
18	HCR/HVOI/HTFU	in	0.0	1100.0	559.0	Depletion
19	HCR/HVOI/HTFU	in	30.0	600.0	559.0	Depletion
20	HCR/HVOI/HTFU	in	30.0	1100.0	559.0	Depletion
21	HCR/HVOI/HTFU	in	50.0	600.0	559.0	Depletion
22	HCR/HVOI/HTFU	in	50.0	1100.0	559.0	Depletion
23	HCR/HVOI/HTFU	in	80.0	600.0	559.0	Depletion
24	HCR/HVOI/HTFU	in	80.0	1100.0	559.0	Depletion
25	HVOI/HTMO	out	0.0	800.0	540.0	Depletion
26	HVOI/HTFU/HTMO	out	0.0	600.0	540.0	Depletion
27	HVOI/HTFU/HTMO	out	0.0	1100.0	540.0	Depletion
28	HCR/HVOI/HTMO	in	0.0	800.0	540.0	Depletion
29	HCR/HVOI/HTFU/HTMO	in	0.0	600.0	540.0	Depletion
30	HCR/HVOI/HTFU/HTMO	in	0.0	1100.0	540.0	Depletion

In Table 3-2, the case of No. 0 is the depletion calculation on the base condition. The cases from No. 1 to No. 30 are also the depletion calculations; however, the core state variables of them are the same with those of the cases from No. 1 to No. 30 in Table 3-1. The core state variables of the cases from No. 1 to No. 12 and from No. 13 to No. 24, and from No. 25 to No. 27 and from No. 28 to No. 30 are the same except for the control rod insertion, respectively.

The treatment of cross term effect for the history effect is similar to that for the instantaneous effect described in the previous section. Namely, I separate the cross term effect among the depletion history variables for following conditions:

(1) The exposure-averaged moderator temperature is constant at 559K. In this condition, the exposure-averaged void fraction, the exposure-averaged fuel temperature, and the exposure-averaged control rod insertion would change.

(2) The exposure-averaged moderator temperature is lower than 559K. In this condition, I assume that the exposure-averaged void fraction is constant at 0% and the exposure-averaged fuel temperature, the exposure-averaged moderator temperature, and the exposure-averaged control rod insertion would change.

By separating the cross term effect as described above, I tabulate the macroscopic cross sections for the history effect in following two types of three dimensional tabulations:

- Void, fuel temperature, and control rod histories (Exposure-averaged moderator temperature: fixed to 559K).
- Fuel temperature, moderator temperature, and control rod histories (Exposure-averaged void fraction: fixed to 0%).

The verifications and the discussions of the treatment of cross term effect among the depletion history variable, which are shown in this section, are also described in the section 3.3.2.2.

3.2.5. Simplified xenon feedback

The accumulations of the particular fission product nuclides, which have short half-life and large absorption cross sections, have large impacts on the accuracies of core calculations. In the conventional macroscopic cross section model, the cumulative effects of ^{135}I, ^{135}Xe, ^{149}Pm, and ^{149}Sm are treated in a microscopic manner.

I consider steady operation conditions (*i.e.*, core power level is constant) in this Chapter. Under the steady operation conditions, the accumulation of ^{135}Xe can be considered as an equilibrium condition in each exposure point. However, since the absorption cross section of ^{135}Xe is large and ^{135}Xe has a large impact on core characteristics, the cumulative effect of ^{135}Xe is treated in a microscopic manner. Namely, the microscopic absorption cross section of ^{135}Xe is tabulated in addition to the macroscopic cross sections and the number density of ^{135}Xe is approximately calculated from the absolute fission rate density.

The effective fission yield of ^{135}Xe is estimated as:

$$\overline{\gamma_X} = \frac{N_X\left(\lambda_X + \sum_g \sigma_{a,X}\phi_g\right)}{\sum_g \Sigma_{f,g}\phi_g}, \tag{3.12}$$

where, $\overline{\gamma}$, N, λ, σ_a, Σ_f, and ϕ are the effective fission yield, the number density, the decay constant, the microscopic absorption cross section, the macroscopic fission cross section, and the neutron flux, respectively. The subscript X represents the ^{135}Xe. The effective fission yield of ^{135}Xe calculated by Equation (3.12) is also tabulated.

Note that the microscopic absorption cross section and the effective fission yield of ^{135}Xe are similarly tabulated as the macroscopic cross sections. They are also tabulated for the core state and the depletion history variables (*i.e.*, the exposure, the void fraction, the fuel temperature, the moderator temperature, the control rod insertion, the void history, the fuel temperature history, the moderator temperature history, and the control rod history) and the treatments of these variables are the same with the macroscopic cross sections described in sections from 3.2.2 to 3.2.4.

3.3. Numerical calculations

3.3.1. Calculation conditions

In order to verify the present macroscopic cross section model for BWR pin-by-pin core analysis, which is described in the previous section, benchmark calculations are carried out in typical BWR fuel assemblies shown in **Figure 3.5** [14, 15]. The fuel rod enrichment distributions within each fuel

assemblies are decided in Chapter 2. The pin-cell averaged cross sections used in this Chapter are calculated by the HELIOS code in 8 energy groups, which are collapsed from 47 energy groups [16]. Note that the 8 group structure shown in **Table 3-3** is slightly modified in order to be consistent with the energy boundaries described in the references [6] and [7]. The exposure points, which are used in the depletion calculations by the HELIOS code, are shown in **Table 3-4**. Note that the exposure points, which are shown in Table 3-4 as shaded area, are used to establish the present macroscopic depletion model (i.e., they are used as the standard exposure points as described in the section 3.2.2).

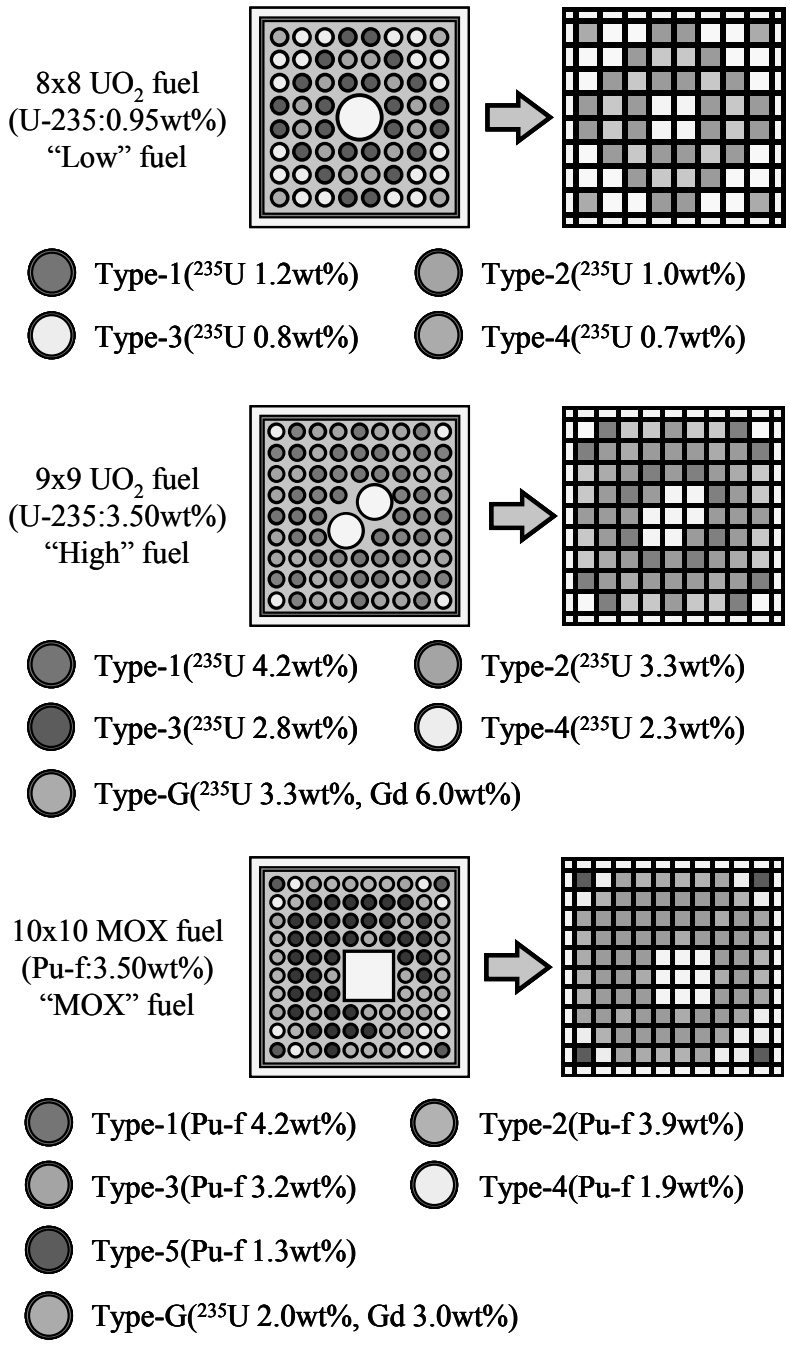

Figure 3.5 Geometries of typical BWR fuel assemblies

Table 3-3 Energy group structure

Group	Upper [eV]	Lower [eV]
1	2.0000E+07	2.2313E+06
2	2.2313E+06	8.2085E+06
3	8.2085E+06	9.1188E+03
4	9.1188E+03	1.3007E+02
5	1.3007E+02	3.9279E+00
6	3.9279E+00	6.2506E-01
7	6.2506E-01	1.4572E-01
8	1.4572E-01	1.0000E-04

Table 3-4 Exposure points for HELIOS and verification calculations

Exposure Points for HELIOS and Verification Calculations									
0.0	0.1	0.2	0.3	0.4	0.5	0.6	0.7	0.8	0.9
1.0	1.5	2.0	2.5	3.0	3.5	4.0	4.5	5.0	5.5
6.0	6.5	7.0	7.5	8.0	8.5	9.0	9.5	10.0	10.5
11.0	11.5	12.0	12.5	13.0	13.5	14.0	14.5	15.0	15.5
16.0	16.5	17.0	17.5	18.0	18.5	19.0	19.5	20.0	21.0
22.0	23.0	24.0	25.0	26.0	27.0	28.0	29.0	30.0	31.0
32.0	33.0	34.0	35.0	36.0	37.0	38.0	39.0	40.0	41.0
42.0	43.0	44.0	45.0	46.0	47.0	48.0	49.0	50.0	51.0
52.0	53.0	54.0	55.0	56.0	57.0	58.0	59.0	60.0	61.0
62.0	63.0	64.0	65.0	66.0	67.0	68.0	69.0	70.0	71.0
72.0	73.0	74.0	75.0	76.0	77.0	78.0	79.0	80.0	[GWd/t]

In order to prepare the pin-cell averaged macroscopic cross sections to various conditions, various combinations of core state variables should be covered by depletion and branch calculations. The case matrix (*i.e.*, the list of depletion and branch calculations), which is used to establish the present macroscopic depletion model, is already shown in Tables 3-1 and 3-2. The pin-cell averaged

macroscopic cross sections are generated according to the case matrix and they are edited and tabulated as the base and the delta cross sections described in section 3.2. In order to reduce the spatial homogenization and the energy collapsing errors, the superhomogenization (SPH) method is applied for each pin-cell averaged cross sections [17].

The SPH factor also depends on the core state and the depletion history variables as the cross sections and it is very important to appropriately estimate such dependencies from the viewpoint of the calculation accuracy. Thus, the SPH factor should be independently considered for each pin-cell. However, the tabulation of the SPH factor requires an additional computational memory. Therefore, in order to reduce memory requirement, the cross sections and the SPH factor are not independently tabulated, but the SPH-corrected cross sections, which are calculated by multiplying the cross sections by the SPH factor, are directly tabulated in this Chapter.

The accuracy of the present macroscopic cross section model described in section 3.2 is confirmed by comparing the calculation results obtained by the tabulated and the reference cross sections. The tabulated cross sections are reconstructed by the present macroscopic cross section model. The reference cross sections are obtained by the lattice physics calculations, in which the values of core state variable on the benchmark calculation cases are directly used. The benchmark calculation cases, which are used for the verifications of depletion calculations, are shown in the sections 3.3.2.1, 3.3.2.2, and 3.3.2.3, respectively.

In the benchmark calculations, I directly treat the exposure distribution within fuel assemblies but the void fraction and the fuel temperature distributions are assumed as uniform. From the reference [18], the effect of the pin-by-pin fuel temperature distribution is considered to be small. Thus, necessity of direct treatment of pin-by-pin fuel temperature distribution would be low. On the other hand, in-channel void distribution has large effect on the calculation results (*e.g.*, the k-infinity and the pin-by-pin fission rate distribution) [19]. Consideration of in-channel void distribution is out of the scope of this Chapter but it is an important issue to be addressed in future study.

The pin-by-pin (cell-homogenized) calculations are carried out by the SUBARU code, which is a pin-by-pin core analysis code for BWR under development [20]. The SUBARU code utilizes the semi-analytic nodal method with the simplified P3 (SP3) theory and explicitly models each homogenized pin-cell. The k-infinities, the pin-by-pin fission rate distributions, and the pin-wise exposure

distributions within the fuel assembly, which are obtained with the tabulated and the reference cross sections, are compared. The absolute value of relative difference of k-infinity, the root-mean-square (RMS) difference of pin-by-pin fission rate distribution, and the RMS difference of pin-wise exposure distribution are calculated as:

$$\Delta k_{inf} = \left| 1 - \frac{k_{inf}^{tabulated}}{k_{inf}^{reference}} \right|, \tag{3.13}$$

$$\Delta R_{f,RMS} = \sqrt{\frac{\sum_{i \in fuel\,mesh} \left(R_{f,i}^{tablulated} - R_{f,i}^{reference} \right)^2}{N_{fuel\,mesh}}}, \tag{3.14}$$

$$\Delta EXP_{RMS} = \sqrt{\frac{\sum_{i \in fuel\,mesh} \left(1 - EXP_i^{tablulated} / EXP_i^{reference} \right)^2}{N_{fuel\,mesh}}}, \tag{3.15}$$

where, Δk_{inf}, $\Delta R_{f,RMS}$, ΔEXP_{RMS}, $R_{f,i}$, EXP_i, and $N_{fuelmesh}$ are the absolute value of relative difference of k-infinity, the RMS difference of pin-by-pin fission rate distribution, the RMS difference of pin-wise exposure distribution, the fission rate on fuel mesh i, the exposure of fuel mesh i, and the number of fuel mesh, respectively. The superscripts *tabulated* and *reference* represent the calculations with the tabulated and the reference cross sections, respectively.

The target accuracies for the absolute value of relative difference of k-infinity and the RMS difference of pin-by-pin fission rate distribution in this Chapter are as the follows:

- Absolute value of relative difference of k-infinity is less than 0.1%dk/k.
- RMS difference of pin-by-pin fission rate distribution is less than 0.3%.

In conventional BWR core analysis, the target accuracy of k-infinity is approximately 0.4%dk/k from the viewpoint of prediction accuracy of reactor shutdown margin. Similarly, the target accuracy of power distribution is generally considered as 10%. In this Chapter, the verification calculations are carried out in single assembly geometries without thermal-hydraulic feedback. Therefore, I set the target accuracies as described the above, which are sufficiently smaller than those for general BWR core

analysis.

In this Chapter, I focus on the absolute value of relative difference of k-infinities and the RMS difference of pin-by-pin fission rate distributions, which are obtained by the SUBARU code with the tabulated and the reference cross sections in order to discuss only the accuracy of the present macroscopic cross section model. However, I also compared the calculation results of the HELIOS code and the SUBARU code. The absolute value of relative difference of k-infinities and the RMS difference of pin-by-pin fission rate distributions, which are estimated by the HELIOS code and the SUBARU code with the reference cross sections, are less than approximately 0.02%dk/k and 0.02%, respectively, on the "BASE" depletion calculation cases as shown in Tables 3-1 and 3-2. Therefore, the SUBARU code with the reference cross sections well reproduces the calculation results obtained by the HELIOS code.

3.3.2. Calculation results and remarks

3.3.2.1. Treatment of exposure

Since the exposure has dominant effect on the macroscopic cross sections, the macroscopic cross sections are independently tabulated for different exposure points. The macroscopic cross sections are interpolated for exposure points, which are calculated in macroscopic depletion calculations, by utilizing the CSI as described in the section 3.2.2.

In order to confirm the calculation accuracies of the exposure distribution and the interpolation of macroscopic cross sections, I use the following three types of cross sections and compare the calculation results:

- The reference cross sections: cross sections are directly obtained by the HELIOS code. The present cross sections give most accurate (reference) results.
- The tabulated cross sections with the reference exposure distribution: cross sections are reconstructed from the present macroscopic cross section model with the reference exposure distribution. The present cross sections will reveal the impact of errors due to the CSI for the exposure by comparing the calculation results by "the reference cross sections".
- The tabulated cross sections: cross sections are reconstructed from the present macroscopic cross section model with the exposure distribution calculated in the macroscopic depletion

calculation. The present cross sections will reveal the impact of errors due to the macroscopic depletion calculations, in which the exposure distribution is calculated, by comparing the calculation results by "the tabulated cross sections with the reference exposure distribution".

The benchmark calculation cases are shown in **Table 3-5**.

Table 3-5 Benchmark calculation cases (exposure)

No.	Type	CR	VOI[%]	TFU[K]	TMO[K]	Depletion/Branch
1	HVOI/HTFU	out	80.0	1100.0	559.0	Depletion
2	HVOI/HTFU/HTMO/HCR	in	0.0	600.0	540.0	Depletion

In Table 3-5, the core state and the depletion history variables of the benchmark calculation cases are the same as those of the depletion calculation cases, which are shown in Table 3-2 and are used to establish the present macroscopic cross section model. Namely, the errors due to the polynomial interpolations for the core state and the depletion history variables do not exist. The benchmark calculation case of No. 1 corresponds to the bulk boiling condition in the core top region on BWR normal operation, in which the void fraction and the fuel temperature are high and the control rod is withdrawn. The benchmark calculation case of No. 2 corresponds to the non-boiling condition in the core bottom region on BWR normal operation, in which the fuel temperature and the moderator temperature are low and the control rod is inserted. They are the limiting cases covered in the present macroscopic cross section model. Through these benchmark calculation cases, I estimate the impact of the interpolation errors for exposure on the calculation accuracies and discuss the treatment of exposure in the present macroscopic cross section model.

The absolute value of relative difference of k-infinity, the RMS difference of pin-by-pin fission rate distribution, and the RMS difference of pin-wise exposure distribution are shown in **Figures 3.6** to **3.8**, respectively. In Figures 3.6 to 3.8, the calculation results obtained by the tabulated cross sections with the reference exposure distribution and those with the calculated exposure distribution are represented as "Case # (Reference exposure distribution)" and "Case # (Calculated exposure distribution)", respectively. In Figures 3.6 and 3.7, the lines indicating the target accuracies are also

shown.

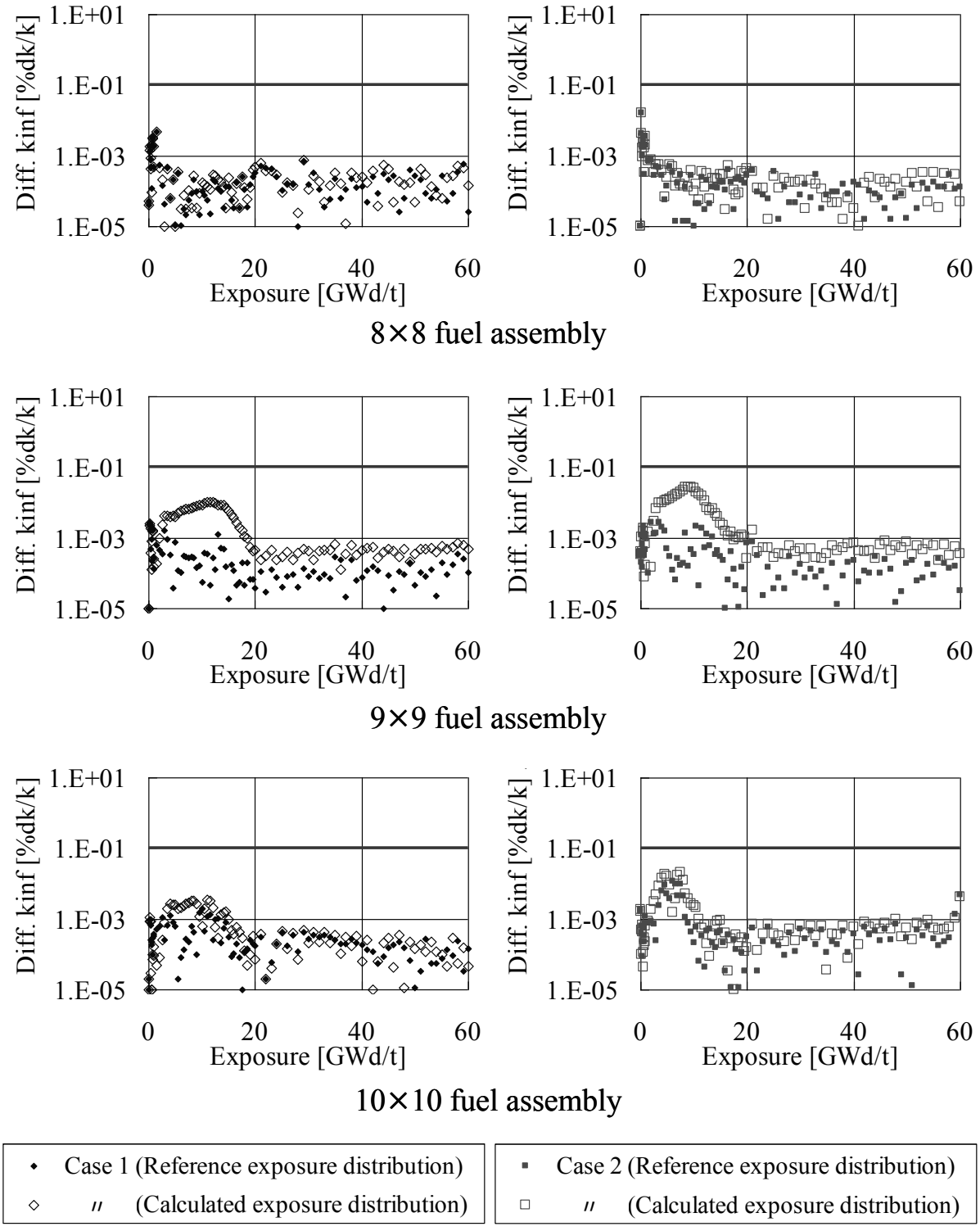

Figure 3.6 Calculation results of k-infinity (Calculation cases: Table 3-5, Target accuracy line: 0.1%dk/k)

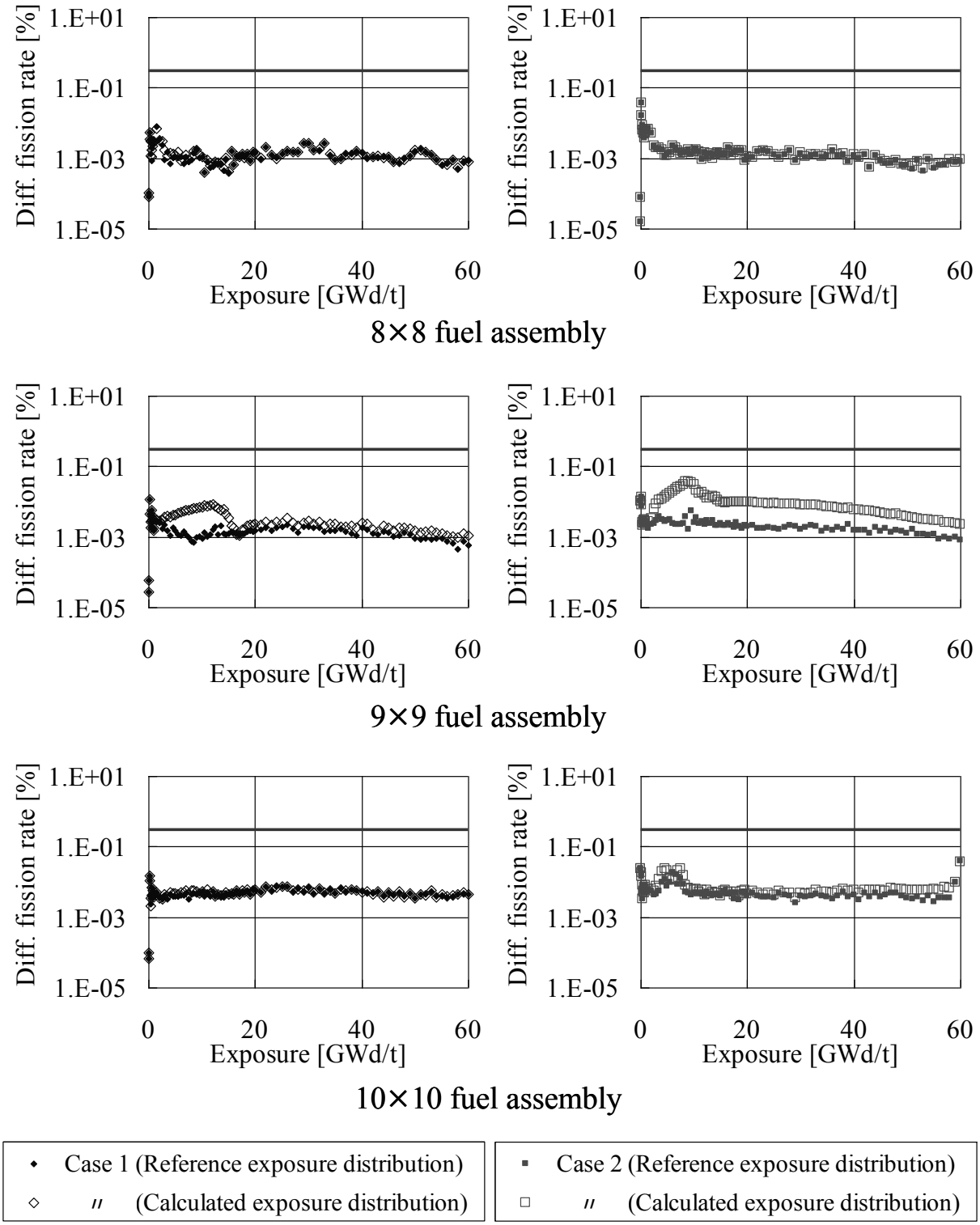

Figure 3.7 Calculation results of pin-by-pin fission rate distribution (Calculation cases: Table 3-5, Target accuracy line: 0.3%)

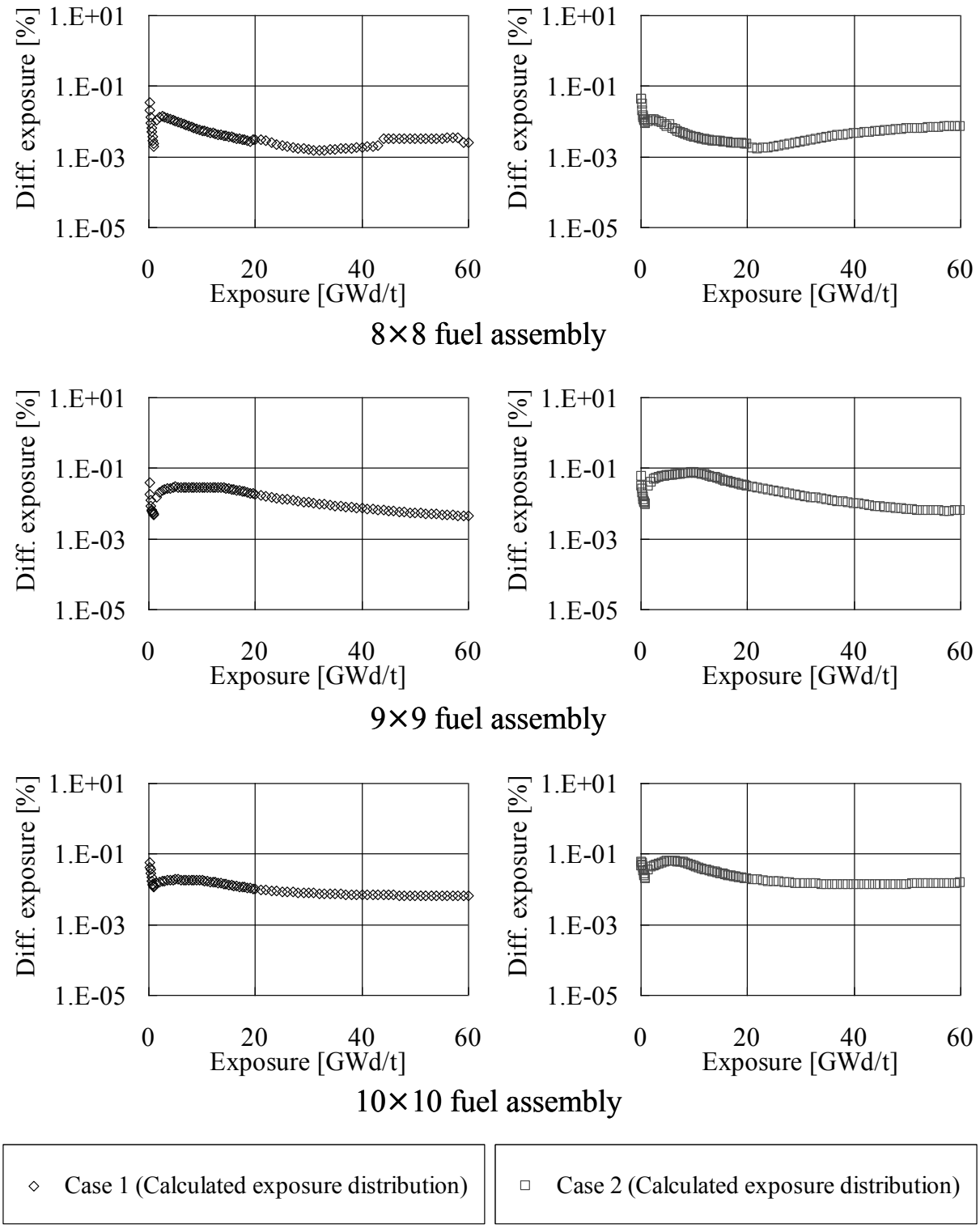

Figure 3.8 Calculation results of pin-wise exposure distribution (Calculation cases: Table 3-5)

From Figures 3.6 to 3.8, on 8×8 fuel assembly, the differences of k-infinity and pin-by-pin fission rate distribution obtained by the tabulated cross sections with the reference and the calculated exposure distribution are almost the same. On 9×9 and 10×10 fuel assemblies, those obtained by the tabulated cross sections with the calculated exposure distribution have several peaks related to the depletions of Gd-bearing fuel pin-cells around 10GWd/t since they have Gd-bearing fuel pin-cells and then become almost the same accuracies with those obtained by the tabulated cross sections with the reference exposure distribution in after 20GWd/t. Common to all types of fuel assemblies, the differences of k-infinity and pin-by-pin fission rate distribution obtained by the tabulated cross sections with the reference and the calculated exposure distribution also have several peaks around 0GWd/t. Errors due to the CSI tend to appear around limits of interpolation since the CSI requires some boundary conditions on limits of interpolation (*i.e.*, 0 and 80GWd/t) as described in the section 3.2.2 and the setup of the boundary condition has an effect on the interpolation accuracy around limits of interpolation. Therefore, such interpolation errors due to the boundary condition cause several peaks of the differences of k-infinity and pin-by-pin fission rate distribution around 0GWd/t. However, the above peak values of the differences of k-infinity and pin-by-pin fission rate distribution are less than about 0.03%dk/k and about 0.03%, respectively. Therefore, the error due to the interpolation for exposure using the CSI is small and the target macroscopic cross sections can be well reproduced.

Compared with the differences of the pin-by-pin fission rate and the exposure distributions, they show almost the same tendencies on all types of fuel assemblies. This result indicates that the errors of the pin-by-pin fission rate distribution cause the errors of the exposure distribution and then they cause the errors of the macroscopic cross sections.

3.3.2.2. Treatment of instantaneous and history effects

The macroscopic cross sections have complicated dependences on the core state and the depletion history variables. Thus, in the present macroscopic cross section model, I approximate the macroscopic cross sections as a linear combination of the macroscopic cross section on the base condition and the correction terms for the instantaneous and the history effects. Then, I separately tabulate the cross term effect for the instantaneous and the history variables according to the moderator temperature and the exposure-averaged moderator temperature as described in the sections 3.2.3 and

3.2.4.

Using the above approximations, the macroscopic cross sections for the instantaneous effect are tabulated in following two types of three dimensional tabulations:

- Void fraction, fuel temperature, and control rod insertion (Moderator temperature: fixed to 559K).
- Fuel temperature, moderator temperature, and control rod insertion (Void fraction: fixed to 0%).
- Similarly, those for the history effect are tabulated in following two types of three dimensional tabulations:
- Void, fuel temperature, and control rod histories (Exposure-averaged moderator temperature: fixed to 559K).
- Fuel temperature, moderator temperature, and control rod histories (Exposure-averaged void fraction: fixed to 0%).

In order to confirm the calculation accuracies for the dependences on the core state and the depletion history variables and evaluate the impact of the treatment of cross term effect, the following five types of cross sections are used and then the calculation results are compared:

- The reference cross sections: cross sections are directly obtained by the HELIOS code. The present cross sections give most accurate (reference) results.
- The tabulated cross sections: cross sections are reconstructed by the present macroscopic cross section model with the cross terms for the instantaneous and the history effects.
- The tabulated cross sections without cross terms for history effect: cross sections are reconstructed by the present macroscopic cross section model without and with the cross terms for the instantaneous and the history effects, respectively. The present cross sections will reveal the impact of cross term for the history effect by comparing the calculation results by “the tabulated cross section”.
- The tabulated cross sections without all cross terms: cross sections are reconstructed by the present macroscopic cross section model without all cross terms for the instantaneous and the history effects. The present cross section will reveal the impact of cross term for the instantaneous effect by comparing the calculation results by “the tabulated cross sections

without cross terms for history effect".

- The tabulated cross sections with specific cross term: cross sections are reconstructed by the present macroscopic cross section model with one of the cross term effects among the core state and the depletion history variables (*e.g.*, the void fraction and the fuel temperature, the void fraction and the control rod insertion, or the void and the control rod histories). The present cross sections will reveal the contribution of each cross term (*i.e.*, the breakdown of cross term effects).

In the following parts, the cross term effects for the two independent three-dimensional cross section tables (*i.e.*, (a) the void fraction, the fuel temperature, and the control rod insertion, (b) the fuel temperature, the moderator temperature, and the control rod insertion) are investigated.

(a) Cross term effect among void fraction, fuel temperature, control rod insertion, and their histories

Firstly, I verify the treatment of the cross term effect among the void fraction, the fuel temperature, the control rod insertion, and their histories through the benchmark calculation cases shown in **Table 3-6**.

Table 3-6 Benchmark calculation cases (void fraction, fuel temperature, control rod insertion, and their histories)

No.	Type	CR	VOI[%]	TFU[K]	TMO[K]	Depletion/Branch
3	HVOI/HTFU	out	60.0	950.0	559.0	Depletion
4	HVOI/HTFU/HCR	in	20.0	700.0	559.0	Depletion

The benchmark calculation case of No. 3 corresponds to the bulk boiling condition on BWR normal operation, in which the void fraction and the fuel temperature are high and the control rod is withdrawn. The benchmark calculation case of No. 4 also corresponds to the bulk boiling condition; however the void fraction and the fuel temperature are low and the spatial and energetic tilt of neutron spectrum due to the control rod insertion is caused. Since errors due to polynomial interpolations tend to be larger at intermediate values between interpolation points, the core state and the depletion history

variables of the benchmark calculation cases in Table 3-6 are determined as intermediate values between those of the branch and the depletion calculation cases in Table 3-1 and Table 3-2, which are used to establish the present macroscopic cross section model.

The absolute value of relative difference of k-infinity and the RMS difference of pin-by-pin fission rate distribution are shown in **Figures 3.9** and **3.10**, respectively. In Figures 3.9 and 3.10, the calculation results obtained with and without cross terms are represented as “Yes” and “No”, respectively. The lines indicating the target accuracies are also shown.

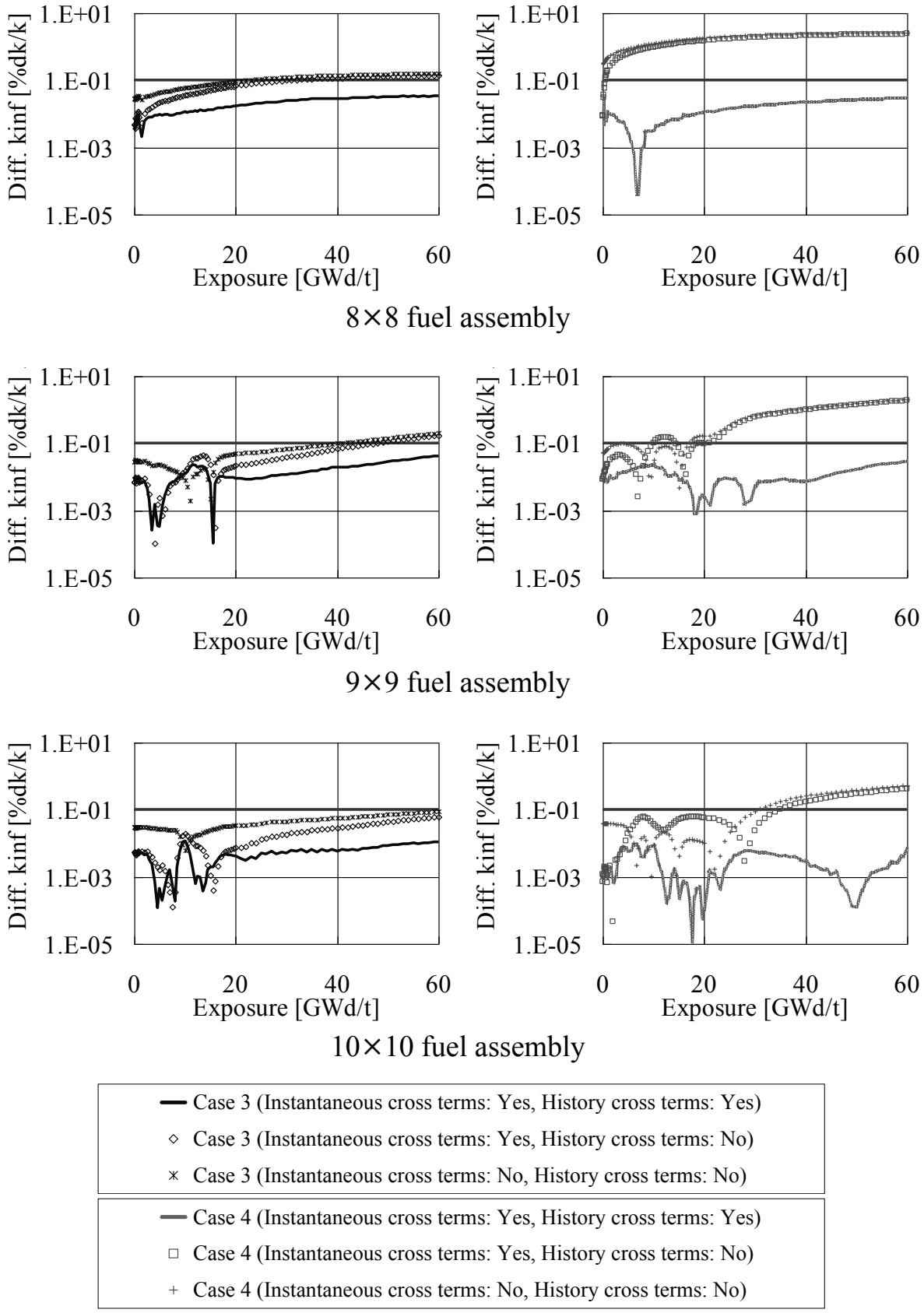

Figure 3.9 Calculation results of k-infinity (Calculation cases: Table 3-6, Target accuracy line: 0.1%dk/k)

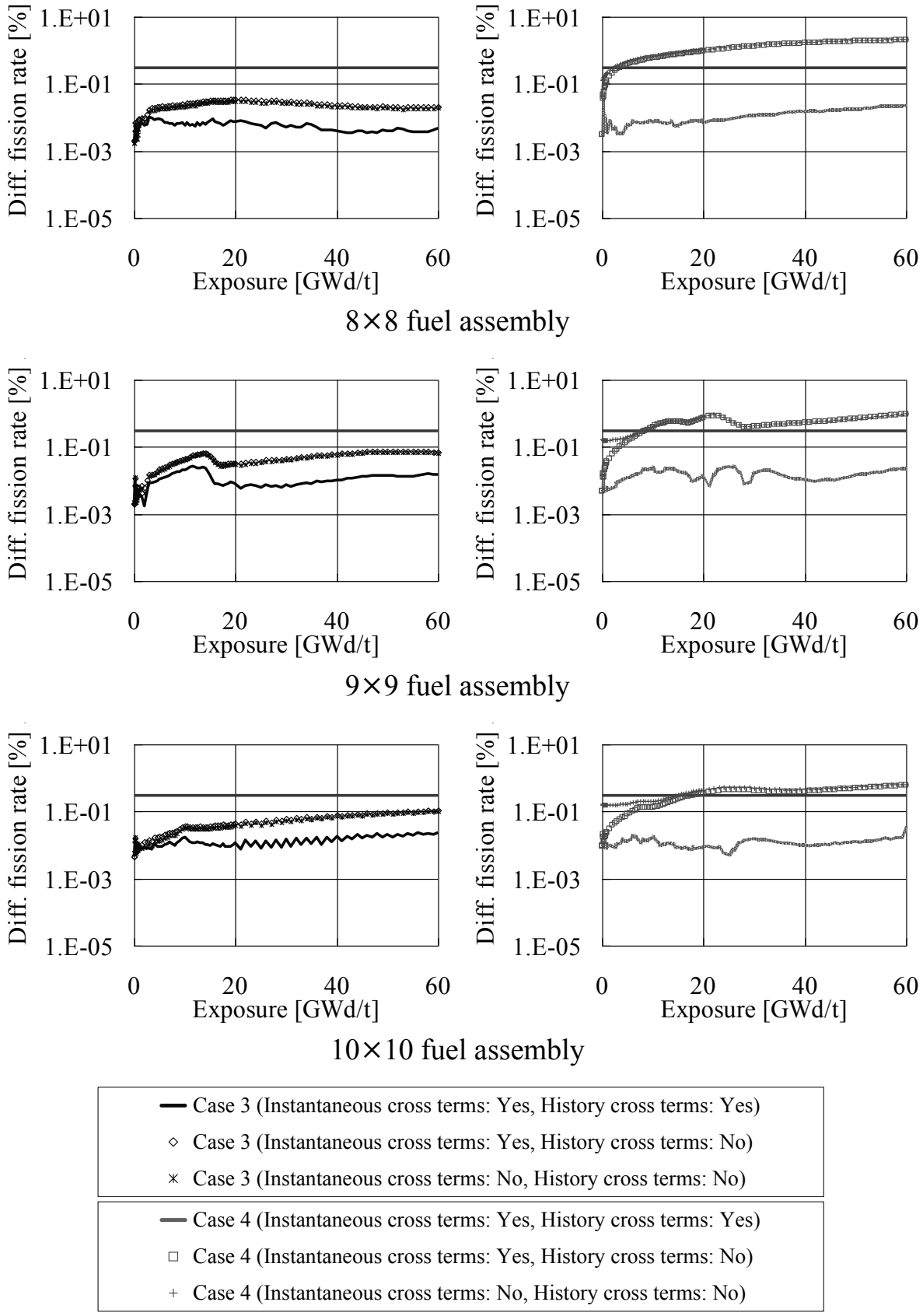

Figure 3.10 Calculation results of pin-by-pin fission rate distribution (Calculation cases: Table 3-6, Target accuracy line: 0.3%)

From Figures 3.9 and 3.10, in the benchmark calculation cases of No. 3 and No. 4, the calculation results obtained by the tabulated cross sections with all cross terms achieve the target accuracies for the differences of k-infinity and pin-by-pin fission rate distribution. The differences of k-infinity and pin-by-pin fission rate distribution become larger as the exposure becomes higher for all benchmark calculation cases. On the other hand, those shown in the previous section are mostly constant while the exposure becomes higher except for the effect of Gd. From these comparisons, the polynomial interpolations for the core state and the depletion history variables cause the errors of the macroscopic cross sections, and then they turn out the errors of the pin-by-pin fission rate distribution. Note that, given the later discussions in the next sections, the errors due to the polynomial interpolations for the void fraction and the void history especially have large impacts on the reconstruction of macroscopic cross sections.

In the benchmark calculation case of No. 3 without the control rod history, the calculation accuracies obtained by the tabulated cross sections without cross terms for history effect and those without all cross terms are worse than those obtained by the tabulated cross sections with all cross terms. The differences of k-infinity and pin-by-pin fission rate distribution obtained by the tabulated cross sections without cross terms for history effect and those without all cross terms are shown within 0.03%dk/k and 0.005%, respectively. These comparison results indicate that the impact of the cross term effect among the void fraction and the fuel temperature is small; thus such cross term effect could be negligible in the macroscopic cross section model. On the high exposure points, the differences of k-infinity obtained by the tabulated cross sections without cross terms for history effect and those without all cross terms exceed the target accuracies. Thus, the cross term effect among the void and the fuel histories is necessary to consider in the present macroscopic cross section model.

In the benchmark calculation case of No. 4 with the control rod history, the calculation accuracies obtained by the tabulated cross sections without cross terms for history effect and those without all cross terms become much worse than those obtained by the tabulated cross sections with all cross terms for all types of fuel assemblies. The differences of k-infinity and pin-by-pin fission rate distribution exceed the target accuracies on most of exposure points. These comparison results indicate that the cross term effect among the control rod insertion, the control rod history, and other core state and depletion history variables (*i.e.*, the void fraction, the fuel temperature, and their histories) is

extremely large.

In order to evaluate and discuss the necessity of the treatment of cross term effect, the benchmark calculation case of No. 4 is calculated with the tabulated cross sections without all cross terms and those with specific cross term. The evaluation results are shown in **Table 3-7**. In Table 3-7, the values are calculated by subtracting the calculation results obtained by the tabulated cross sections with specific cross term from those obtained by the tabulated cross sections without all cross terms.

Table 3-7 Impact of cross term effect among void fraction, fuel temperature, control rod insertion, and their histories (1/3)

8×8 fuel assembly

	Exposure	Instantaneous cross terms			History cross terms		
	[GWd/t]	VOI-TFU	VOI-CR	TFU-CR	HVOI-HTFU	HVOI-HCR	HTFU-HCR
Δk_{inf} [%dk/k]	0	-0.01	0.33	0.00	0.00	0.00	0.00
	10	-0.01	0.30	0.00	-0.02	0.93	0.08
	20	-0.01	0.31	0.00	-0.04	1.48	0.13
	30	-0.01	0.31	0.00	-0.05	1.84	0.16
	40	-0.01	0.32	0.00	-0.06	2.07	0.19
	50	-0.01	0.32	0.00	-0.06	2.22	0.20
	60	-0.01	0.31	0.00	-0.07	2.33	0.21
$\Delta R_{f,RMS}$ [%]	0	0.00	0.13	0.00	0.00	0.00	0.00
	10	0.00	0.10	0.00	0.01	0.52	0.05
	20	0.00	0.11	0.00	0.02	0.83	0.08
	30	0.00	0.13	0.00	0.02	1.17	0.11
	40	0.00	0.14	0.00	0.02	1.45	0.14
	50	0.00	0.15	0.00	0.03	1.65	0.17
	60	0.00	0.16	0.00	0.03	1.78	0.18

Table 3-7 Impact of cross term effect among void fraction, fuel temperature, control rod insertion, and their histories (2/3)

9×9 fuel assembly

	Exposure	Instantaneous cross terms			History cross terms		
	[GWd/t]	VOI-TFU	VOI-CR	TFU-CR	HVOI-HTFU	HVOI-HCR	HTFU-HCR
Δk_{inf} [%dk/k]	0	-0.01	0.05	0.00	0.00	0.00	0.00
	10	0.01	-0.08	0.00	0.00	-0.07	-0.01
	20	-0.01	0.08	0.00	-0.01	0.10	0.02
	30	-0.01	0.12	0.00	-0.03	0.58	0.05
	40	-0.01	0.13	0.00	-0.05	0.99	0.08
	50	-0.01	0.15	0.00	-0.08	1.43	0.12
	60	-0.01	0.17	0.00	-0.11	1.88	0.16
$\Delta R_{f,RMS}$ [%]	0	0.00	0.16	0.00	0.00	0.00	0.00
	10	0.00	0.02	0.00	-0.01	0.28	0.01
	20	0.00	0.09	0.00	-0.01	0.71	0.02
	30	0.00	0.03	0.00	0.00	0.34	0.03
	40	0.00	0.03	0.00	0.01	0.44	0.04
	50	0.00	0.02	0.00	0.02	0.55	0.05
	60	0.00	0.02	0.00	0.04	0.76	0.08

Table 3-7 Impact of cross term effect among void fraction, fuel temperature, control rod insertion, and their histories (3/3)

10×10 fuel assembly

	Exposure	Instantaneous cross terms			History cross terms		
	[GWd/t]	VOI-TFU	VOI-CR	TFU-CR	HVOI-HTFU	HVOI-HCR	HTFU-HCR
Δk_{inf} [%dk/k]	0	-0.01	0.03	0.00	0.00	0.00	0.00
	10	-0.01	-0.04	0.00	0.00	-0.05	0.00
	20	0.01	-0.06	0.00	0.01	-0.04	-0.01
	30	-0.01	0.08	0.00	-0.02	0.01	0.02
	40	-0.01	0.10	0.00	-0.03	0.16	0.03
	50	-0.01	0.12	0.00	-0.04	0.29	0.04
	60	-0.01	0.13	0.00	-0.06	0.43	0.05
$\Delta R_{f,RMS}$ [%]	0	0.00	0.15	0.00	0.00	0.00	0.00
	10	0.00	0.07	0.00	-0.01	0.04	0.01
	20	0.00	0.10	0.00	-0.01	0.29	0.01
	30	0.00	0.08	0.00	-0.01	0.37	0.02
	40	0.00	0.06	0.00	-0.02	0.31	0.04
	50	0.00	0.06	0.00	-0.02	0.38	0.05
	60	0.00	0.06	0.00	-0.02	0.46	0.06

From Table 3-7, the impacts of the cross term effect among the void fraction and the fuel temperature represented as “VOI-TFU” and that among the fuel temperature and the control rod insertion represented as “TFU-CR” are small or almost zero for all types of fuel assemblies; thus such cross term effect could be negligible in the present macroscopic cross section model. On the other hand, other cross term effects have large impacts, especially for the cross term effect among the void and the control rod histories represented as “HVOI-HCR”. The cross term effect among the void and the control rod histories has the largest impact and this impact becomes larger as the exposure becomes higher on all types of fuel assemblies. Therefore, the treatment of this cross term effect is essential to accurately reproduce the target cross sections. The cross term effect among the void fraction and the control rod insertion represented as ”VOI-CR” has the second largest impact after that among the void and the control rod histories especially on the low exposure points, which is almost the same value with that among the void and the control rod histories and the impact of this is constant for the exposure. The cross term effect among the void and the fuel temperature histories represented as “HVOI-HTFU” and that among the fuel temperature and the control rod histories represented as “HTFU-HCR” have small impacts on the low exposure points, which are about or less than a tenth part of that of the cross term effect among the void and the control rod histories. However, they become larger as the exposure becomes higher and are not be negligible from the viewpoints of the target accuracies especially on the high exposure points

Therefore, the following cross term effects have large impacts on the reconstruction of macroscopic cross sections and are necessary to consider in the present macroscopic cross section model as the following priority order:

(1) Void and control rod histories (HVOI-HCR).

(2) Void fraction and control rod insertion (VOI-CR).

(3) Fuel temperature and control rod histories (HTFU-HCR).

(4) Void and fuel temperature histories (HVOI-HTFU).

The treatment of them is important in order to accurately reproduce the target cross sections and estimate the k-infinity and the pin-by-pin fission rate distribution.

(b) Cross term effect among fuel temperature, moderator temperature, control rod insertion, and their histories

Next, the treatment of the cross term effect among the fuel temperature, the moderator temperature, the control rod insertion, and their histories is verified through the benchmark calculation cases shown in **Table 3-8**.

Table 3-8 Benchmark calculation cases (fuel temperature, moderator temperature, control rod insertion, and their histories)

No.	Type	CR	VOI[%]	TFU[K]	TMO[K]	Depletion/Branch
5	HVOI/HTFU/HTMO	out	0.0	950.0	550.0	Depletion
6	HVOI/HTFU/HTMO/HCR	in	0.0	700.0	550.0	Depletion

The benchmark calculation case of No. 5 corresponds to the non-boiling condition, in which the fuel temperature is high and the control rod is withdrawn. The benchmark calculation case of No. 6 also corresponds to the non-boiling condition; however the fuel temperature is low and the spatial and energetic tilt of neutron spectrum due to the control rod insertion is caused. The core state and the depletion history variables of the benchmark calculation cases in Table 3-8 are also determined as intermediate values between those of the branch and the depletion calculation cases in Tables 3-1 and 3-2 similarly to the benchmark calculation cases in Table 3-6.

The absolute value of relative difference of k-infinity and the RMS difference of pin-by-pin fission rate distribution are shown in **Figures 3.11** and **3.12**, respectively. In Figures 3.11 and 3.12, the calculation results obtained with and without cross terms are represented as “Yes” and “No”, respectively. The lines indicating the target accuracies are also shown.

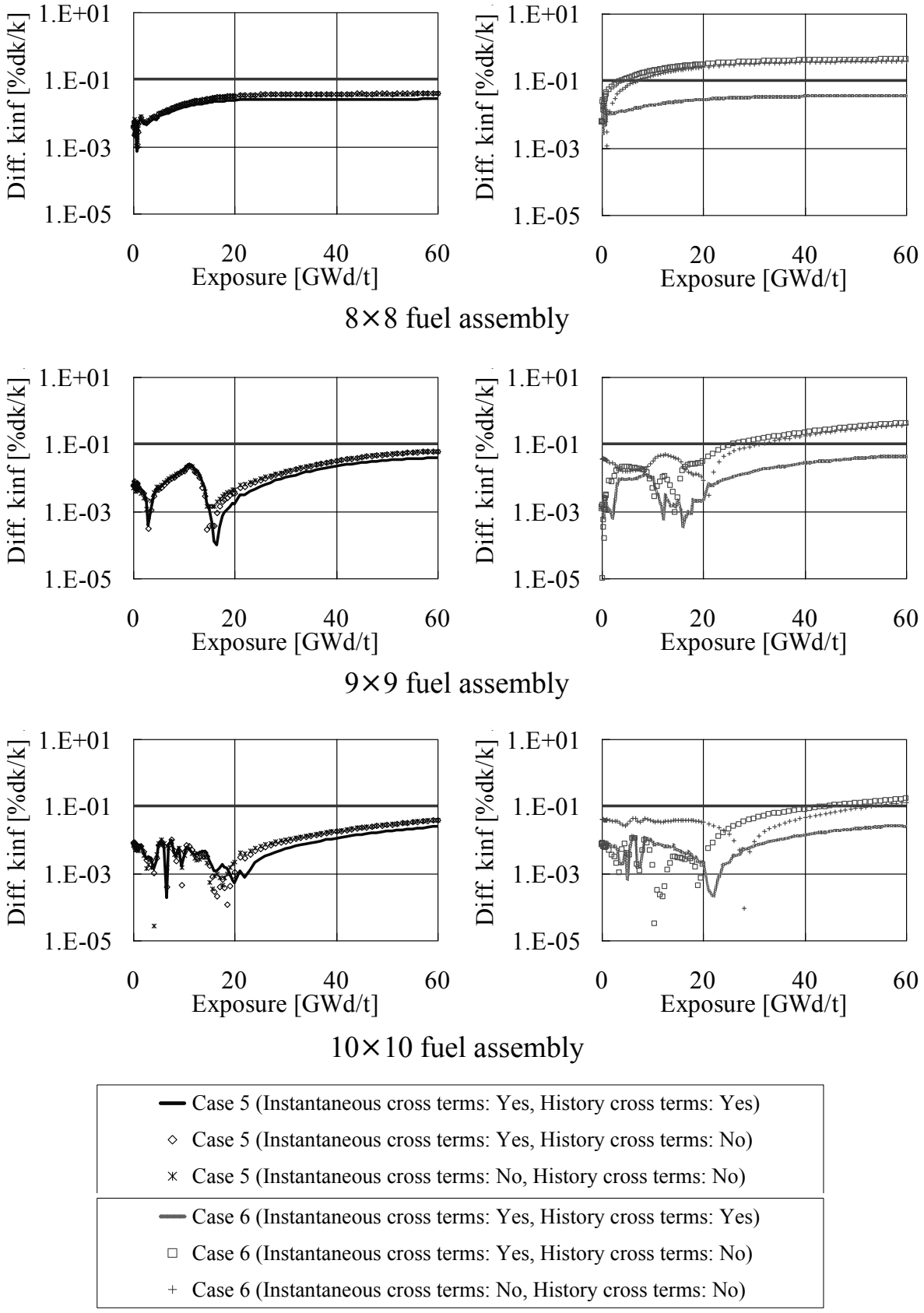

Figure 3.11 Calculation results of k-infinity (Calculation cases: Table 3-8, Target accuracy line: 0.1%dk/k)

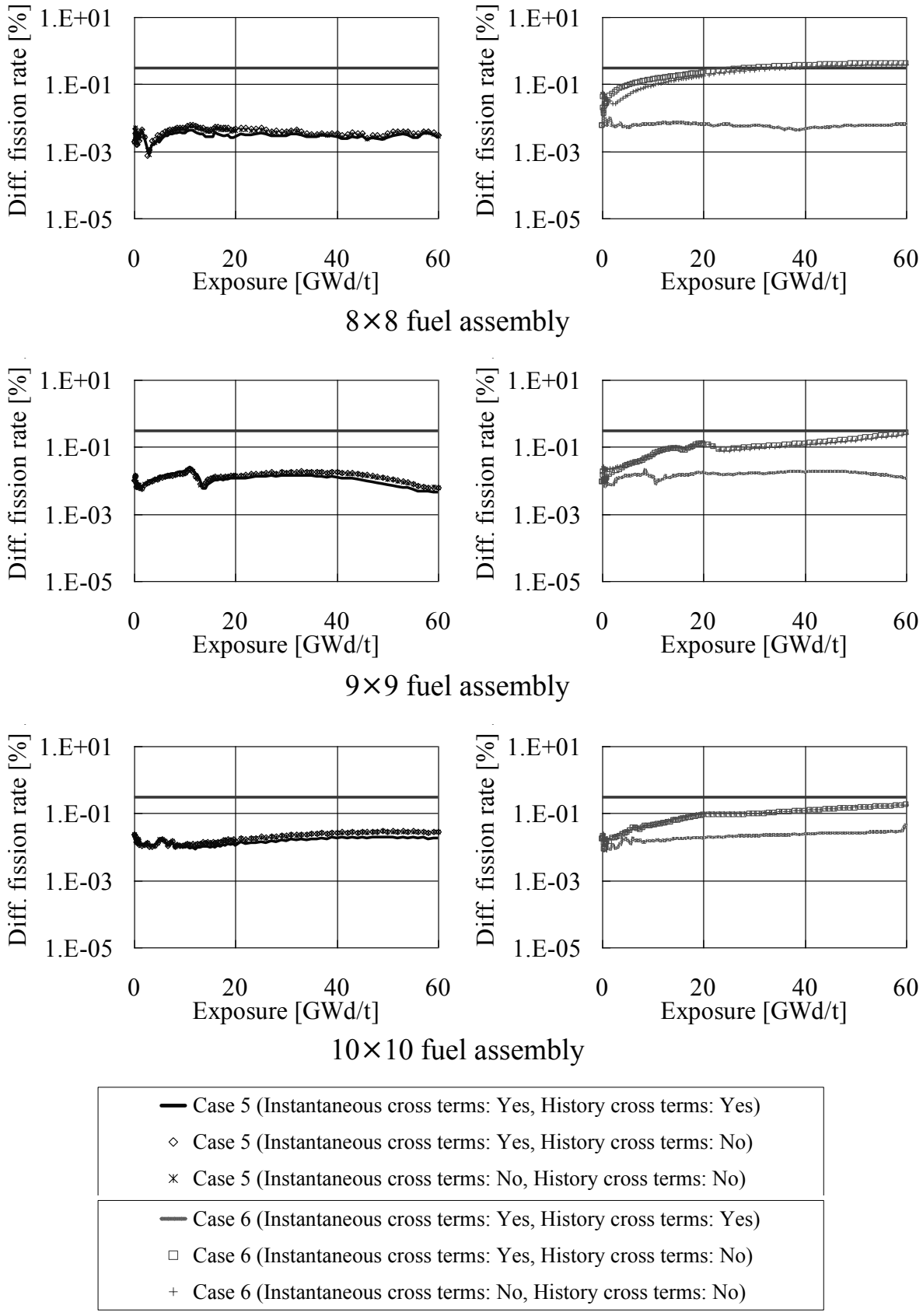

Figure 3.12 Calculation results of pin-by-pin fission rate distribution (Calculation cases: Table 3-8, Target accuracy line: 0.3%)

From Figures 3.11 and 3.12, in the benchmark calculation cases of No. 5 and No. 6, the calculation results obtained by the tabulated cross sections also achieve the target accuracies for the differences of k-infinity and pin-by-pin fission rate distribution. The differences of k-infinity and pin-by-pin fission rate distribution in Figures 3.11 and 3.12 are smaller than those in Figures 3.9 and 3.10. Unlike to the differences of k-infinity and pin-by-pin fission rate distribution of the benchmark calculation cases of No. 3 and No. 4 shown in Figures 3.9 and 3.10, those of the benchmark calculation cases of No. 5 and No. 6 are fairly constant as the exposure becomes higher for the benchmark calculation cases except for the effect of Gd. Combined with the discussions in the previous section, the errors due to the polynomial interpolations for the void fraction and the void history have dominant effects on the calculation accuracies of the present macroscopic cross section model.

In the benchmark calculation case of No. 5, three types of the differences of k-infinity and pin-by-pin fission rate distribution are shown within 0.01%dk/k and 0.01%, respectively (*i.e.*, three types of calculation results are almost the same). On the other hand, in the benchmark calculation case of No. 6, the calculation results obtained by the tabulated cross sections without cross terms for history effect and those without all cross terms become larger than those obtained by the tabulated cross sections with all cross terms. From these comparisons, the cross term effect among the fuel temperature, the moderator temperature, and their histories is small. Furthermore, the cross term effects among the control rod insertion, the control rod history, and other core state and depletion history variables (*i.e.*, the fuel temperature, the moderator temperature, and their histories) are extremely large, which shows the same tendencies as described in the previous section.

Similar to the previous section, the benchmark calculation case of No. 6 is also calculated out in several cross term conditions in order to evaluate and discuss the necessity of the treatment of cross term effect. The evaluation results are shown in **Table 3-9**. The values are calculated in a similar manner to those in Table 3-7. Note that the cross term effect among the fuel temperature, the control rod insertion, and their histories are omitted in Table 3-9 since they are already discussed in the previous section.

Table 3-9 Impact of cross term effect among fuel temperature, moderator temperature, control rod insertion, and their histories (1/3)

8×8 fuel assembly

	Exposure	Instantaneous cross terms		History cross terms	
	[GWd/t]	TFU-TMO	TMO-CR	HTFU-HTMO	HTMO-HCR
Δk_{inf} [%dk/k]	0	0.00	0.03	0.00	0.00
	10	0.00	-0.04	0.00	0.12
	20	0.00	-0.04	-0.01	0.18
	30	0.00	-0.04	-0.01	0.22
	40	0.00	-0.04	-0.01	0.24
	50	0.00	-0.04	-0.01	0.25
	60	0.00	-0.04	-0.01	0.25
$\Delta R_{f,RMS}$ [%]	0	0.00	0.05	0.00	0.00
	10	0.00	-0.04	0.00	0.08
	20	0.00	-0.03	0.00	0.13
	30	0.00	-0.03	0.00	0.17
	40	0.00	-0.03	0.00	0.20
	50	0.00	-0.03	0.00	0.22
	60	0.00	-0.03	0.00	0.23

Table 3-9 Impact of cross term effect among fuel temperature, moderator temperature, control rod insertion, and their histories (2/3)

9×9 fuel assembly

	Exposure	Instantaneous cross terms		History cross terms	
	[GWd/t]	TFU-TMO	TMO-CR	HTFU-HTMO	HTMO-HCR
Δk_{inf} [%dk/k]	0	0.00	0.04	0.00	0.00
	10	0.00	0.03	0.00	0.01
	20	0.00	-0.02	0.00	-0.01
	30	0.00	-0.04	0.00	0.08
	40	0.00	-0.04	-0.01	0.13
	50	0.00	-0.04	-0.01	0.19
	60	0.00	-0.03	-0.01	0.24
$\Delta R_{f,RMS}$ [%]	0	0.00	0.01	0.00	0.00
	10	0.00	0.01	0.00	0.03
	20	0.00	0.01	0.00	0.08
	30	0.00	-0.01	0.00	0.05
	40	0.00	-0.01	0.00	0.07
	50	0.00	-0.01	0.00	0.10
	60	0.00	-0.01	0.00	0.14

Table 3-9 Impact of cross term effect among fuel temperature, moderator temperature, control rod insertion, and their histories (3/3)

10×10 fuel assembly

	Exposure	Instantaneous cross terms		History cross terms	
	[GWd/t]	TFU-TMO	TMO-CR	HTFU-HTMO	HTMO-HCR
Δk_{inf} [%dk/k]	0	0.00	0.03	0.00	0.00
	10	0.00	0.03	0.00	0.00
	20	0.00	0.03	0.00	0.00
	30	0.00	-0.03	0.00	0.00
	40	0.00	-0.03	-0.01	0.04
	50	0.00	-0.03	-0.01	0.06
	60	0.00	-0.03	-0.01	0.09
$\Delta R_{f,RMS}$ [%]	0	0.00	0.00	0.00	0.00
	10	0.00	0.00	0.00	0.02
	20	0.00	0.01	0.00	0.05
	30	0.00	0.01	0.00	0.05
	40	0.00	0.01	0.00	0.06
	50	0.00	0.01	0.00	0.08
	60	0.00	0.01	0.00	0.09

From Table 3-9, the impacts of the cross term effect among the fuel temperature and the moderator temperature represented as “TFU-TMO” and that among the fuel temperature and the moderator temperature histories represented as “HTFU-HTMO” are small or almost zero for all types of fuel assemblies. Thus, similar to that among the void fraction and the fuel temperature and that among the fuel temperature and the control rod insertion in Table 3-7, such cross term effect could be negligible in the present macroscopic cross section model. The cross term effect among the moderator temperature and the control rod histories represented as “HTMO-HCR” has a large impact and this impact becomes larger as the exposure becomes higher for all types of fuel assemblies. The impact of this cross term effect is larger than that of the cross term effect among the fuel temperature and the control rod histories in Table 3-7. Even if the cross term effect among the moderator temperature and the control rod insertion represented as “TMO-CR” is neglected in the present macroscopic cross section model, the calculation results would achieve the target accuracies. However, the impact of the cross term effect among the moderator temperature and the control rod insertion for the k-infinity is about a third part of the target accuracy. Therefore, it is desirable to include the cross term effect among the moderator temperature and the control rod insertion in the present macroscopic cross section model.

Combined with the discussions in the previous section, the impacts of the cross term effect among the control rod history (or the void history) and other depletion history variables are generally large and the consideration of such cross term effect is crucial. The following cross term effects are necessary to consider in the present macroscopic cross section model as the following priority order:

(1) Void and control rod histories (HVOI-HCR).

(2) Void fraction and control rod insertion (VOI-CR).

(3) Moderator temperature and control rod histories (HTMO-HCR).

(4) Fuel temperature and control rod histories (HTFU-HCR).

(5) Void and fuel temperature histories (HVOI-HTFU).

(6) Moderator and control rod insertion (TMO-CR).

The treatment of them is important in order to accurately reproduce the target cross sections and estimate the k-infinity and the pin-by-pin fission rate distribution.

3.4. Conclusions

In this Chapter, I have developed a macroscopic cross section model for BWR pin-by-pin core analysis, in which the macroscopic cross sections are basically approximated by a linear combination of the macroscopic cross section on the base condition and the correction terms for the instantaneous and the history effects.

For the instantaneous effect, in order to capture the cross term effect among the core state sariables, several branch calculations, in which some core state variables are simultaneously changed from those on the base condition, are carried out and are used to calculate the variations of cross sections. For the history effect, the unified approach using the SH, which has been successfully used in the conventional advanced nodal method and the pin-by-pin core calculation for PWR, would be difficult to use since there is the large variation of the neutron spectrum due to the void fraction distribution and the control rod insertion within BWR fuel assemblies. Therefore, I use the exposure-averaged core state variables as the history indices. In order to capture the cross term effect among the depletion history variables, several depletion calculations, in which some depletion history variables are simultaneously changed from those on the base condition, are carried out and are used to calculate the variations of cross sections in combination with several branch calculations prepared for the instantaneous effect.

Verification calculations are carried out for typical BWR fuel assemblies. The pin-by-pin fine mesh calculations are carried out by the SUBARU code, which is a pin-by-pin core analysis code for BWR. Calculation results obtained by the reference and the tabulated cross sections are compared. The reference cross sections are obtained by the lattice physics calculations, in which core state variables are directly specified. The tabulated cross sections are reconstructed through the present macroscopic cross section model. In order to verify the present macroscopic cross section model, several benchmark calculations are carried out from the viewpoints of the treatment of exposure and the cross term effect for the instantaneous and the history effects.

Firstly, in order to confirm the calculation accuracies for the treatment of exposure in the present macroscopic depletion model, several benchmark calculations, in which the polynomial interpolations for the core state and the depletion history variables do not influence on calculation accuracies, are carried out. From the calculation results, though the differences of k-infinity and pin-by-pin fission rate distribution have several peaks related to the depletions of Gd-bearing fuel pin-cells, the differences are

sufficiently small from the viewpoints of the target accuracies. Therefore, the interpolation for exposure using the CSI in the present macroscopic cross section model can well reproduce the target cross sections.

Then, in order to confirm the validity of the treatment of the instantaneous and the history effects, several benchmark calculations are carried out. The calculation results obtained by the tabulated cross sections, which are reproduced with or without the cross term effect among the core state and the depletion history variables, are compared. The calculation results obtained by the tabulated cross sections, which consider the cross term effect among the core state and the depletion history variables, achieve the target accuracies on the differences of k-infinity and pin-by-pin fission rate distribution. Therefore, the present macroscopic cross section model well reproduces the target cross sections. The impacts of some cross term effects (*e.g.*, the cross term effect among the void fraction and the fuel temperature) are small or almost zero; thus such cross term effects could be negligible in the present macroscopic cross section model. However, the cross term effects among the control rod history (or the void history) and other depletion history variables have large impacts, thus the consideration of such cross term effects is crucial in order to accurately reproduce the target cross sections and estimate the k-infinity and the pin-by-pin fission rate distribution.

Consequently, the present cross section model for BWR pin-by-pin core analysis can be a candidate in practical applications on normal operations.

References

[1] K. R. Rempe, K. S. Smith, "SIMULATE-3 Pin Power Reconstruction: Methodology and Benchmarking," *Nucl. Sci. Eng.*, **10**, pp. 334-342, (1989).

[2] T. Iwamoto, M. Yamamoto, "Pin Power Reconstruction Methods of the Few-Group BWR Core Simulator NEREUS," *J. Nucl. Sci. Technol.*, **36**[12], pp. 1141-1152, (1999).

[3] T. Bahadir, S-Ö Lindahl, S. Palmtag, "SIMULATE-4 Multigroup Nodal Code with Microscopic Depletion Model," *Proc. Mathematics and Computation, Supercomputing, Reactor Physics and Nuclear and Biological Applications (M&C 2005)*, Sep. 12-15, 2005, Avignon, France, (2005). [CD-ROM].

[4] K. Yamaji, H. Matsumoto, M. Nakano, "Development of the New Pin-by-pin Core Calculation Method with Embedded Heterogeneous Assembly Calculation," *Proc. Int. Conf. on Physics of Reactors (PHYSOR 2006)*, Sep. 10-14, 2006, Vancouver, Canada, (2006). [CD-ROM].

[5] N. Z. Cho, S. Yuk, H. J. Yoo *et al*, "Overlapping Local/Global Iteration Framework for Whole-Core Transport Solution," *Proc. Int. Conf. on the Physics of Reactors (PHYSOR 2012*),Apr. 15-20, 2012, Knoxville, Tennessee, (2012). [CD-ROM].

[6] K. Tada, A. Yamamoto, Y. Yamane *et al.*, "Applicability of the Diffusion and Simplified P3 Theories for Pin-by-Pin Geometry of BWR," *J. Nucl. Sci. Technol.*, **45**[10], pp. 997-1008, (2008).

[7] K. Tada, A. Yamamoto, Y. Yamane, "Treatment of Staggered Mesh for BWR Pin-by-Pin Core Analysis," *J. Nucl. Sci. Technol.*, **46**[2], pp. 163-174, (2009).

[8] M. Tatsumi, A. Yamamoto, "Advanced PWR Core Calculation Based on Multi-group Nodal-transport Method in Three-dimensional Pin-by-Pin Geometry," *J. Nucl. Sci. Technol.*, **40**[6], pp. 376-387, (2003).

[9] F. Hoareau, M. Fiscounakis, D. Couyras *et al.*, "A Pin by Pin Microscopic Depletion Sheme Using an Homogeneous Core Calculation with Pin-Power Reconstruction," *Proc. 2009 Int. Congress on the Advances in Nuclear Power Plants (ICAPP '09)*, May 10-14, 2009, Tokyo, Japan, (2009). [CD-ROM].

[10] M. Stålek, C. Demazière, "Development and Validation of A Cross-Section Interface for PARCS," *Ann. Nucl. Energy*, **35**, pp. 2397-2409, (2008).

[11] T. Iwamoto, M. Yamamoto, "Advanced Nodal Methods of the Few-Group BWR Core Simulator

NEUREUS," *J. Nucl. Sci. Technol.*, **36**[11], pp. 996-1008, (1999).

[12] H. Yokota, *Suchikaisekinyumon I*, Kaisei Publishing Co., Ltd, Tokyo, pp. 77-82, (2003). [in Japanese].

[13] A. Karve, P. J. Turinsky, "FORMOSA-B: A Boling Water Reactor In-Core Management Optimization Package II," *Nucl. Technol.*, **131**, pp. 48-68, 1999.

[14] H. Okuno, Y. Naito, K. Suyama, *OECD/NEA Burnup Credit Criticality Benchmarks Phase IIIB: Burnup Calculations of BWR Fuel Assemblies for Storage and Transport*, JAERI-Research 2002-001, Japan Atomic Energy Research Institute (JAERI), (2002).

[15] A. Yamamoto, T. Ikehara, T. Ito *et al.*, "Benchmark Problem Suite for Reactor Physics Study of LWR Next Generation Fuels," *J. Nucl. Sci. Technol.*, **39**[8], pp. 900-912, (2002).

[16] *HELIOS Methods (Version 1.11)*, Studsvik Scandpower, 2009.

[17] A. Hébert, "A Consistent Technique for the Pin-by-Pin Homogenization of A Pressurized Water Reactor Assembly," *Nucl. Sci. Eng.*, **113**, pp. 227-238, (1991).

[18] A. Yamamoto, T. Ikeno, "Impact of Pin-by-Pin Thermal-Hydraulic Feedback Modeling on Steady-State Core Characteristics," *Nucl. Technol.*, **149**, pp.175-188, (2005).

[19] T. Ama, H. Hyoudou, T. Takeda, "Effect of Radial Void Distribution within Fuel Assembly on Assembly Neutronic Characteristics," *J. Nucl. Sci. Technol.*, **39**[1], pp. 90-100, (2002).

[20] K. Tada, A. Yamamoto, S. Kosaka *et al.*, "Development of a Prototype Pin-by-pin Fine Mesh Calculation Code for BWR Core Analysis," *Proc. Int. Conf. on Physics of Reactors (PHYSOR '08)*, Sep. 14-19, 2008, Interlaken, Switzerland, (2008). [CD-ROM].

Chapter 3 is based on an Accepted Manuscript of an article published by Taylor & Francis in Journal of Nuclear Science and Technology on Novenmber 29th, 2013, available online: http://wwww.tandfonline.com/10.1080/00223131.2014.864248.

Chapter 4. A spectral interference correction technique for coarse group cross sections on pin-by-pin core analysis (1): A new correction technique using leakage index

4.1. Introduction

Nuclear cross sections strongly depend on neutron energy (*e.g.*, their behaviors in resonance regions). In order to directly capture such energy dependence of cross sections and accurately calculate several types of reaction rates, several tens of thousand of energy groups should be used in core calculations. However, such ultra-fine group calculations are impractical for core analysis from the viewpoint of computational time and required memory. Therefore, in the conventional core analysis, the number of energy groups is reduced as the calculation geometry becomes large (*i.e.*, energy collapsing of cross sections is performed). However, the energy collapsing through conventional lattice physics calculations does not directly take into account the spectral interference effect, which is also called as the neighborhood effect or the spectral mismatch effect. Several corrections of cross sections considering the spectral interference effect are performed in core calculations in engineering or empirical manner. The spectral interference effect induces the variations of neutron spectrum and causes the spatial homogenization and the energy collapsing errors of cross sections.

In the conventional BWR core analysis with lattice physics and core calculations, assembly-homogenized coarse group (1 to 3 group(s)) cross sections are obtained by spatial average and energetic collapse of heterogeneous fine group (dozens to a few hundred groups) cross sections [1, 2]. These spatial homogenization and energy collapsing are performed through lattice physics calculations in single assembly geometries with the reflective boundary condition. Namely, neutron fluxes in single assembly geometries are used in the spatial homogenization and the energy collapsing of cross sections. However, neutron fluxes in single assembly geometries are generally different from those in core geometries, since the spatial and the energetic distribution of neutron fluxes become different in core geometries by the spectral interference effect due to the adjacent loadings of different types of fuel assemblies. As a result, appropriate cross sections for core calculations (*i.e.*, cross sections directly homogenized and collapsed in core geometries) are different from those calculated through lattice physics calculations in single assembly geometries. Therefore, a correction for cross sections

considering the spectral interference effect is necessary.

In order to correct the cross sections, several techniques have been studied. In the conventional core analysis in 2 or 3 groups, the spectral index (SI), which is the ratio of fast to thermal fluxes with the energy boundary on 0.625eV, has been traditionally used and the variations of cross sections are represented as the functions of SI [3, 4]. Moreover, in the recent studies, on-the-fly boundary condition adjustments have been investigated in pressurized water reactor (PWR) core geometries [5, 6]. In such on-the-fly correction techniques, cross sections are recalculated through the iterations of lattice physics calculations with the updated albedo boundary conditions, which are obtained by the boundary conditions of the target fuel assemblies in core calculations.

Recently, as a next generation core analysis method, the pin-by-pin fine mesh core calculation method for BWR core analysis has been studied [7, 8]. The previous study indicates that the pin-by-pin approach for BWR core analysis has good accuracy to evaluate important parameters for highly heterogeneous cores (*e.g.*, mixed-oxide (MOX) or high-burnup fuel loaded core). In BWR fuel assemblies, significant variation on energetic distribution of neutron spectrum is observed due to complicated geometries (*e.g.*, a large enrichment splitting, Gd-bearing rods, and control rod insertion). In order to capture significant variation on energetic distribution of neutron spectrum in BWR fuel assemblies or in highly heterogeneous cores and to obtain higher prediction accuracy, utilization of finer energy group structure in core calculations is desirable. For example, 8 or 9 group structure is used in the previous study of the pin-by-pin approach for light water reactor (LWR) core analysis [7-9]. However, even if I utilize such finer energy group structure, the spectral interference effect on the energy collapsing should be still taken into account and several correction techniques considering this effect are necessary. For such finer group calculations, in which variations on energetic distribution of neutron spectrum are considered in more detail, the conventional SI correction technique based on engineering or empirical approaches would not be valid since the SI only considers the ratio of fast to thermal fluxes. Namely, even if the SI indicates a same value, finer group cross sections would be different due to variations of fine group neutron spectrum within coarse groups. Furthermore, since various types of fuel assembly are loaded into BWR cores with complicated depletion histories (*e.g.*, void history and control rod history), the on-the-fly approaches would require larger computation time for the pin-by-pin BWR core analysis.

In this Chapter, I focus on the spectral interference effect on the energy collapsing and propose a new correction technique for the coarse group cross sections used in pin-by-pin core analysis of BWRs. Some theoretical descriptions related to this Chapter are described in section 4.2. The verifications of the present correction technique are shown in section 4.3 through numerical benchmark calculations. Finally, the concluding remarks are given in section 4.4.

4.2. Methodology

In this section, the root cause for the variations of coarse group cross sections in single and colorset assembly geometries (*i.e.*, lattice physics and core calculations) is discussed at first. Then, the theoretical descriptions for the new correction technique proposed in this Chapter are described.

4.2.1. Overview of energy collapsing

Firstly, I discuss the reason for the variations of coarse group cross sections in single and colorset assembly geometries from the viewpoint of mathematical formulations for the energy collapsing. In the conventional core analysis with lattice physics and core calculations, coarse group cross sections for core calculations are obtained by collapsing fine group cross sections with fine group neutron fluxes through lattice physics calculations in single assembly geometries:

$$\Sigma_{x,G} = \frac{\sum_{g \in G} \Sigma_{x,g} \phi_g}{\sum_{g \in G} \phi_g}, \tag{4.1}$$

where Σ and ϕ are the macroscopic cross section and the neutron flux, respectively. The subscripts of x, g, and G represent the reaction type (*i.e.*, absorption, fission, production cross sections, scattering matrices, and diffusion coefficients), the fine group index, and the coarse group index, respectively. By using Equation (4.1), the variation of coarse group cross sections obtained by single and colorset assembly calculations is written by:

$$
\begin{aligned}
&\Sigma_{x,G}^{colorset} - \Sigma_{x,G}^{single} \\
&= \frac{\sum_{g\in G} \Sigma_{x,g}^{single} \phi_g^{colorset}}{\sum_{g\in G} \phi_g^{colorset}} - \frac{\sum_{g\in G} \Sigma_{x,g}^{single} \phi_g^{single}}{\sum_{g\in G} \phi_g^{single}} \\
&= \sum_{g\in G} \Sigma_{x,g}^{single} \frac{\phi_g^{colorset}}{\sum_{g\in G} \phi_g^{colorset}} - \sum_{g\in G} \Sigma_{x,g}^{single} \frac{\phi_g^{single}}{\sum_{g\in G} \phi_g^{single}} \\
&= \sum_{g\in G} \Sigma_{x,g}^{single} \left(w_g^{colorset} - w_g^{single} \right),
\end{aligned}
\tag{4.2}
$$

where w is the neutron flux weight of particular energy group. The superscripts *single* and *colorset* represent single and colorset assembly calculations, respectively. Note that the fine group cross sections are assumed to be the same in single and colorset assembly calculations in Equation (4.2). According to Equation (4.2), the variations of fine group flux weights (*i.e.*, the energetic distribution of fine group neutron spectrum) are necessary to correct the coarse group cross sections due to the spectral interference effect.

From the viewpoint of actual physical phenomena, I consider that the variations of fine group neutron fluxes are caused by those of neutron leakage (*i.e.*, the boundary conditions of fuel assemblies). Then, the variations of fine group neutron fluxes cause those of coarse group cross sections. In order to capture such physical phenomena, several approaches have been studied (*e.g.*, neutron current to flux ratios on mesh surfaces is considered as a correction index, fine group neutron fluxes are reconstructed, or several colorset conditions are combined [10-12]). In this Chapter, I consider that the variations of coarse group cross sections are functions of neutron leakage and propose a new correction technique for coarse group cross sections considering the spectral interference effect by focusing on the variations of neutron leakage.

4.2.2. Correction technique using leakage index

In order to discuss the variations of coarse group cross sections through neutron leakage, I utilize the generalized perturbation theory based on the diffusion theory and derive the relationship between the variations of coarse group cross sections and neutron leakage [13]. It should be noted that I treat the spectral interference effect as perturbations of boundary condition on fuel assembly in focus. Thus, the following theoretical descriptions assume single assembly geometries with variations of boundary

condition.

Firstly, let us start with the k-effective eigenvalue equation based on diffusion theory:

$$(\mathbf{L}+\mathbf{A})\phi(\vec{r},E)=\frac{1}{k_{eff}}\mathbf{F}\phi(\vec{r},E), \tag{4.3}$$

where k_{eff} and ϕ are the k-effective (the effective multiplication factor) and the neutron flux, respectively. The operators **L**, **A**, and **F** correspond to the neutron leakage, the neutron loss by absorption and scattering reactions and the production by scattering reaction, and the production by fission reaction, respectively. From here, I consider the multi-group diffusion equation. The operators **L**, **A**, and **F** in Equation (4.3) are written as:

$$\begin{cases}\mathbf{L}=-\nabla D_g(\vec{r})\nabla \\ \mathbf{A}=\Sigma_{r,g}(\vec{r})-\sum_{g'\neq g}\Sigma_{s,g'\to g}(\vec{r}), \\ \mathbf{F}=\chi_g(\vec{r})\sum_{g'}\nu\Sigma_{f,g'}(\vec{r})\end{cases} \tag{4.4}$$

where D, Σ_r, $\nu\Sigma_f$, Σ_s, and χ are the diffusion coefficient, the removal cross section, the production cross section, the scattering cross section, and the fission spectrum, respectively. The vector of $\vec{r}$ indicates the space. The subscript of g represents the energy group index. By using the operator **M**, which is the diffusion operator, Equation (4.3) is written as:

$$\mathbf{M}\phi_g(\vec{r})=\left(\mathbf{L}+\mathbf{A}-\frac{1}{k_{eff}}\mathbf{F}\right)\phi_g(\vec{r})=0. \tag{4.5}$$

Now, let us consider an arbitrary reaction rate ratio:

$$R=\frac{\left\langle\Sigma_{1,g}(\vec{r}),\phi_g(\vec{r})\right\rangle}{\left\langle\Sigma_{2,g}(\vec{r}),\phi_g(\vec{r})\right\rangle}, \tag{4.6}$$

where R, Σ, ϕ, are the reaction rate ratio, the cross section, and the neutron flux, respectively. The bracket denotes the integration over space and the summation over neutron energy groups. In order to discuss coarse group cross sections in Equation (4.1), $\Sigma_{1,g}(\vec{r})$ and $\Sigma_{2,g}(\vec{r})$ in Equation (4.6) are determined as:

$$\begin{cases} \Sigma_{1,g}(\vec{r}) = \Sigma_{x,g}(\vec{r}) C_{m,g,G}(\vec{r}) \\ \Sigma_{2,g}(\vec{r}) = C_{m,g,G}(\vec{r}) \end{cases}, \tag{4.7}$$

where Σ_x is the macroscopic cross sections of reaction x. The subscript of g, G, and m represent the fine energy group, the coarse energy group, and the homogenized mesh indices, respectively. In Equation (4.7), $C_{m,g,G}(\vec{r})$ is defined as:

$$C_{m,g,G}(\vec{r}) \equiv \begin{cases} 1, & if \ \ \vec{r} \in V_m, g \in G \\ 0, & otherwise \end{cases} \tag{4.8}$$

where V_m is the volume space of homogenized mesh m. By substituting Equations (4.7) and (4.8) into Equation (4.6), coarse group cross sections in Equation (4.1) are represented as:

$$\Sigma_{x,m,G} = \frac{\left\langle \Sigma_{x,g}(\vec{r}) C_{m,g,G}(\vec{r}), \phi_g(\vec{r}) \right\rangle}{\left\langle C_{m,g,G}(\vec{r}), \phi_g(\vec{r}) \right\rangle}. \tag{4.9}$$

The sensitivity coefficient of coarse group cross sections for an arbitrary parameter is defined as:

$$S \equiv \frac{d\Sigma_{x,m,G}}{\Sigma_{x,m,G}} \Big/ \frac{dX}{X}, \tag{4.10}$$

where S and X are the sensitivity coefficient and the arbitrary parameter, respectively. With common

derivation in the generalized perturbation theory [13], Equation (4.10) is written as follows by neglecting the second order variations:

$$S = \left(\frac{\left\langle \frac{\partial \Sigma_{x,g}(\vec{r})}{\partial X} C_{m,g,G}(\vec{r}), \phi_g(\vec{r}) \right\rangle}{\left\langle \Sigma_{x,g}(\vec{r}) C_{m,g,G}(\vec{r}), \phi_g(\vec{r}) \right\rangle} + \frac{\left\langle \Sigma_{x,g}(\vec{r}) C_{m,g,G}(\vec{r}), \frac{\partial \phi_g(\vec{r})}{\partial X} \right\rangle}{\left\langle \Sigma_{x,g}(\vec{r}) C_{m,g,G}(\vec{r}), \phi_g(\vec{r}) \right\rangle} - \frac{\left\langle C_{m,g,G}(\vec{r}), \frac{\partial \phi_g(\vec{r})}{\partial X} \right\rangle}{\left\langle C_{m,g,G}(\vec{r}), \phi_g(\vec{r}) \right\rangle} \right) X . \quad (4.11)$$

The first term in the right hand side of Equation (4.11) is the direct term, which expresses the variation of reaction rate due to the perturbation of $\Sigma_{x,g}(\vec{r})$. The second and third terms are the indirect terms, which express the variation of reaction rate due to the perturbation of neutron flux.

Then, in order to estimate the indirect terms (*i.e.*, the second and the third terms in the right hand side of Equation (4.11)), I introduce the generalized adjoint flux, which is calculated by the adjoint equation described as:

$$\mathbf{M}^{+}\Gamma_g^{+}(\vec{r}) = Q_g^{+}(\vec{r}), \quad (4.12)$$

where Γ^{+} and Q^{+} are the generalized adjoint flux and the generalized adjoint source, respectively. For the reaction rate ratio shown in Equation (4.6), the generalized adjoint source is given as:

$$Q_g^{+}(\vec{r}) = \frac{\Sigma_{1,g}(\vec{r})}{\left\langle \Sigma_{1,g}(\vec{r}), \phi_g(\vec{r}) \right\rangle} - \frac{\Sigma_{2,g}(\vec{r})}{\left\langle \Sigma_{2,g}(\vec{r}), \phi_g(\vec{r}) \right\rangle} . \quad (4.13)$$

For energy collapsing of cross sections shown in Equation (4.9), by using Equation (4.7), Equation (4.13) is written as:

$$Q_g^+(\vec{r}) = \frac{\Sigma_{x,g}(\vec{r})C_{m,g,G}(\vec{r})}{\left\langle \Sigma_{x,g}(\vec{r})C_{m,g,G}(\vec{r}), \phi_g(\vec{r}) \right\rangle} - \frac{C_{m,g,G}(\vec{r})}{\left\langle C_{m,g,G}(\vec{r}), \phi_g(\vec{r}) \right\rangle}. \tag{4.14}$$

Thus, from Equation (4.12), the generalized adjoint flux for energy collapsing of cross sections satisfies:

$$\mathbf{M}^+\Gamma_g^+(\vec{r}) = \frac{\Sigma_{x,g}(\vec{r})C_{m,g,G}(\vec{r})}{\left\langle \Sigma_{x,g}(\vec{r})C_{m,g,G}(\vec{r}), \phi_g(\vec{r}) \right\rangle} - \frac{C_{m,g,G}(\vec{r})}{\left\langle C_{m,g,G}(\vec{r}), \phi_g(\vec{r}) \right\rangle}. \tag{4.15}$$

By multiplying $\frac{\partial \phi_g(\vec{r})}{\partial X}$ for the both sides of Equation (4.15), integrating over space, and summing over neutron energy groups, I can obtain:

$$\left\langle \frac{\partial \phi_g(\vec{r})}{\partial X}, \mathbf{M}^+\Gamma^+ \right\rangle = \frac{\left\langle \Sigma_{x,g}(\vec{r})C_{m,g,G}(\vec{r}), \frac{\partial \phi_g(\vec{r})}{\partial X} \right\rangle}{\left\langle \Sigma_{x,g}(\vec{r})C_{m,g,G}(\vec{r}), \phi_g(\vec{r}) \right\rangle} - \frac{\left\langle C_{m,g,G}(\vec{r}), \frac{\partial \phi_g(\vec{r})}{\partial X} \right\rangle}{\left\langle C_{m,g,G}(\vec{r}), \phi_g(\vec{r}) \right\rangle}. \tag{4.16}$$

In Equation (4.5), if I consider the variation of operator **M** and the neutron flux, they satisfy the following relation:

$$\left(\mathbf{M} + d\mathbf{M}\right)\left(\phi_g(\vec{r}) + d\phi_g(\vec{r})\right) = 0. \tag{4.17}$$

Here, I also assume that the second order variations are negligible and consider $\mathbf{M}\phi_g(\vec{r}) = 0$, then I obtain:

$$\mathbf{M}d\phi_g(\vec{r}) = -d\mathbf{M}\phi_g(\vec{r}). \tag{4.18}$$

Thus, by multiplying $\Gamma_g^+(\vec{r})$, integrating over space, summing over neutron energy groups, and dividing dX for the both sides of Equation (4.18), I can obtain:

$$\left\langle \Gamma_g^+(\vec{r}), \mathbf{M}\frac{\partial \phi_g(\vec{r})}{\partial X} \right\rangle = -\left\langle \Gamma_g^+(\vec{r}), \frac{\partial \mathbf{M}}{\partial X}\phi_g(\vec{r}) \right\rangle. \tag{4.19}$$

By using the property of adjoint operator for the left hand side of Equation (4.19), I can obtain:

$$\left\langle \Gamma_g^+(\vec{r}), \mathbf{M}\frac{\partial \phi_g(\vec{r})}{\partial X} \right\rangle = \left\langle \frac{\partial \phi_g(\vec{r})}{\partial X}, \mathbf{M}^+\Gamma_g^+(\vec{r}) \right\rangle. \tag{4.20}$$

From Equations (4.19) and (4.20), Equation (4.16) is written as:

$$-\left\langle \Gamma_g^+(\vec{r}), \frac{\partial \mathbf{M}}{\partial X}\phi_g(\vec{r}) \right\rangle = \frac{\left\langle \Sigma_{x,g}(\vec{r})C_{m,g,G}(\vec{r}), \frac{\partial \phi_g(\vec{r})}{\partial X} \right\rangle}{\left\langle \Sigma_{x,g}(\vec{r})C_{m,g,G}(\vec{r}), \phi_g(\vec{r}) \right\rangle} - \frac{\left\langle C_{m,g,G}(\vec{r}), \frac{\partial \phi_g(\vec{r})}{\partial X} \right\rangle}{\left\langle C_{m,g,G}(\vec{r}), \phi_g(\vec{r}) \right\rangle}. \tag{4.21}$$

Therefore, by using Equation (4.21), the sensitivity coefficient of coarse group cross sections for an arbitrary parameter shown in Equation (4.11) is given by:

$$S = \left(\frac{\left\langle \frac{\partial \Sigma_{x,g}(\vec{r})}{\partial X} C_{m,g,G}(\vec{r}), \phi_g(\vec{r}) \right\rangle}{\left\langle \Sigma_{x,g}(\vec{r})C_{m,g,G}(\vec{r}), \phi_g(\vec{r}) \right\rangle} - \left\langle \Gamma_g^+(\vec{r}), \frac{\partial \mathbf{M}}{\partial X}\phi_g(\vec{r}) \right\rangle \right) X. \tag{4.22}$$

In this Chapter, I assume that the fine group cross sections $\Sigma_{x,g}(\vec{r})$ do not change when an arbitrary parameter *X* is perturbed. Thus, Equation (4.22) is approximated as:

$$S \approx -\left\langle \Gamma_g^+(\vec{r}), \frac{\partial \mathbf{M}}{\partial X}\phi_g(\vec{r}) \right\rangle X . \tag{4.23}$$

Finally, let us consider the variation of neutron leakage due to the spectral interference effect in Equation (4.23). In order to express the neutron leakage, I newly introduce a LI defined by:

$$LI_g(\vec{r}) \equiv \frac{\int_S \overrightarrow{J_g}(\vec{r}) \cdot \vec{n}(\vec{r}) dS \Big/ \int_V dV}{\phi_g(\vec{r})}, \tag{4.24}$$

which is an index parameter related to neutron leakage and is defined as a macroscopic cross section of volume-averaged neutron leakage. From the viewpoint of neutron balance in the k-effective eigenvalue calculation, the LI is calculated by:

$$LI_g(\vec{r}) = \frac{\int_V \frac{\chi_g(\vec{r})}{k_{eff}} \sum_{g'} \nu\Sigma_{f,g'}(\vec{r})\phi_{g'}(\vec{r}) + \sum_{g' \neq g} \Sigma_{s,g' \to g}(\vec{r})\phi_{g'}(\vec{r}) - \Sigma_{r,g}(\vec{r})\phi_g(\vec{r}) dV \Big/ \int_V dV}{\phi_g(\vec{r})}. \tag{4.25}$$

From Equation (4.25), the dimension of LI is same as macroscopic cross sections. That is, the LI is also considered as a kind of macroscopic cross section related to the neutron leakage.

By utilizing the LI calculated by Equation (4.25), the operator **L** is approximated as:

$$\mathbf{L} = -\nabla D_g(\vec{r})\nabla \approx LI_g(\vec{r}), \tag{4.26}$$

thus, the variation of operator **M** is written as:

$$\partial \mathbf{M} = \partial \mathbf{L} \approx \partial LI_g(\vec{r}) . \tag{4.27}$$

It should be noted that only $LI_g(\vec{r})$ is changed as shown in Equation (4.27) since I assume that the variations of neutron spectrum are only occurred by the neutron leakage due to the spectral interference effect (*i.e.*, cross sections are not changed). Therefore, by using Equations (4.26) and (4.27), Equation (4.23) is approximated as:

$$\begin{aligned} S &= \frac{\partial \Sigma_{x,m,G}}{\Sigma_{x,m,G}} \Bigg/ \frac{\partial LI_{g'}(\vec{r})}{LI_{g'}(\vec{r})} \\ &= -\left\langle \Gamma_g^+(\vec{r}), \frac{\partial \mathbf{M}}{\partial LI_{g'}(\vec{r})} \phi_g(\vec{r}) \right\rangle LI_{g'}(\vec{r}) \\ &\approx -\left\langle \Gamma_g^+(\vec{r}), C_m(\vec{r}) \delta_{g,g'} \phi_g(\vec{r}) \right\rangle LI_{g'}(\vec{r}), \end{aligned} \tag{4.28}$$

where $C_m(\vec{r})$ is defined as:

$$C_m(\vec{r}) \equiv \begin{cases} 1, & if \ \vec{r} \in V_m \\ 0, & otherwise \end{cases} \tag{4.29}$$

In Equation (4.28), δ is the kronecker delta. Note that, as shown in Equations (4.28) and (4.29), the sensitivity coefficient of coarse group cross sections is only represented by the LIs over the volume space of target homogenized mesh *m*. In reality, neutron leakage changes by various reasons (*e.g.*, variation of boundary condition and cross section change) and it has complicated spatial and energetic relationships. For example, cross section changes such as control rod insertion in another fuel assembly can vary neutron leakage at a pin-cell in focus through spatial and energetic coupling as a critical system. However, by introducing the LIs, which correspond to macroscopic "leakage" cross sections, the variations of neutron leakage due to the spectral interference effect can be considered as perturbation of LIs in the target homogenized mesh. This greatly simplifies the situation and is a great advantage of using the LIs. Therefore, Equation (4.28) is written as:

$$\frac{\partial \Sigma_{x,m,G}}{\partial LI_{g'}(\vec{r})} = -\Sigma_{x,m,G} \int_{\vec{r} \in V_m} \Gamma^{+}_{g'}(\vec{r}) \phi_{g'}(\vec{r}) d\vec{r} \,. \tag{4.30}$$

By considering the summation of variations of fine group LIs, the variations of coarse group cross sections can be estimated as:

$$\begin{aligned} d\Sigma_{x,m,G} &= \sum_{g'} \frac{\partial \Sigma_{x,m,G}}{\partial LI_{g'}(\vec{r})} dLI_{g'}(\vec{r}) \\ &= -\Sigma_{x,m,G} \sum_{g'} \left[\int_{\vec{r} \in V_m} \Gamma^{+}_{g'}(\vec{r}) \phi_{g'}(\vec{r}) dLI_{g'}(\vec{r}) d\vec{r} \right] \end{aligned} \tag{4.31}$$

In Equation (4.31), the variations of coarse group cross sections are estimated by integrating the product of fine group generalized adjoint flux, fine group neutron flux, and the variation of fine group LI over space and by summing it over neutron energy groups. However, since core calculations in the conventional core analysis are performed with coarse group cross sections, they cannot directly estimate the fine group generalized adjoint fluxes, the fine group neutron fluxes, and the variations of fine group LIs in the right hand side of Equation (4.31). Thus, it is necessary to simplify Equation (4.31) based on coarse group parameters.

In this Chapter, I assume the relationship between the variations of fine group and coarse group LIs as:

$$dLI_G(\vec{r}) \approx \frac{\sum_{g \in G} dLI_g(\vec{r}) \phi_g(\vec{r})}{\sum_{g \in G} \phi_g(\vec{r})}, \tag{4.32}$$

thus Equation (4.31) is written as:

$$
\begin{aligned}
d\Sigma_{x,m,G} &= -\Sigma_{x,m,G}\sum_{g'}\left[\int_{\vec{r}\in V_m}\Gamma^{+}_{g'}(\vec{r})\phi_{g'}(\vec{r})dLI_{g'}(\vec{r})d\vec{r}\right] \\
&= -\Sigma_{x,m,G}\int_{\vec{r}\in V_m}\left[\sum_{G'}\left\{\sum_{g'\in G'}\Gamma^{+}_{g'}(\vec{r})\phi_{g'}(\vec{r})dLI_{g'}(\vec{r})\right\}\right]d\vec{r} \\
&= -\Sigma_{x,m,G}\int_{\vec{r}\in V_m}\left[\sum_{G'}\left\{\frac{\sum_{g'\in G'}\Gamma^{+}_{g'}(\vec{r})\phi_{g'}(\vec{r})dLI_{g'}(\vec{r})\sum_{g'\in G'}\phi_{g'}(\vec{r})}{\sum_{g'\in G'}dLI_{g'}(\vec{r})\phi_{g'}(\vec{r})}\frac{\sum_{g'\in G'}dLI_{g'}(\vec{r})\phi_{g'}(\vec{r})}{\sum_{g'\in G'}\phi_{g'}(\vec{r})}\right\}\right]d\vec{r} \\
&\approx -\Sigma_{x,m,G}\int_{\vec{r}\in V_m}\left[\sum_{G'}\left\{\frac{\sum_{g'\in G'}\Gamma^{+}_{g'}(\vec{r})\phi_{g'}(\vec{r})dLI_{g'}(\vec{r})\sum_{g'\in G'}\phi_{g'}(\vec{r})}{\sum_{g'\in G'}dLI_{g'}(\vec{r})\phi_{g'}(\vec{r})}\right\}dLI_{G'}(\vec{r})\right]d\vec{r} \\
&= \int_{\vec{r}\in V_m}\left[\sum_{G'}a_{x,G,G'}(\vec{r})dLI_{G'}(\vec{r})\right]d\vec{r} \\
&= \sum_{G'}\left[\int_{\vec{r}\in V_m}a_{x,G,G'}(\vec{r})dLI_{G'}(\vec{r})d\vec{r}\right],
\end{aligned}
\tag{4.33}
$$

where

$$
a_{x,G,G'}(\vec{r}) = -\Sigma_{x,m,G}\frac{\sum_{g'\in G'}\Gamma^{+}_{g'}(\vec{r})\phi_{g'}(\vec{r})dLI_{g'}(\vec{r})\sum_{g'\in G'}\phi_{g'}(\vec{r})}{\sum_{g'\in G'}dLI_{g'}(\vec{r})\phi_{g'}(\vec{r})},
\tag{4.34}
$$

which is the coupling coefficient defined as a variation of G-th group cross sections per a variation of G'-th group LI (*i.e.*, $a_{x,G,G'}(\vec{r})$ corresponds to a sensitivity coefficient of coarse group cross sections to coarse group LIs).

In Equations (4.33) and (4.34), the fine group generalized adjoint fluxes and neutron fluxes are still necessary to calculate the coupling coefficients though the variations of coarse group cross sections are approximately estimated by the variations of coarse group LIs. Thus, in this Chapter, Equation (4.34) is not used to calculate the coupling coefficients since utilization of Equation (4.34) requires large computational load to calculate the fine group generalized adjoint fluxes. The details of calculation procedures to estimate the coupling coefficients are shown in the next section. The discussions from the viewpoint of computational load are described in the section 4.2.3

For the spatial differences of homogenized meshes, Equation (4.33) is written as:

$$d\Sigma_{x,m,G} = \Sigma_{x,m,G}^{colorset} - \Sigma_{x,m,G}^{single} \approx \sum_{G'} a_{x,m,G,G'} dLI_{m,G'} = \sum_{G'} a_{x,m,G,G'} \left(LI_{m,G'}^{colorset} - LI_{m,G'}^{single} \right), \quad (4.35)$$

where the superscript *single* and *colorset* represent single and colorset assembly calculations, respectively. In this Chapter, Equation (4.35) is used for all reaction types of cross sections (*i.e.*, absorption, fission, production cross sections, scattering matrices, and diffusion coefficients) since they are collapsed with neutron fluxes as Equation (4.1). The applicability of Equation (4.35), which is derived from Equation (4.31), is verified through numerical calculations in section 4.3.

4.2.3. Calculation procedure to estimate coupling coefficients of leakage index

In the previous section, I utilize the generalized perturbation theory and approximately derive the relationship between the variations of coarse group cross sections and LIs as shown in Equation (4.35). According to Equation (4.35), the coupling coefficients are necessary to estimate the variations of coarse group cross sections in prior to core calculations. However, the fine group generalized adjoint fluxes and neutron fluxes are necessary to directly calculate the coupling coefficients based on Equation (4.34) and such calculation is impractical from the viewpoint of computational load. Therefore, in this Chapter, I perform several colorset assembly calculations to obtain the relationship between the variations of coarse group cross sections and LIs. Then I calculate the coupling coefficients by the least squares approximation for the variations of coarse group cross sections and LIs. By adopting such colorset assembly calculations, calculations of fine group generalized adjoint fluxes and neutron fluxes are not necessary. In this section, the details of calculation procedures to estimate the coupling coefficients are described.

Equation (4.35) is derived under the assumption that the spectral interference effect is treated as the perturbations of boundary condition on target fuel assemblies. In order to calculate the coupling coefficients, it is necessary to simulate the perturbations of boundary conditions due to the spectral interference effect. In this Chapter, I carry out several colorset assembly calculations to perturb the boundary conditions on the target fuel assemblies. However, we generally do not have prior knowledge which types of fuel assemblies (e.g., the assembly exposure and the enrichment distribution) will be loaded into the adjacent regions of target fuel assembly. Therefore, I perform various simplified colorset assembly calculations and calculate the coupling coefficients. For various simplified colorset assembly

calculations, I prepare some simplified fuel assemblies.

In this section, the calculation procedure to calculate the coupling coefficients of LIs in Equation (4.35) is described as first, then the details of target and simplified fuel assemblies are shown.

The overview of the calculation procedure to obtain the relationship between the variations of coarse group cross sections and those of LIs and to calculate the coupling coefficients in Equation (4.35) is shown in **Figure 4.1**.

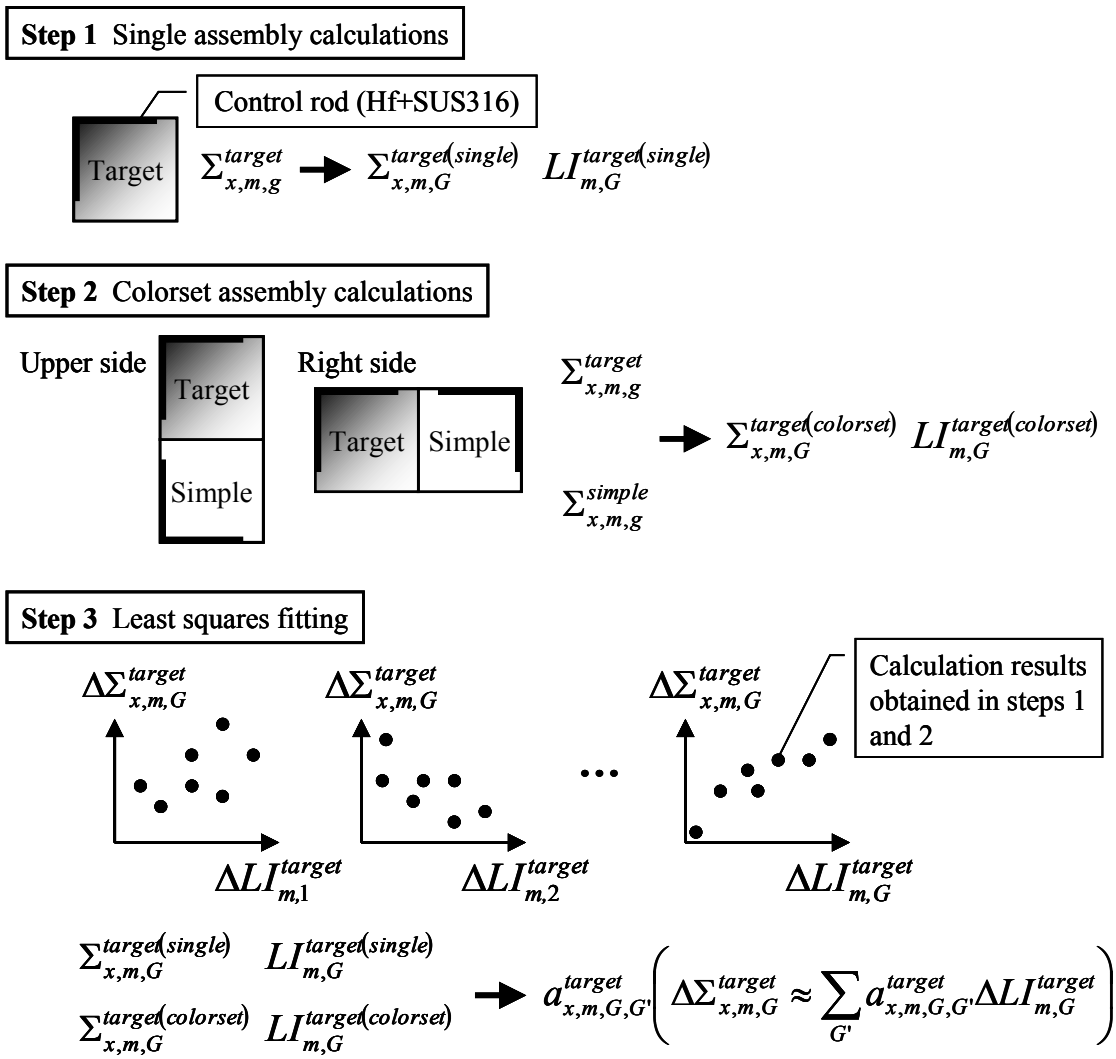

Figure 4.1 Overview of procedure to obtain relationship between coarse group cross sections and LIs

As shown in Figure 4.1, firstly, fine group calculations are carried out in single assembly geometries, which consist of the target fuel assembly. Coarse group cross sections ($\Sigma_{m,G}^{target(single)}$) are collapsed in single assembly geometries and coarse group LIs ($LI_{m,G}^{target(single)}$) are estimated by utilizing

the calculation results (*i.e.*, the neutron fluxes and the k-effective).

Secondly, fine group calculations are carried out in colorset assembly geometries, which consist of the target and the simplified fuel assemblies. Coarse group cross sections ($\Sigma_{m,G}^{target(colorset)}$) are directly collapsed in colorset assembly geometries and coarse group LIs ($LI_{m,G}^{target(colorset)}$) are estimated by utilizing the calculation results (i.e., the neutron fluxes and the k-effective). Note that the fine group cross sections ($\Sigma_{x,m,g}^{target}$ and $\Sigma_{x,m,g}^{simple}$) used in the steps 1 and 2 are the same and they are preliminarily calculated in lattice physics code. The details of preparation of fine group cross sections are described in the section 4.3.1.

In the colorset assembly calculations, the colorset assembly geometries should be chosen to cover actual impacts of spectral interference effect. In this Chapter, I assume that actual impacts of spectral interference effect can be simulated two assembly geometries with reflective boundary condition, in which the target and the simplified fuel assemblies are adjacently loaded. This assumption is justified since the spectral interference effect is mainly observed in the assembly peripheral meshes and the actual impacts of spectral interference effect can be decomposed into the impact from each assembly surface. Thus, by considering the symmetry of fuel assembly, two types of two assembly geometries shown in Figure 4.1 are used in this Chapter. It should be noted that the control rod insertion for two assembly geometries shown in Figure 4.1 is different from that for actual operating core (*i.e.*, the control rods are not inserted into neighboring control cells). However, in lattice physics calculations (single assembly geometries with the reflective boundary condition), the control rods are assumed to be inserted into neighboring control cells. Moreover, if the control rod insertion for actual operating core is simulated, colorset assembly geometries become large and large computational load is necessary. Thus, in order to simplify colorset assembly geometries and to reduce computational load, I use the two assembly geometries with approximate treatment of the control rod insertion.

Finally, the coupling coefficients of LIs ($a_{m,G,G'}^{target}$), which correspond to $a_{x,m,G,G'}$ in Equation (4.35), are calculated for each pin-cell. The least squares approximation for the relationship between coarse group cross sections and LIs obtained in the steps 1 and 2 is used to estimate the coupling coefficients.

In this Chapter, three types of 8×8 BWR fuel assemblies shown in **Figure 4.2** are used for the target fuel assemblies.

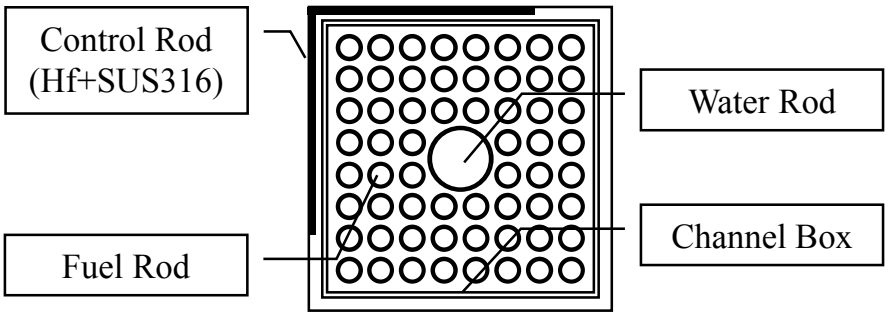

4	3	3	1	1	3	3	4
3	3	1	2	2	1	3	3
3	1	2	1	1	2	1	3
1	2	1			1	2	1
1	2	1			1	2	1
3	1	2	1	1	2	1	3
3	3	1	2	2	1	3	3
4	3	3	1	1	3	3	4

Low-enrichment UO_2 fuel assembly
(Assembly-averaged enrichment: 1.0wt% ^{235}U)

Type-1 1.2wt% ^{235}U
Type-2 1.0wt% ^{235}U
Type-3 0.8wt% ^{235}U
Type-4 0.7wt% ^{235}U

4	3	2	2	2	2	3	4
3	2	G	1	1	G	2	3
2	G	1	1	1	1	G	2
2	1	1			1	1	2
2	1	1			1	1	2
2	G	1	1	1	1	G	2
3	2	G	1	1	G	2	3
4	3	2	2	2	2	3	4

High-enrichment UO_2 fuel assembly
(Assembly-averaged enrichment: 3.5wt% ^{235}U)

Type-1 4.2wt% ^{235}U
Type-2 3.3wt% ^{235}U
Type-3 2.8wt% ^{235}U
Type-4 2.3wt% ^{235}U
Type-G 3.0wt% ^{235}U, 6.0wt% Gd

4	3	2	2	2	2	3	4
3	G	1	1	G	1	G	3
2	1	1	G	1	1	1	2
2	1	G			1	G	2
2	G	1			G	1	2
2	1	1	1	G	1	1	2
3	G	1	G	1	1	G	3
4	3	2	2	2	2	3	4

MOX fuel assembly
(Assembly-averaged enrichment: 4.0wt% Pu-fissile)

Type-1 4.8wt% Pu-fissile
Type-2 3.9wt% Pu-fissile
Type-3 3.2wt% Pu-fissile
Type-4 1.9wt% Pu-fissile
Type-G 2.0wt% ^{235}U, 3.0wt% Gd

Figure 4.2 8×8 BWR fuel assemblies used in Chapter 4

As shown in Figure 4.2, the low-enrichment UO_2 (assembly-averaged enrichment: 1.0wt% ^{235}U), the high-enrichment UO_2 (assembly-averaged enrichment: 3.5wt% ^{235}U), and the MOX (assembly-averaged enrichment: 4.0wt% Pu-fissile) fuel assemblies are used. The geometry of these 8×8 fuel assembly are taken by the reference [14]. The fuel rod enrichment distributions of them are manually decided.

In general, the enrichment distribution of fuel assemblies, which will be loaded into the adjacent regions of target fuel assembly, is unknown in prior to core calculations. Thus, six types of fuel

assemblies with the uniform enrichment distribution are used for simplified fuel assemblies. The fuel rod enrichments are 1.0 wt% ^{235}U, 3.0 wt% ^{235}U, 5.0 wt% ^{235}U, 3.0 wt% Pu-fissile, 4.0 wt% Pu-fissile, and 5.0 wt% Pu-fissile. Enrichments of ^{235}U and Pu-fissile are chosen to cover the values used in typical BWR fuel assemblies. The geometry of simplified fuel assemblies is the same with that of target fuel assemblies (*i.e.*, the simplified fuel assemblies are also 8×8 BWR fuel assemblies).

4.3. Numerical calculations

4.3.1. Calculation conditions

4.3.1.1. Preparation of pin-cell averaged cross sections

The pin-cell averaged cross sections used in this Chapter are calculated by the HELIOS code in 47 energy groups [15]. In the HELIOS code, the depletion calculation is performed in single assembly geometry with the reflective boundary condition. The void fraction, the control rod position, and the power density are fixed during the depletion calculation. Through the depletion calculations, I obtain the pin-cell averaged fine group cross sections at 0, 15, 30, 45, and 60GWd/t (assembly-averaged exposure). The fine group cross sections at 0, 15, 30, 45, and 60GWd/t are used to construct the two assembly geometries shown in the section 4.2.3 and the 4×4 colorset assembly geometries as described below.

In order to reduce the spatial homogenization errors, the superhomogenization (SPH) method is applied for 47-group pin-cell averaged cross sections in single assembly geometries [16]. Note that the SPH method is not applied to reduce the energy collapsing errors in this Chapter.

In general, the SPH factor changes due to the spectral interference effect similar to the coarse group cross sections. In order to apply the SPH method to reduce the energy collapsing errors, consideration of the spectral interference effect on SPH factor is necessary. However, the treatment of the SPH factor considering the spectral interference effect is out of the scope of this Chapter. I focus on the reproduction of reference coarse group cross sections, which are directly obtained by colorset assembly calculations, in this Chapter. Treatment of the SPH factor will be addressed in a future study.

4.3.1.2. Estimations of coupling coefficients of leakage index

In the present correction technique using the leakage index, the two assembly geometries, which consist of the target and the simplified fuel assemblies, are used. Through the two assembly calculations,

the perturbations of boundary conditions due to the spectral interference effect are simulated and the coupling coefficients of LIs are calculated.

In this Chapter, I carry out 36 patterns of two assembly calculations for one target fuel assemblies. These 36 patterns of two assembly geometries are determined by the combinations of calculation conditions for simplified fuel assemblies as follows:

- Fuel rod enrichment (six patterns): 1.0 wt% ^{235}U, 3.0 wt% ^{235}U, 5.0 wt% ^{235}U, 3.0 wt% Pu-fissile, 4.0 wt% Pu-fissile, and 5.0 wt% Pu-fissile.
- Assembly-averaged exposure (three patterns): 0, 30, and 60GWd/t.
- Loading position of simplified fuel assemblies (two patterns): Upper and right sides for the target fuel assembly.

Let us compare the computational load to calculate the coupling coefficients of LIs in Equation (4.35). I can use two approaches to calculate the coupling coefficients (*i.e.*, by using the fine group generalized adjoint fluxes and neutron fluxes based on Equation (4.34), or by applying the least squares approximation for the calculation results obtained by the two assembly calculations).

In order to calculate the fine group generalized adjoint fluxes using Equation (4.13), different generalized adjoint sources should be set for each pin-cell meshes, reaction types, and coarse energy groups. When I calculate the fine group generalized adjoint fluxes for absorption, fission, production cross sections, scattering matrices, and diffusion coefficients with 8 groups in 8×8 BWR fuel assembly, approximately 5,000 single assembly calculations are necessary. Note that the number of pin-cell meshes of 8×8 BWR fuel assembly is 55 by considering the symmetry of 8×8 BWR fuel assembly. In general, in order to calculate the generalized adjoint fluxes, complicated iteration calculations are necessary. Thus, in reality, several tens of thousand single assembly calculations are necessary.

On the other hand, when I carry out the 36 patterns of two assembly calculations, its computational load approximately corresponds to 150 (~36×4) single assembly calculations. Note that I assume that the computational load of two assembly calculation is comparable to 4 single assembly calculations.

Therefore, the least squares approximation for the relationships between the coarse group cross sections and LIs obtained by the two assembly calculations is more efficient than the direct calculations based on Equation (4.34).

4.3.1.3. Verifications of present correction technique

In order to verify the applicability of the present correction technique, two dimensional benchmark problems considering typical characteristics of BWR cores are carried out. In the benchmark problems, I consider the energy collapsing of cross sections from 47 to 4 and 8 energy groups, whose structures are shown in **Table 4-1** [17].

Table 4-1 Energy group structure

4-group structure	8-group structure	Lower energy boundary [eV]
1st group	1st group	2.2313E+06
	2nd group	8.2085E+05
	3rd group	9.1188E+03
2nd group	4th group	1.3007E+02
	5th group	3.9279E+00
3rd group	6th group	6.2506E-01
4th group	7th group	1.4572E-01
	8th group	1.0000E-04

Through the numerical verifications with 4 and 8 energy group structures, firstly, I discuss the applicability of the present correction technique for finer group cross sections. Next, I also discuss the degree of freedom of correction in the present technique, which relates to the performance of cross section reproductions. These discussions will be done by comparing the calculation results between different energy group structures.

In this Chapter, I use 4×4 colorset assembly geometry with the periodic boundary condition shown in **Figure 4.3**, which consists of different types of 8×8 BWR fuel assemblies shown in Figure 4.2.

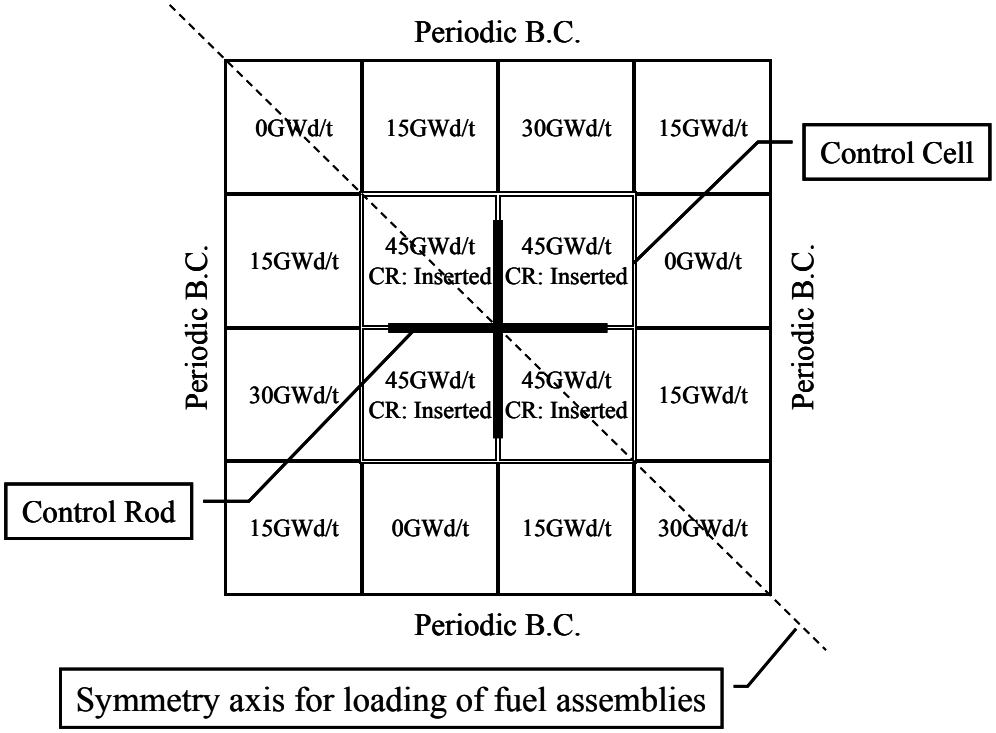

Figure 4.3 Geometry of 4×4 colorset assemblies in Chapter 4

In Figure 4.3, 2×2 fuel assemblies, which are located in the center of 4×4 colorset assembly geometry, simulate a control cell and are same fuel assemblies (*i.e.*, the assembly-averaged exposure and the type of fuel assembly are same). For other fuel assemblies loaded around the control cell the assembly-averaged exposures are fixed as shown in Figure 4.3 and the types of fuel assemblies are randomly determined considering the diagonal symmetry of 4×4 colorset assembly geometry. Through these procedures, I determine approximately 6,500 patterns of 4×4 colorset assembly geometries, which are combinations of three types of fuel assemblies for the control cell and surrounding seven assemblies (*i.e.*, 3^8 patterns). Note that the assembly-averaged void fraction is 40%. Since I assume that the cycle length is 15GWd/t and consider the loading pattern of fuel assemblies in the beginning of cycle, the assembly-averaged exposure is chosen from 0, 15, 30, and 45GWd/t.

4.3.2. Calculation procedure to correct coarse group cross sections

In the present correction technique using the leakage index, the coarse group cross sections are corrected by the following procedures. Note that iteration calculations are necessary to update coarse group cross sections since the LIs in the target colorset fuel assembly (*i.e.*, $LI_{m,G}$ in Equation (4.35)) are unknown.

(1) Single assembly calculations in coarse group are carried out for all types of fuel assemblies, which are used in the target colorset assembly geometry. Through such single assembly calculations, $LI_{m,G}^{single}$ in Equation (4.35) are calculated for each pin-cell meshes.

(2) Target colorset assembly calculation in coarse group is carried out with the uncorrected coarse group cross sections. Namely, $LI_{m,G'}^{colorset}$ and $d\Sigma_{x,m,G}$ in Equation (4.35) are assumed to be $LI_{m,G}^{single}$ and zero, respectively, in this step.

(3) By using the neutron fluxes and the k-effective obtained by the target colorset assembly calculation, the LIs perturbed by the spectral interference effect calculated. Namely, $LI_{m,G'}^{colorset}$ in Equation (4.35) are updated.

(4) Based on Equation (4.35), the variations of coarse group cross sections are recalculated by the LIs obtained in the steps (1) and (3) (*i.e.*, $LI_{m,G}^{single}$ and $LI_{m,G'}^{colorset}$) and the coupling coefficients of LIs pre-calculated in the section 4.2.3.

(5) Target colorset assembly calculation in coarse group is carried out with the corrected coarse group cross sections obtained in the step (4).

(6) The steps (3) to (5) are repeated until the k-infinity and the pin-by-pin fission rate distribution of the target colorset assembly calculation are converged.

4.3.3. Calculation results and remarks

In order to verify the applicability of the present correction technique, I compare the k-infinities and the pin-by-pin fission rate distributions of several 4×4 colorset assembly geometries. The pin-by-pin (cell-homogenized) calculations in the single and the colorset assembly geometries are performed by the diffusion method. The finite difference method is used for the spatial discretization in the diffusion method. The absolute value of relative difference of k-infinity and the root-mean-square (RMS) difference of pin-by-pin fission rate distribution are calculated as:

$$\Delta k_{inf} = \left| \frac{k_{inf}^{calculated} - k_{inf}^{reference}}{k_{inf}^{reference}} \right|, \tag{4.36}$$

$$\Delta R_{f,RMS} = \sqrt{\frac{\sum_{m \in fuel\,mesh} \left(R_{f,m}^{calculated} - R_{f,m}^{reference} \right)^2}{N_{fuel\,mesh}}}, \tag{4.37}$$

where Δk_{inf}, $\Delta R_{f,RMS}$, $R_{f,i}$, and $N_{fuel\ mesh}$ are the absolute value of relative difference of k-infinity, the RMS difference of pin-by-pin fission rate distribution, the pin-by-pin fission rate on fuel mesh m, and the total number of fuel meshes, respectively. The superscripts *calculated* and *reference* represent the calculations with the coarse group cross sections corrected (or not corrected) by the present correction technique and those with the reference cross sections, respectively. In the present verifications, the coarse group cross sections obtained by direct collapsing of fine group cross sections in the target colorset assembly geometry are used as the reference cross sections. Note that reproducibility of coarse group cross section by applying the present correction technique is major interest in this Chapter. Thus, the SPH method is used to reduce the spatial homogenization errors but is not used to reduce the energy collapsing errors. The direct comparisons with the fine group or the HELIOS calculations will be addressed in a future study since the treatment of the SPH factor considering the spectral interference effect has not been investigated yet as described previously.

The absolute value of relative difference of k-infinities and the RMS difference of pin-by-pin fission rate distributions calculated with 4-group and 8-group cross sections are shown in **Figures 4.4** and **4.5**, respectively. In **Table 4-2**, these calculation results are summarized. In Figures 4.4 and 4.5 and Table 4-2, the calculation results obtained by the coarse group cross sections corrected by the present correction technique and those not corrected (*i.e.*, only collapsed in single assembly geometries) are represented as “Corrected” and “Not-Corrected”, respectively.

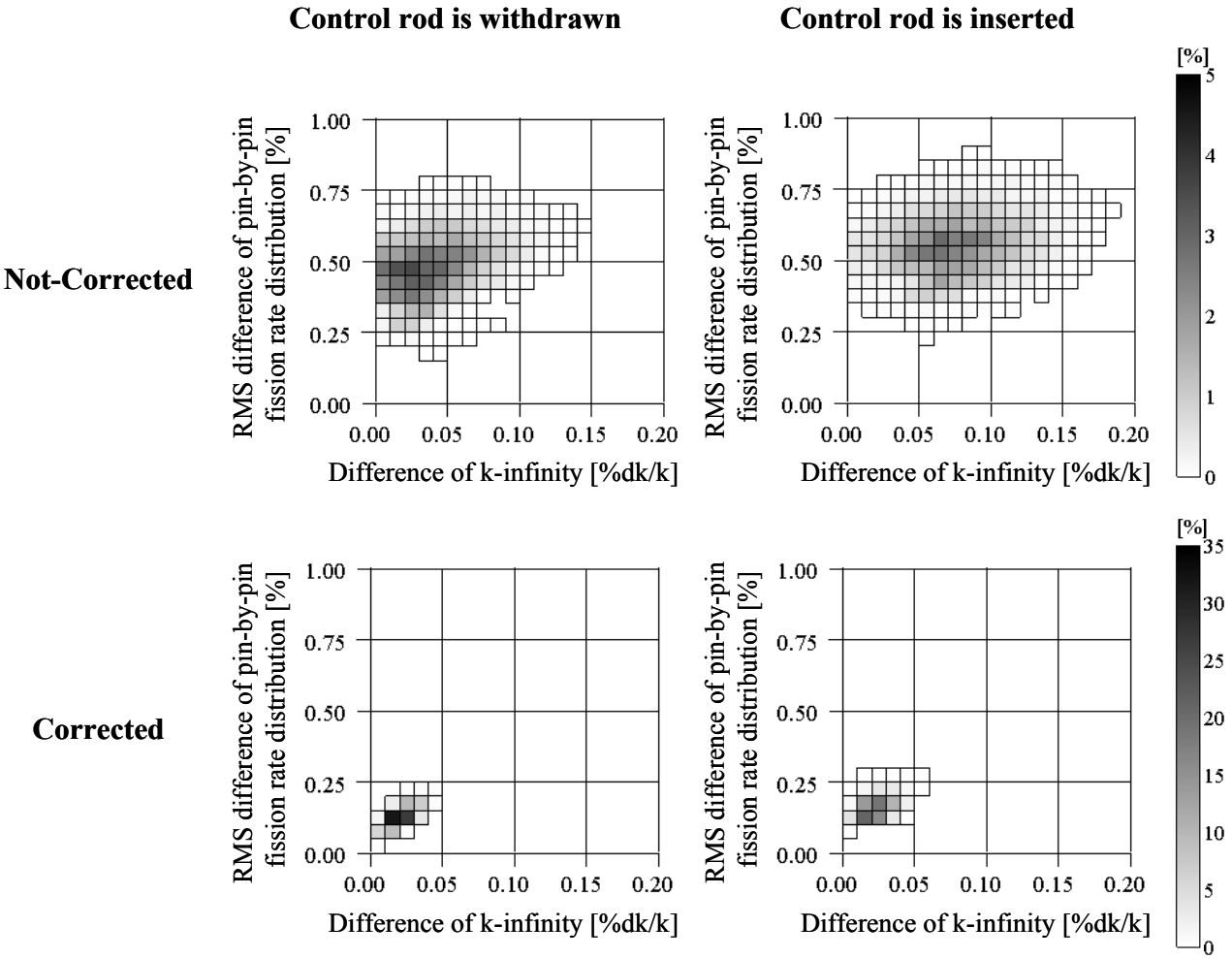

Figure 4.4 Frequency distributions of k-infinity and pin-by-pin fission rate distribution (4 groups)

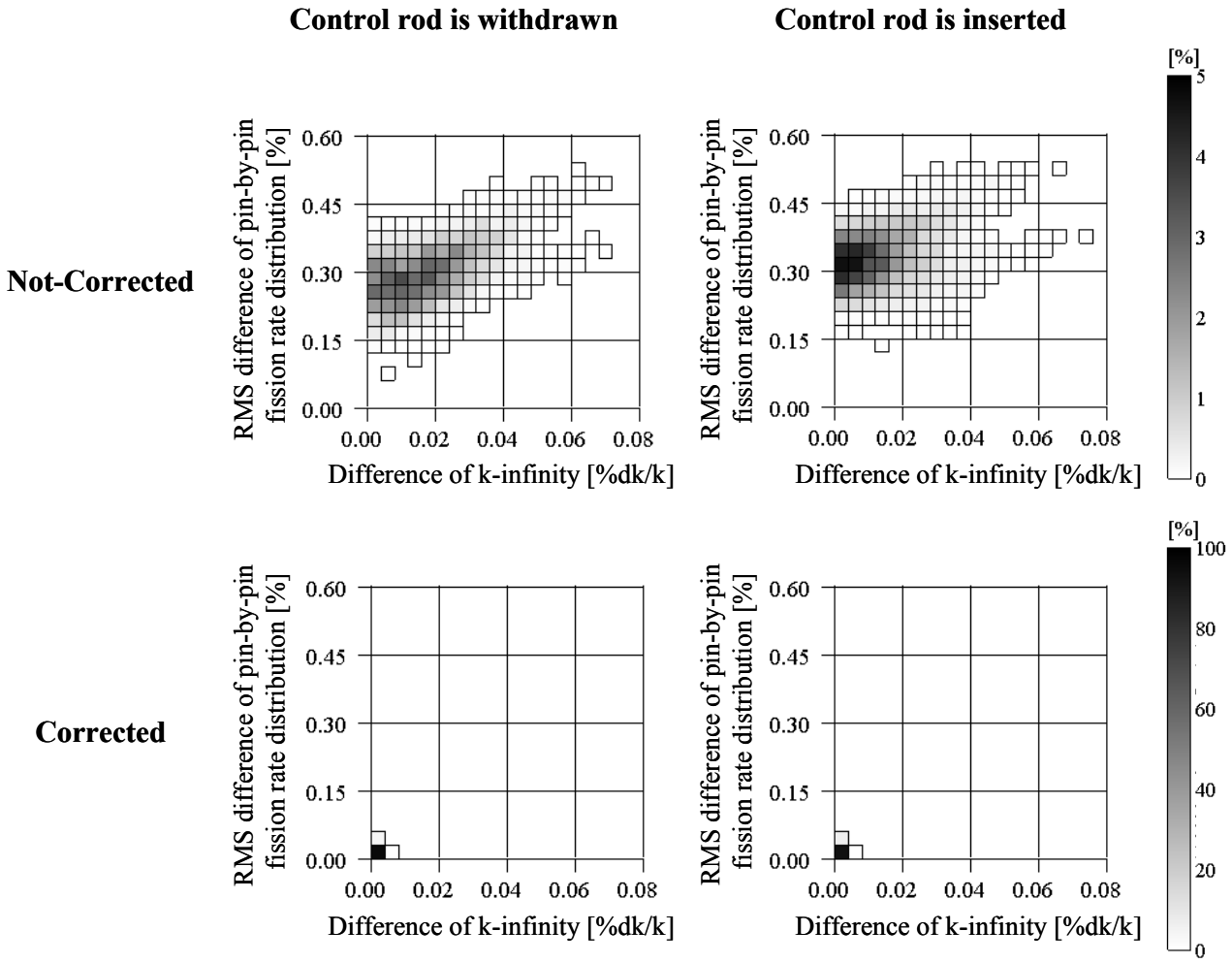

Figure 4.5 Frequency distributions of k-infinity and pin-by-pin fission rate distribution (8 groups)

Table 4-2 Summary of calculation results

Control rod: Withdrawn		4-group structure		8-group structure	
		Corrected	Not-Corrected	Corrected	Not-Corrected
Δk_{inf} [%dk/k]	Average	0.02	0.04	0.00	0.02
	Maximum	0.05	0.14	0.00	0.07
$\Delta R_{f,RMS}$ [%]	Average	0.13	0.48	0.02	0.29
	Maximum	0.23	0.79	0.04	0.51
Control rod: Inserted		4-group structure		8-group structure	
		Corrected	Not-Corrected	Corrected	Not-Corrected
Δk_{inf} [%dk/k]	Average	0.02	0.07	0.00	0.01
	Maximum	0.05	0.19	0.01	0.07
$\Delta R_{f,RMS}$ [%]	Average	0.16	0.55	0.02	0.33
	Maximum	0.28	0.86	0.04	0.54

From Figures 4.4 and 4.5, the calculation accuracies of k-infinity and pin-by-pin fission rate distribution are improved by applying the present correction technique using the LIs. These improvements are observed on all calculation cases, whose loading patterns are randomly determined. Therefore, the present correction technique using the LIs is valid to correct coarse group cross sections considering the spectral interference effect. From Table 4-2, the improvements of calculation accuracies are observed for the energy collapsing from 47 to both of 4 and 8 energy groups. Thus, Equation (4.35), which is derived from Equation (4.30), would be valid and can capture the impacts of variations of neutron leakages due to the spectral interference effect.

In order to estimate the reproducibility of coarse group cross sections calculated by Equation (4.35), I also estimate the RMS difference of coarse group cross sections, which is potentially caused on the present correction technique, as:

$$R_{x,m,G} = \sqrt{\frac{\sum_{i \in \substack{two\,assembly \\ geometry}} \left\{ 1 - \left(\Sigma^{single}_{x,m,G} + \sum_{G'} a_{x,m,G,G'} \left(LI^{i}_{m,G'} - LI^{single}_{m,G'} \right) \right) \Big/ \Sigma^{colorset}_{x,m,G} \right\}^2}{N_{\substack{two\,assembly \\ geometry}}}}, \qquad (4.38)$$

where R and $N_{two\ assembly\ geometry}$ are the RMS difference of coarse group cross sections and the number of two assembly geometries used to calculate the coupling coefficients (*i.e.*, quadruple of the number of simplified fuel assemblies), respectively.

The RMS differences of absorption cross sections and diffusion coefficients in the MOX fuel assembly without the control rod are shown in **Figures 4.6** and **4.7**, respectively. Note that the assembly averaged void fraction and the assembly-averaged exposure of MOX fuel assembly are 40% and 0GWd/t, respectively.

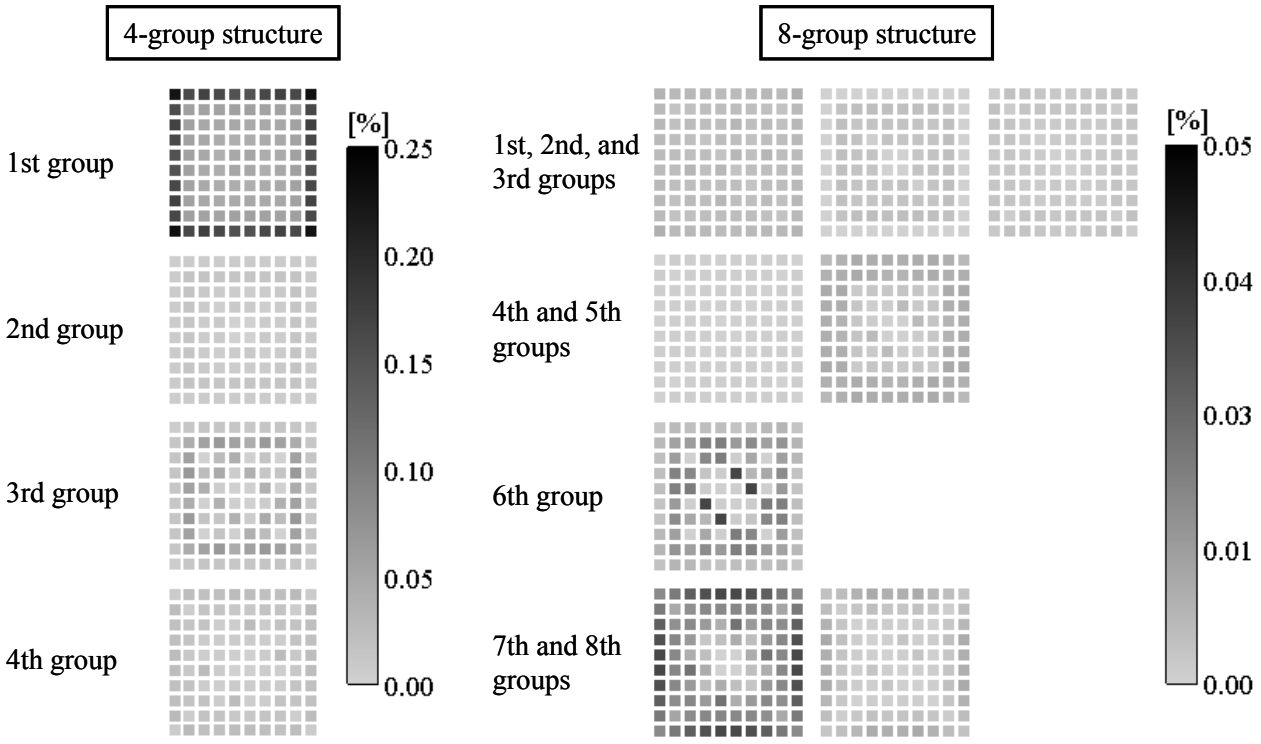

Figure 4.6 RMS differences of absorption cross sections in MOX fuel assembly (void fraction: 40%, exposure: 0GWd/t)

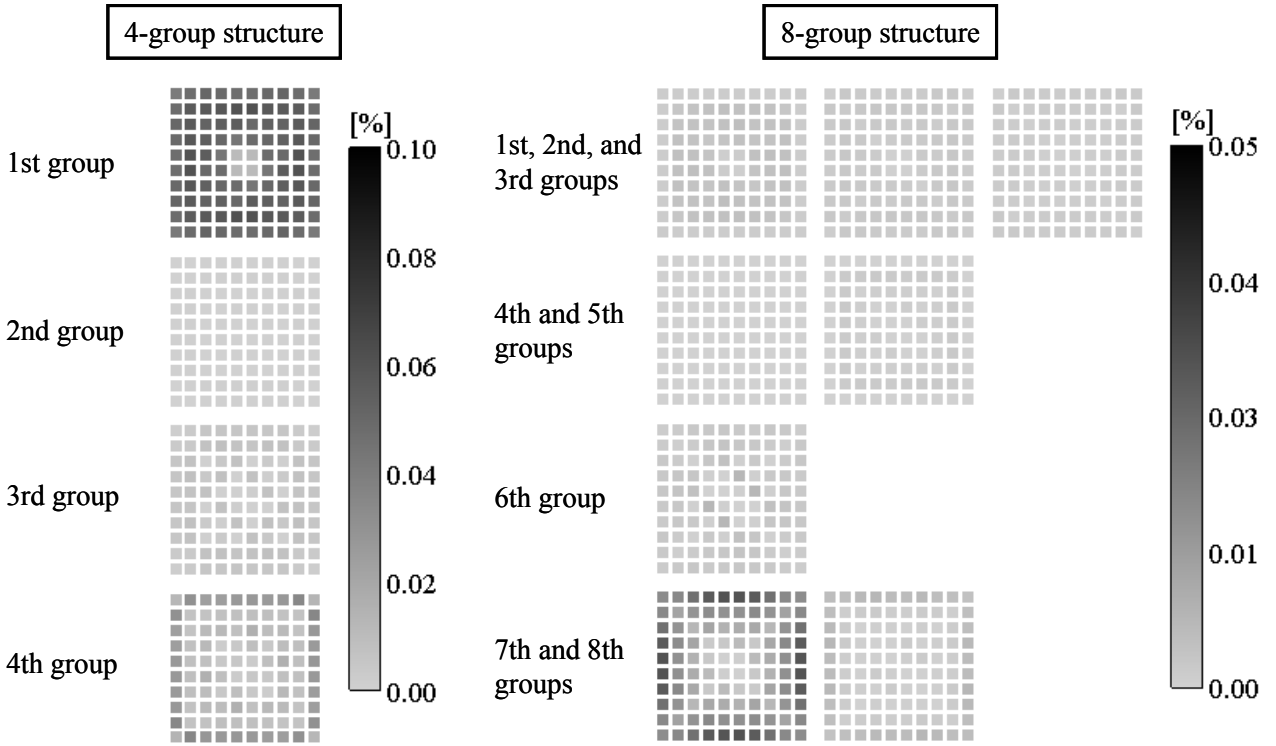

Figure 4.7 RMS differences of diffusion coefficients in MOX fuel assembly (void fraction: 40%, exposure: 0GWd/t)

From Figure 4.6, the RMS differences of 6th group absorption cross sections in 8-group structure are about 0.05% in water rod meshes and those of 7th group absorption cross sections are about 0.05% in peripheral meshes. However, the RMS differences of other group absorption cross sections are less than 0.01%. In 4-group structure, the RMS differences absorption cross sections have different tendencies from those in 8-group structure. They are generally larger than those in 8-group structure. The RMS differences of 1st group absorption cross sections in 4-group structure are about 0.25% in peripheral meshes. From Figure 4.7, the RMS differences of 7th group diffusion coefficients in 8-group structure are about 0.04% in peripheral meshes and those of other group diffusion coefficients are less than 0.01%. On the other hand, in 4-group structure, the RMS differences of 1st group diffusion coefficients become much larger in almost meshes. Note that similar results are observed for other types of reactions (*e.g.*, production, fission, and scattering) and for other types of fuel assemblies (*i.e.*, the low-enrichment UO_2 and the high-enrichment UO_2 fuel assemblies).

From the results described the above, the differences of cross sections in 4-group structure become larger than those in 8-group structure and they are mainly observed in peripheral meshes, in

which the impact of the spectral interference effect generally becomes large. The impact of spectral interference effect in 8 groups are generally smaller than that in 4 groups and the degree of freedom for the present correction technique in 8 groups is greater than that in 4 groups as shown in Equation (4.35). Therefore, since the reproducibility of 8-group cross sections becomes better than that of 4-group cross sections, the differences of k-infinity and pin-by-pin fission rate distribution in 8-group structures shown in Figures 4.4 and 4.5 and Table 4-2 are smaller than those in 4-group structures.

4.4. Conclusions

In this Chapter, I propose a new correction technique for coarse group cross sections in the pin-by-pin core calculations considering the spectral interference effect, which is caused by the adjacent loading of different types of fuel assemblies.

In the present correction technique, I focus on the perturbation of neutron leakage, thus, I newly introduce the LI, which is defined as the macroscopic cross section of volume-averaged neutron leakage value. From theoretical discussion utilizing the generalized perturbation theory, the variations of coarse group cross sections are approximately represented by the fine group generalized adjoint flux, neutron flux, and LI. However, since core calculations in the conventional core analysis are performed with coarse group cross sections, I cannot directly estimate such fine group parameters. Therefore, I approximate the variation of coarse group cross sections as the linear combination of coarse group LIs.

In order to apply the present correction technique with the linear combination of coarse group LIs, it is necessary to estimate the coupling coefficients of LIs in prior to core calculations. Although the coupling coefficients of LIs are estimated by performing several colorset assembly calculations, I have no prior knowledge on the types of fuel assemblies (*e.g.*, the assembly-averaged exposure and the enrichment distribution) loaded into the adjacent regions of the target fuel assembly in actual cores. Thus, I prepare various simplified fuel assemblies separately from the target fuel assemblies. For the simplified fuel assemblies, the assembly-averaged void fraction, the assembly-averaged exposure of fuel assembly, and the fuel rod enrichment of ^{235}U or Pu-fissile are chosen from the values of typical BWR fuel assemblies though the fuel rod enrichment splitting is neglected. In order to obtain the relationship between the coarse group cross sections and LIs, calculations are carried out in single and colorset assembly geometries. In this Chapter, I use two assembly geometries with reflective boundary condition

as colorset assembly geometries. With the calculation results obtained through the single assembly and the colorset assembly calculations, the coupling coefficients of LIs are calculated by applying the least squares approximation.

Verification calculations are carried out for 4×4 colorset assembly geometries including the control cell and the energy collapsing from 47 to 4 and 8 energy groups is considered. I perform the pin-by-pin fine mesh calculations based on the diffusion theory and compare the k-infinity and the pin-by-pin fission rate distribution. In the present verification, coarse group cross sections directly collapsed in target 4×4 colorset assembly geometries are used to obtain the reference results in order to focus on the reproducibility of coarse group cross sections by the present correction technique.

From the comparisons, the calculation accuracies of k-infinity and pin-by-pin fission rate distribution are improved by applying the present correction technique using the LIs. Therefore, the present correction technique using the LIs well reproduces the coarse group cross sections considering the spectral interference effect.

Consequently, the present correction technique using the LIs is useful in order to correct coarse group cross sections considering the spectral interference effect on pin-by-pin BWR core analysis.

References

[1] K. R. Rempe, K. S. Smith, "SIMULATE-3 Pin Power Reconstruction: Methodology and Benchmarking," *Nucl. Sci. Eng.*, **10**, pp. 334-342, (1989).

[2] T. Iwamoto, M. Yamamoto, "Pin Power Reconstruction Methods of the Few-Group BWR Core Simulator NEREUS," *J. Nucl. Sci. Technol.*, **36**[12], pp. 1141-1152, (1999).

[3] S. Palmtag, K. Smith, "Two-Group Spectral Corrections for MOX Calculations," *Proc. Int. Conf. on Physics of Reactors (PHYSOR98)*, Oct. 5-8, 1998, Long Island, New York, (1998). [CD-ROM].

[4] T. Ida, Y, Tahara, "Two-Group Micro-Depletion Correction Model for ALPHA/PHENIX-P/ANC Code System," *Proc. Int. Conf. on the Physics of Reactors (PHYSOR 2000)*, May 7-11, 2000, Pittsburgh, Pennsylvania, (2000). [CD-ROM].

[5] K. Yamaji, H. Matsumoto, M. Nakano, "Development of the New Pin-by-pin Core Calculation Method with Embedded Heterogeneous Assembly Calculation," *Proc. Int. Conf. on Physics of Reactors (PHYSOR 2006)*, Sep. 10-14, 2006, Vancouver, Canada, (2006). [CD-ROM].

[6] N. Z. Cho, S. Yuk, H. J. Yoo *et al*, "Overlapping Local/Global Iteration Framework for Whole-Core Transport Solution," *Proc. Int. Conf. on the Physics of Reactors (PHYSOR 2012*),Apr. 15-20, 2012, Knoxville, Tennessee, (2012). [CD-ROM].

[7] K. Tada, A. Yamamoto, Y. Yamane *et al.*, "Applicability of the Diffusion and Simplified P3 Theories for Pin-by-Pin Geometry of BWR," *J. Nucl. Sci. Technol.*, **45**[10], pp. 997-1008, (2008).

[8] K. Tada, A. Yamamoto, Y. Yamane, "Treatment of Staggered Mesh for BWR Pin-by-Pin Core Analysis," *J. Nucl. Sci. Technol.*, **46**[2], pp. 163-174, (2009).

[9] M. Tatsumi, A. Yamamoto, "Advanced PWR Core Calculation Based on Multi-group Nodal-transport Method in Three-dimensional Pin-by-Pin Geometry," *J. Nucl. Sci. Technol.*, **40**[6], pp. 376-387, (2003).

[10] F. Rahnema, E. M. Nichita, "Leakage Corrected Spatial (Assembly) Homogenization Technique," *Ann. Nucl. Energy*, **24**, pp. 477-488, (1997).

[11] S. Douglass, F. Rahnema, "Subgroup Decomposition Method," *Ann. Nucl. Energy*, **48**, pp. 84-101, (2012).

[12] K. T. Clarno, M. L. Adams, "Capturing the Effects of Unlike Neighbors in Single-Assembly Calculations," *Nucl. Sci. Eng.*, 149, pp. 182-196, (2005).

[13] K. Kobayashi, *Genshiro-buturi*, Corona Publishing Company, Tokyo, (1996). [in Japanese].

[14] H. Okuno, Y. Naito, K. Suyama, *OECD/NEA Burnup Credit Criticality Benchmarks Phase IIIB: Burnup Calculations of BWR Fuel Assemblies for Storage and Transport*, JAERI-Research 2002-001, Japan Atomic Energy Research Institute (JAERI), (2002).

[15] *HELIOS Methods (Version 1.11)*, Studsvik Scandpower, 2009.

[16] A. Hébert, "A Consistent Technique for the Pin-by-Pin Homogenization of A Pressurized Water Reactor Assembly," *Nucl. Sci. Eng.*, **113**, pp. 227-238, (1991).

[17] T. Kozlowski, T. J. Downar, *PWR MOX/UO_2 Core Transient Benchmark*, NEA/NSC/DOC(2006)20, OECD/NEA, (2007).

Chapter 4 is based on an Accepted Manuscript of an article published by Taylor & Francis in Journal of Nuclear Science and Technology on April 3rd, 2014, available online: http://wwww.tandfonline.com/10.1080/00223131.2014.903212.

Chapter 5. A spectral interference correction technique for coarse group cross sections on pin-by-pin core analysis (2): Application of correction technique using leakage index combined with SPH or discontinuity factors

5.1. Introduction

In Chapter 4, I propose a new correction technique in order to capture the spectral interference effect and to correct coarse group cross sections. In this correction technique, I assume that the spectral interference effect has relationship with variations of neutron leakage from the viewpoint of neutron balance. Moreover, a leakage index (LI), which is similar to a macroscopic cross section related to the neutron leakage, is newly used as a correction index. Through the mathematical derivations using the generalized perturbation theory based on the diffusion theory, the variations of coarse group cross sections due to the spectral interference effect are approximately represented by the linear combination of variations of coarse group LIs. From the verification calculation results in Chapter 4, it is confirmed that the correction technique using LI (i.e., the LI correction technique) can well reproduce the reference coarse group cross sections (*i.e.*, cross sections directly collapsed with consideration of the spectral interference effect). It should be reminded that even if the reference coarse group cross sections, which are collapsed with actual neutron spectrum in core geometries, are used, the coarse group calculations do not reproduce the reference fine group calculation results. The root cause of this inconsistency is the energy collapsing error, which should be considered in addition to the spectral interference effect. Namely, though the LI correction technique can well reproduce the reference coarse group calculation results, this cannot reduce the errors between the fine and the coarse group calculation results. Therefore, in order to reproduce the reference fine group calculation results, combinations of the LI correction technique with other correction techniques, which reduce the energy collapsing errors, are necessary.

In this Chapter, I focus on the SPH factor and the DF, which can reduce the energy collapsing errors [1, 2]. Then, I try to combine the LI correction technique with either the SPH factor or the DF in this Chapter (*i.e.*, the LI correction technique with the SPH factor and that with the DF are investigated). Since the LI correction technique is proposed in Chapter 4, the performance of such combination has not been investigated and confirmed so far. Only the spectral interference effect on energy collapsing of cross sections is investigated in this Chapter but the spectral interference effect on spatial

homogenization of cross sections is not investigated. The similar investigation for the spectral interference effect on spatial homogenization will be necessary in order to fully verify the applicability of the LI correction technique with the SPH factor or the DF in the practical use. However, it is not discussed in this Chapter since I focus on the energy collapsing error.

Concepts of combination of the correction techniques are described in section 5.2. The verification results of the LI correction technique with the SPH factor or the DF are shown in section 5.3 through numerical benchmark calculations. Finally, the concluding remarks are given in section 5.4.

5.2. Methodology

In this section, firstly, the overview of the LI correction technique is described in order to make this Chapter self-explanatory. Then, the concepts of combinations of the LI correction technique with the SPH factor or the DF are shown.

5.2.1. Overview of LI correction technique

The conventional core analysis consists of lattice physics and core calculations. Coarse group cross sections for core calculations are obtained by collapsing fine group cross sections with fine group neutron fluxes through lattice physics calculations in single assembly geometries:

$$\Sigma_{x,G} = \frac{\sum_{g \in G} \Sigma_{x,g} \phi_g}{\sum_{g \in G} \phi_g}, \tag{5.1}$$

where Σ and ϕ are the macroscopic cross section and the neutron flux, respectively. The subscripts of x, g, and G represent the reaction type (*e.g.*, fission and absorption), the fine group index, and the coarse group index, respectively. However, the neutron fluxes used in Equation (5.1) (*i.e.*, calculated in single assembly geometries) are different from those obtained in core geometries, since the spatial and the energetic distribution of neutron fluxes in core geometries become different by the spectral interference effect. Thus, coarse group cross sections, which are calculated through lattice physics analyses in single assembly geometries, become different from the appropriate coarse group cross sections for core calculations.

In order to correct coarse group cross sections considering the spectral interference effect, I

focus on neutron leakages in each pin-cell and consider the relationship between the variations of coarse group cross sections and neutron leakage. In order to express the neutron leakage, I newly introduce the LI defined by:

$$LI_g(\vec{r}) \equiv \frac{\int_S \overrightarrow{J_g}(\vec{r}) \cdot \vec{n}(\vec{r}) dS \Big/ \int_V dV}{\phi_g(\vec{r})}, \tag{5.2}$$

which is an index parameter related to neutron leakage and is defined as a macroscopic cross section of volume-averaged neutron leakage. From the viewpoint of neutron balance in the k-effective eigenvalue calculation, the LI is calculated by:

$$LI_g(\vec{r}) = \frac{\int_V \frac{\chi_g(\vec{r})}{k_{eff}} \sum_{g'} \nu\Sigma_{f,g'}(\vec{r})\phi_{g'}(\vec{r}) + \sum_{g' \neq g} \Sigma_{s,g' \to g}(\vec{r})\phi_{g'}(\vec{r}) - \Sigma_{r,g}(\vec{r})\phi_g(\vec{r}) dV \Big/ \int_V dV}{\phi_g(\vec{r})}. \tag{5.3}$$

From Equation (5.3), the dimension of LI is the same as macroscopic cross sections. Namely, the LI is considered as a macroscopic cross section related to the neutron leakage. By using the LI in Equation (5.2) and by considering the perturbations of LI, I approximately represent the variations of coarse group cross sections as the linear combination of variations of coarse group LIs:

$$d\Sigma_{x,m,G} \approx \sum_{G'} a_{x,m,G,G'} dLI_{m,G'} = \sum_{G'} a_{x,m,G,G'} \left(LI_{m,G'} - LI_{m,G'}^{single} \right), \tag{5.4}$$

where a is the coupling coefficients of LIs. The superscript *single* represents single assembly calculations. In order to calculate the coupling coefficients of LIs in Equation (5.4), I perform various simplified colorset assembly calculations, which consist of the target and the simplified fuel assemblies described in section 5.3.1, and simulate actual impacts of spectral interference effect in core geometries. In this Chapter, Equation (5.4) is used for all reaction types of cross sections (*i.e.*, absorption, fission, and production cross sections, scattering matrices, and diffusion coefficients) since they are collapsed

with neutron fluxes as Equation (5.1).

Note that the detailed mathematical descriptions of derivations of Equation (5.4) can be found in Chapter 4.

5.2.2. Combination of LI correction technique with SPH factor or DF

In the previous section, the overview of the LI correction technique is described. The LI correction technique based on Equation (5.4) can reduce errors due to the spectral interference effect and well reproduces the reference coarse group cross sections. However, even if the reference coarse group calculation results are well reproduced, errors due to the energy collapsing of cross sections still exist (*i.e.*, the reference fine group calculation results are not reproduced). Thus, it is necessary to combine the LI correction technique and other correction methods, which reduce the energy collapsing errors.

It is possible to reduce the energy collapsing errors by the SPH factor or the DF. For the energy collapsing of cross sections, these are calculated as:

$$\mu_G = \frac{\sum_{g \in G} \phi_g}{\phi_G}, \tag{5.5}$$

$$f_G = \frac{\sum_{g \in G} \phi_{s,g}}{\phi_{s,G}}, \tag{5.6}$$

where ϕ, ϕ_s, μ, and f are the region-averaged neutron flux, the region-surface neutron flux, the SPH factor, and the DF, respectively. The subscript of g and G represent the fine energy group and the coarse energy group indices, respectively. In this Chapter, the SPH factor and the DF are calculated in each pin-cell mesh and in every surfaces of pin-cell mesh, respectively.

Similar to coarse group cross sections, the SPH factor and the DF in core geometries are also different from those in single assembly geometries by the spectral interference effect. Thus, the variations of the SPH factor and the DF would be taken into account. In our preliminary investigations, I tried to simultaneously correct the coarse group cross sections and the SPH factor by the LI correction technique. However, this approach encountered the following difficulty.

In order to estimate the variations of SPH factor due to the spectral interference effect, calculations of the SPH factor in every simplified colorset assembly geometries are necessary in order to simulate actual impacts of spectral interference effect in core geometries. Thus, the calculation procedure of LI correction technique becomes very complicated. Moreover, in the LI correction technique based on the diffusion theory, the LI defined in Equation (5.3) are used to correct the coarse group cross sections and the neuron fluxes are necessary to estimate the LI. If the SPH factor simultaneously changes with the coarse group cross sections, the corrections of coarse group cross sections and SPH factor would conflict each other over the variations of neutron fluxes. As the results of such conflict, the calculation procedure of LI correction technique becomes unstable from the viewpoint of numerical calculation. When the equivalence between the SPH factor and the DF (i.e., the SPH factor corresponds to the inverse of region-averaged DF) is considered, the simultaneous correction of coarse group cross sections and DF would present the same problems as the SPH factor.

Therefore, in this Chapter, I assume that dependences of SPH factor and DF on the spectral interference effect are not significant. Namely, the SPH factor and the DF, which are calculated in single assembly geometries, are used during the calculation procedure of LI correction technique. With this approximation, I can avoid the instabilities of numerical calculations of LI correction technique.

The overview of calculation procedure of LI correction technique with the SPH factor or the DF is shown in **Figure 5.1**.

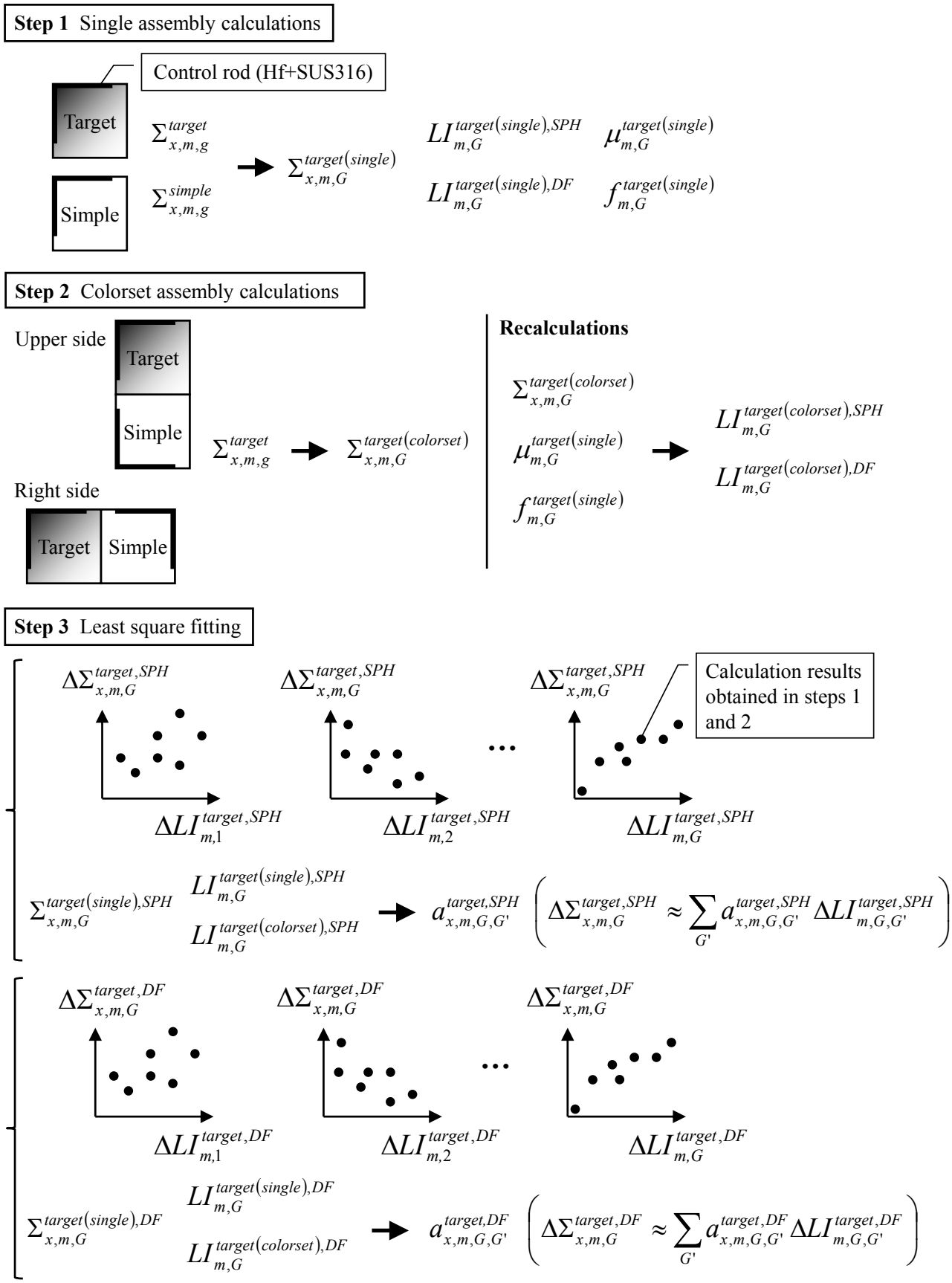

Figure 5.1 Overview of calculation procedure of LI correction technique with SPH factor and DF

As shown in Figure 5.1, firstly, single assembly calculations are carried out for target and simplified fuel assemblies. Coarse group cross sections ($\Sigma_{x,m,G}^{target(single)}$) are collapsed in single assembly geometries and the SPH factor and the DF ($\mu_{m,G}^{target(single)}$ and $f_{m,G}^{target(single)}$) are calculated. By utilizing the calculation results (i.e., the neutron fluxes and the k-effective) and the SPH factor, coarse group LIs ($LI_{m,G}^{target(single),SPH}$) are estimated. Similarly, by utilizing the calculation results and the DF, coarse group LIs ($LI_{m,G}^{target(single),DF}$) are also estimated. Note that the coarse group LIs, which are obtained with the SPH factor or the DF, are calculated as:

$$LI_{m,G}^{SPH} = \frac{\frac{\chi_{m,G}}{k_{eff}^{SPH}} \sum_{G'} \mu_{m,G'} \nu\Sigma_{f,m,G'} \phi_{m,G'}^{SPH} + \sum_{G' \neq G} \mu_{m,G'} \Sigma_{s,m,G' \to G} \phi_{m,G'}^{SPH} - \mu_{m,G} \Sigma_{r,m,G} \phi_{m,G}^{SPH}}{\mu_{m,G} \phi_{m,G}^{SPH}}, \qquad (5.7)$$

$$LI_{m,G}^{DF} = \frac{\frac{\chi_{m,G}}{k_{eff}^{DF}} \sum_{G'} \nu\Sigma_{f,m,G'} \phi_{m,G'}^{DF} + \sum_{G' \neq G} \Sigma_{s,m,G' \to G} \phi_{m,G'}^{DF} - \Sigma_{r,m,G} \phi_{m,G'}^{DF}}{\phi_{m,G}^{DF}}. \qquad (5.8)$$

Note that $\mu_{m,G} \phi_{m,G}^{SPH}$ in the coarse group calculation is equivalent to the summation of fine group neutron fluxes. Furthermore, in the coarse group calculations with the DF, $\phi_{m,G}^{DF}$ is equivalent to the summation of fine group neutron fluxes. Thus, the coarse group LIs obtained by Equations (5.7) or (5.8) is consistent with those obtained by the fine group calculation results.

Secondly, fine group calculations are carried out in colorset assembly geometries, which consist of the target and the simplified fuel assemblies. Coarse group cross sections ($\Sigma_{x,m,G}^{target(colorset)}$), which are directly collapsed in colorset assembly geometries, are estimated. By the coarse group cross sections ($\Sigma_{x,m,G}^{target(colorset)}$), the SPH factor or the DF ($\mu_{m,G}^{target(single)}$ or $f_{m,G}^{target(single)}$), and the neutron fluxes in the target and the simplified fuel assemblies, the LIs ($LI_{m,G}^{target(colorset),SPH}$ and $LI_{m,G}^{target(colorset),DF}$) in the target fuel assembly are calculated by Equations (5.7) and (5.8), respectively.

The colorset assembly geometries should be chosen to cover actual impacts of spectral interference effect. Thus, similar to Chapter 4, I assume that actual impacts of spectral interference effect can be simulated two assembly geometries with reflective boundary condition, in which the target and the simplified fuel assemblies are adjacently loaded. As shown in Chapter 4, utilizations of such two

assembly geometries and the simplified fuel assemblies are justified due to the following viewpoints;

(1) The spectral interference effect is mainly observed in the assembly peripheral meshes. Thus, the actual impacts of spectral interference effect can be decomposed into the impact from each assembly surface.

(2) BWR fuel assemblies have geometric symmetries. Thus, two types of two assembly geometries shown in Figure 5.1 can cover the impacts of spectral interference effect on each assembly surface.

(3) In order to consider the control rod insertion on actual operating core, larger colorset assembly geometries (*e.g.*, 4×4 colorset assembly geometries) should be used and larger computational load is necessary. Thus, the treatment of control rod insertion is approximated.

(4) The enrichment distribution of adjacent fuel assemblies is unknown in prior to core calculations. Moreover, the spectral interference effect is mainly observed in the assembly peripheral meshes. I consider that the average enrichment of fuel assembly has larger impact on the spectral interference effect than the enrichment distribution in a fuel assembly. Therefore, the uniform enrichment distribution is used for simplified fuel assemblies in order to simplify colorset assembly geometries and to reduce computational load.

Finally, the coupling coefficients of LIs ($a_{x,m,G,G'}^{target,SPH}$ and $a_{x,m,G,G'}^{target,DF}$) are calculated for each pin-cell. The least squares approximation for the relationship between the variations of coarse group cross sections ($\Delta\Sigma_{x,m,G}^{target,SPH}$ or $\Delta\Sigma_{x,m,G}^{target,DF}$) and those of coarse group LIs ($\Delta LI_{m,G}^{target,SPH}$ or $\Delta LI_{m,G}^{target,DF}$) obtained in the steps 1 and 2 is used to estimate the coupling coefficients.

In this Chapter, three types of 8×8 BWR fuel assemblies shown in **Figure 5.2** are used for the target fuel assemblies [3].

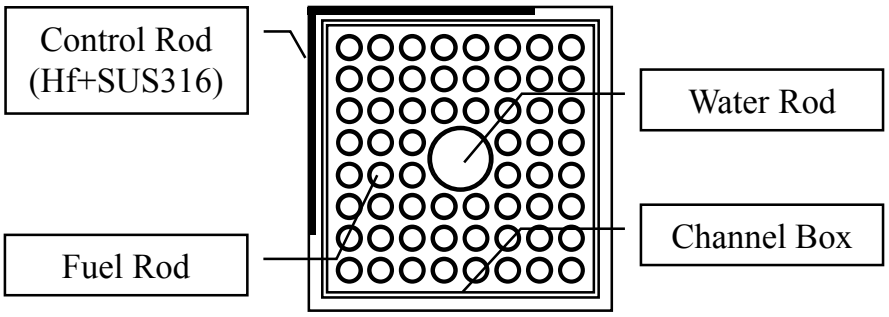

4	3	3	1	1	3	3	4
3	3	1	2	2	1	3	3
3	1	2	1	1	2	1	3
1	2	1			1	2	1
1	2	1			1	2	1
3	1	2	1	1	2	1	3
3	3	1	2	2	1	3	3
4	3	3	1	1	3	3	4

Low-enrichment UO_2 fuel assembly
(Assembly-averaged enrichment: 1.0wt% ^{235}U)

Type-1 1.2wt% ^{235}U
Type-2 1.0wt% ^{235}U
Type-3 0.8wt% ^{235}U
Type-4 0.7wt% ^{235}U

4	3	2	2	2	2	3	4
3	2	G	1	1	G	2	3
2	G	1	1	1	1	G	2
2	1	1			1	1	2
2	1	1			1	1	2
2	G	1	1	1	1	G	2
3	2	G	1	1	G	2	3
4	3	2	2	2	2	3	4

High-enrichment UO_2 fuel assembly
(Assembly-averaged enrichment: 3.5wt% ^{235}U)

Type-1 4.2wt% ^{235}U
Type-2 3.3wt% ^{235}U
Type-3 2.8wt% ^{235}U
Type-4 2.3wt% ^{235}U
Type-G 3.0wt% ^{235}U, 6.0wt% Gd

4	3	2	2	2	2	3	4
3	G	1	1	G	1	G	3
2	1	1	G	1	1	1	2
2	1	G			1	G	2
2	G	1			G	1	2
2	1	1	1	G	1	1	2
3	G	1	G	1	1	G	3
4	3	2	2	2	2	3	4

MOX fuel assembly
(Assembly-averaged enrichment: 4.0wt% Pu-fissile)

Type-1 4.8wt% Pu-fissile
Type-2 3.9wt% Pu-fissile
Type-3 3.2wt% Pu-fissile
Type-4 1.9wt% Pu-fissile
Type-G 2.0wt% ^{235}U, 3.0wt% Gd

Figure 5.2 8×8 BWR fuel assemblies used in Chapter 5

In the conventional and the next generation BWR core designs, 9×9 and 10×10 BWR fuel assemblies are also used in addition to the 8×8 BWR fuel assembly shown in Figure 5.2 [3, 4]. I think the average enrichment or Pu content of a fuel assembly has larger impact on the spectral interference effect than the assembly geometries (*e.g.*, the number and the radius of fuel rods). Thus, I use the 8×8 BWR fuel assembly as a typical one and consider several fuel rod enrichments of ^{235}U or Pu-fissile.

As shown in Figure 5.2, the low-enrichment UO_2 (assembly-averaged enrichment: 1.0wt% ^{235}U), the high-enrichment UO_2 (assembly-averaged enrichment: 3.5wt% ^{235}U), and the MOX

(assembly-averaged enrichment: 4.0wt% Pu-fissile) fuel assemblies are used. The geometry of these 8×8 fuel assembly are taken by the reference [3]. The fuel rod enrichment distributions are manually decided with the considerations for the positions of Gd-bearing fuel rods and the fuel rod enrichment distributions in the reference [3, 4].

Six types of fuel assemblies with the uniform enrichment distribution are used for simplified fuel assemblies. The fuel rod enrichments are 1.0 wt% ^{235}U, 3.0 wt% ^{235}U, 5.0 wt% ^{235}U, 3.0 wt% Pu-fissile, 4.0 wt% Pu-fissile, and 5.0 wt% Pu-fissile. Enrichments of ^{235}U and Pu-fissile are chosen to cover the values used in typical BWR fuel assemblies. The geometry of simplified fuel assemblies is the same with that of target fuel assemblies (*i.e.*, the simplified fuel assemblies are also 8×8 BWR fuel assemblies).

Note that the above design conditions of target and simplified fuel assemblies (*i.e.*, the geometry and the enrichment distribution of target and simplified fuel assemblies) are the same with those described in Chapter 4.

5.3. Numerical calculations

5.3.1. Calculation conditions and preparations for correction

5.3.1.1. Preparation of pin-cell averaged cross sections

The pin-cell averaged cross sections used in this Chapter are calculated by the HELIOS code in 47 energy groups [5]. In the HELIOS code, the depletion calculation is performed in single assembly geometry with the reflective boundary condition. The void fraction, the control rod position, and the power density are fixed during the depletion calculation. Through the depletion calculations, I obtain the pin-cell averaged fine group cross sections at 0, 15, 30, 45, and 60GWd/t (assembly-averaged exposure). The fine group cross sections at 0, 15, 30, 45, and 60GWd/t are used to construct the two assembly geometries shown in the section 5.2.2 and the 4×4 colorset assembly geometries as described in later. The heterogeneous 47-group cross sections are homogenized in each pin-cell and the SPH method is applied for 47-group pin-cell averaged cross sections in single assembly geometries in order to reduce the spatial homogenization errors [1].

5.3.1.2. Estimations of coupling coefficients of leakage index

As shown in the section 5.2.2, the two assembly calculations, which consist of the target and the

simplified fuel assemblies, are carried out and the perturbations of boundary conditions due to the spectral interference effect are simulated. Then, the coupling coefficients of LIs are calculated with this condition. In this Chapter, I carry out 36 patterns of two assembly calculations for one target fuel assemblies. These 36 patterns of two assembly geometries are determined by the combinations of calculation conditions for simplified fuel assemblies as follows:

(1) Fuel rod enrichment of simplified fuel assembly (six patterns): 1.0 wt% ^{235}U, 3.0 wt% ^{235}U, 5.0 wt% ^{235}U, 3.0 wt% Pu-fissile, 4.0 wt% Pu-fissile, and 5.0 wt% Pu-fissile.

(2) Assembly-averaged exposure (three patterns): 0, 30, and 60GWd/t.

(3) Loading position of simplified fuel assemblies (two patterns): Upper and right sides for the target fuel assembly.

Note that the assembly-averaged void fraction is 40% and the void fraction distribution is assumed as uniform. From the reference [6], an in-channel void distribution has a considerable impact on the calculation results (*e.g.*, the k-infinity and the pin-by-pin fission rate distribution). However, consideration of an in-channel void distribution is beyond the scope of this Chapter, which aims verifications of simultaneous utilization of the LI corrections and the SPH or the DF correction. Treatment of in-channel void distribution is an important issue to be addressed in future work.

The above calculation conditions to estimate the coupling coefficients of coarse group LIs are the same with those described in Chapter 4. Moreover, the relationships between the variations of coarse group cross sections and LIs, which are obtained through 36 patterns of two assembly calculations, sufficiently cover those obtained through 4×4 colorset assembly calculations as described in later.

5.3.1.3. Calculation geometry and number of energy groups

In order to verify the present LI correction technique with the SPH factor or the DF, two dimensional benchmark problems considering typical characteristics of BWR cores are carried out. In the benchmark problems, I consider the energy collapsing of cross sections from 47 to 4 and 8 energy groups, whose structures are shown in **Table 5-1** [6, 8]. Through the numerical verifications with 4 and 8 energy group structures, I confirm that present LI correction technique with the SPH factor or the DF can be used for several energy group structures.

Table 5-1 Energy group structure

4-group structure	8-group structure	Lower energy boundary [eV]
1st group	1st group	2.2313E+06
	2nd group	8.2085E+05
	3rd group	9.1188E+03
2nd group	4th group	1.3007E+02
	5th group	3.9279E+00
3rd group	6th group	6.2506E-01
4th group	7th group	1.4572E-01
	8th group	1.0000E-04

In this Chapter, I use 4×4 colorset assembly geometry with the periodic boundary condition shown in **Figure 5.3**, which consists of three different types of 8×8 BWR fuel assemblies shown in Figure 5.2.

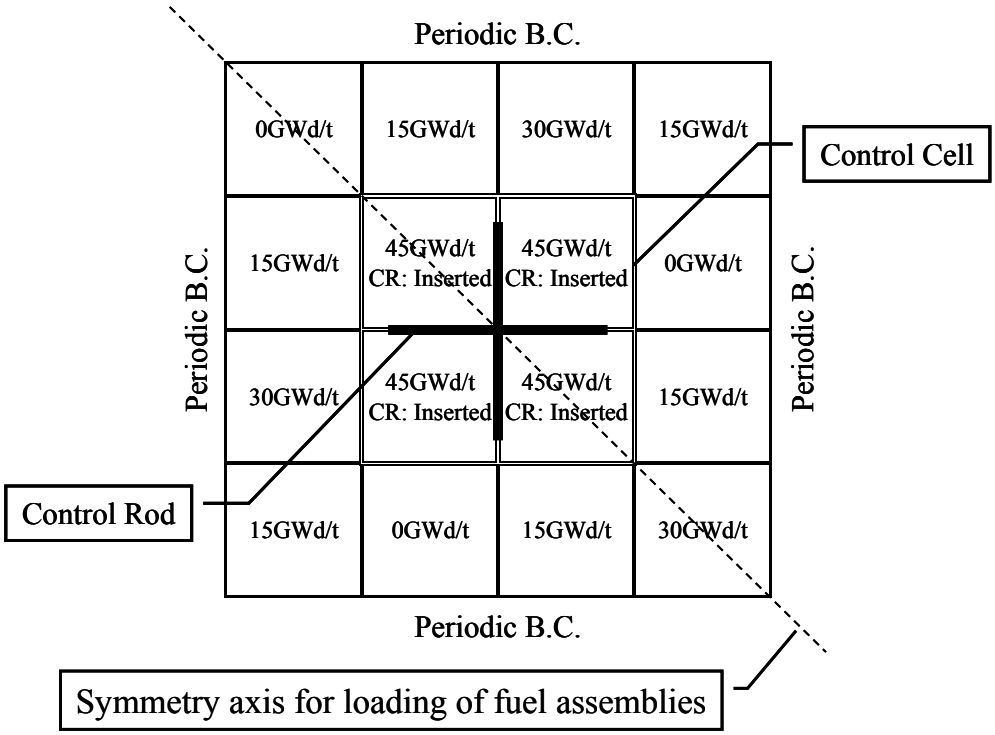

Figure 5.3 Geometry of 4×4 colorset assemblies in Chapter 5

In Figure 5.3, the 2×2 fuel assemblies, which are located in the center of 4×4 colorset assembly geometry, simulate a control cell and have the same specifications (*i.e.*, the assembly-averaged exposure and the type of fuel assembly are the same). For other fuel assemblies loaded around the control cell, the assembly-averaged exposures are fixed as shown in Figure 5.3 and the types of fuel assemblies are randomly determined considering the diagonal symmetry of 4×4 colorset assembly geometry. Through these procedures, I determine approximately 6,500 patterns of 4×4 colorset assembly geometries, which are combinations of three types of fuel assemblies for the control cell and surrounding seven assemblies (*i.e.*, 3^8 patterns). The assembly-averaged void fraction is 40%, which is an average value of void fraction in actual BWR cores. It should be reminded that consideration of an in-channel void distribution is beyond the scope of this Chapter as described previously. Since I assume that the cycle length is 15GWd/t and consider the loading pattern of fuel assemblies in the beginning of cycle, the assembly-averaged exposure is chosen from 0, 15, 30, or 45GWd/t.

Note that the above calculation conditions are the same with those described in Chapter 4.

5.3.2. Verification procedure to correct coarse group cross sections

In the present LI correction technique with the SPH factor or the DF, the coarse group cross sections are corrected by the following procedures. Note that the SPH factor and the DF are not corrected (*i.e.*, those calculated in single assembly geometries are used).

(1) Single assembly calculations in coarse group are carried out for all types of fuel assemblies. Through such single assembly calculations, the $LI_{m,G}^{single}$ in Equation (5.4) is calculated.

(2) Target 4×4 colorset assembly calculation in coarse group is carried out with the uncorrected coarse group cross sections and the SPH factor or the DF, which are obtained in single assembly geometries. The LIs in the target 4×4 colorset assembly geometries are calculated using the neutron fluxes and the k-effective obtained in this step.

(3) Based on Equation (5.4), the corrections of coarse group cross sections are estimated using the LIs obtained in the steps (1) and (2) and the coupling coefficients of LIs pre-calculated in the section 5.2.2.

(4) Target 4×4 colorset assembly calculation in coarse group is carried out with the corrected coarse group cross sections obtained in the step (3) and the SPH factor or the DF. The LIs

are updated using the neutron fluxes and the k-effective of target 4×4 colorset assembly calculation.

(5) The steps (3) and (4) are repeated until the k-infinity and the pin-by-pin fission rate distribution of the target 4×4 colorset assembly calculation are converged.

As shown in the above, the iteration of core calculations is necessary in order to correct the coarse group cross sections by the present LI correction technique. In actual core analysis, cross sections are also corrected by the thermal-hydraulic feedback effect. The coarse group cross sections can be simultaneously corrected by the present LI correction technique and the thermal-hydraulic feedback effect and thus the computational time would not be significantly increased even if present LI correction technique is applied. Also note that the number of iterations required for the present LI correction technique with the SPH factor and that with the DF are comparable, which is confirmed through the verification calculations described in the next section.

5.3.3. Verification results and remarks

5.3.3.1. Impact of LI correction technique, SPH factor, and DF

In general, in order to reproduce heterogeneous fine group calculations by homogeneous coarse group calculations, the spatial homogenization and the energy collapsing errors should be taken into account as shown in **Figure 5.4**.

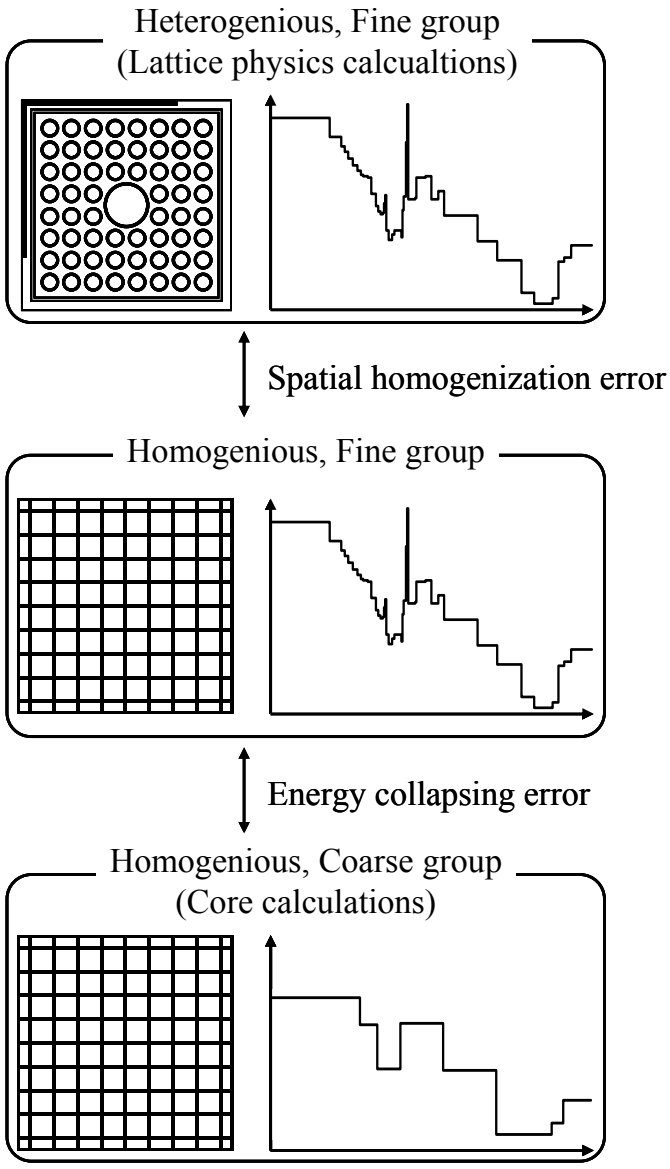

Figure 5.4 Treatments of spatial and energy dependences in lattice physics and core calculations

However, in this Chapter, I only focus on the reduction of energy collapsing error. Reduction of the spatial homogenization error is out of the scope of this Chapter. Therefore, in the present verifications, the pin-averaged 47-group cross sections obtained by the HELIOS code in single assembly geometries are used as the reference cross sections, which corresponds to the middle part in Figure 5.4. Moreover, the core calculations are performed with the pin-averaged 4- or 8-group cross sections, which correspond to the lower part in Figure 5.4. In this context, the direct comparison with the HELIOS calculations (*i.e.*, the upper part in Figure 5.4) would be an open issue to be addressed in future work. For the fine group (47-group) and the coarse group (4- or 8-group) calculations, the diffusion method is used.

In order to discuss the impacts of the LI correction technique, the SPH factor, and the DF, I compare the k-infinities and the pin-by-pin fission rate distributions on several 4×4 colorset assembly geometries. The pin-by-pin (cell-homogenized) calculations in the single and the colorset assembly geometries are performed by the diffusion method, in which the finite difference method is used for the spatial discretization. The present spatial discretization method would be different from typical pin-by-pin calculation method. However, in general, spatial discretization error is not very large in a pin-by-pin calculation since spatial mesh size is small. Therefore, the difference of spatial discretization method would not have significant impact on the calculation results. However, confirmation on this issue will be desirable as a future study.

The absolute value of relative difference of k-infinity and the root-mean-square (RMS) difference of pin-by-pin fission rate distribution are calculated as:

$$\Delta k_{inf} = \left| \frac{k_{inf}^{calculated} - k_{inf}^{reference}}{k_{inf}^{reference}} \right|, \tag{5.9}$$

$$\Delta R_{f,RMS} = \sqrt{\frac{\sum_{m \in fuel\,mesh} \left(R_{f,m}^{calculated} - R_{f,m}^{reference} \right)^2}{N_{fuel\,mesh}}}, \tag{5.10}$$

where Δk_{inf}, $\Delta R_{f,RMS}$, $R_{f,m}$, and $N_{fuel\ mesh}$ are the absolute value of relative difference of k-infinity, the RMS difference of pin-by-pin fission rate distribution, the pin-by-pin fission rate on fuel mesh m, and the total number of fuel meshes, respectively. The superscript *calculated* represents the calculations with the coarse group cross sections corrected (or not corrected) by the present LI correction technique with the SPH factor or the DF. The superscript *reference* represents those with the reference cross sections. Note that the reference cross sections have been corrected by the SPH method in order to reduce the spatial homogenization errors in single assembly geometries.

In the present verifications, the six types of calculation results in **Table 5-2** are compared with the reference calculation results (*i.e.*, the 47-group calculation results).

Table 5-2 Types of calculation results used in present verifications

	LI correction technique	SPH factor	DF
None	×	×	×
LI	○	×	×
SPH	×	○	×
DF	×	×	○
LI+SPH	○	○	×
LI+DF	○	×	○

×: not applied, ○: applied

The absolute value of relative difference of k-infinities and the RMS difference of pin-by-pin fission rate distributions are summarized in **Tables 5-3** and **5-4**. These are calculated in approximately 6,500 patterns of 4×4 colorset assembly geometries with 4- and 8-group cross sections.

Table 5-3 Summary of 4-group calculation results considering errors due to spectral interference effect and energy collapsing

Control Rod: Withdrawn		None	LI	SPH	DF	LI+SPH	LI+DF
Δk_{inf} [pcm]	Average	106	87	57	44	37	20
	Maximum	403	310	172	142	81	45
$\Delta R_{f,RMS}$ [%]	Average	1.19	1.01	0.77	0.59	0.49	0.26
	Maximum	1.51	1.16	1.28	1.01	0.82	0.47
Control Rod: Inserted		None	LI	SPH	DF	LI+SPH	LI+DF
Δk_{inf} [pcm]	Average	137	95	100	89	46	31
	Maximum	465	328	221	196	90	63
$\Delta R_{f,RMS}$ [%]	Average	1.28	1.06	0.85	0.71	0.53	0.33
	Maximum	1.60	1.23	1.37	1.12	0.86	0.58

Table 5-4 Summary of 8-group calculation results considering errors due to spectral interference effect and energy collapsing

Control Rod: Withdrawn		None	LI	SPH	DF	LI+SPH	LI+DF
Δk_{inf} [pcm]	Average	29	33	14	16	8	3
	Maximum	135	110	60	70	24	8
$\Delta R_{f,RMS}$ [%]	Average	0.59	0.50	0.29	0.30	0.20	0.07
	Maximum	0.78	0.63	0.45	0.52	0.35	0.13
Control Rod: Inserted		None	LI	SPH	DF	LI+SPH	LI+DF
Δk_{inf} [pcm]	Average	36	38	13	13	6	6
	Maximum	151	115	62	70	24	12
$\Delta R_{f,RMS}$ [%]	Average	0.62	0.52	0.31	0.35	0.21	0.08
	Maximum	0.82	0.65	0.48	0.55	0.35	0.14

From Tables 5-3 and 5-4, the impacts of the LI correction technique, the SPH factor, and the DF can be discussed.

Firstly, the impact of the LI correction technique is discussed from the comparison of “None” and “LI”. In this comparison, only the error due to the spectral interference effect on coarse group cross sections is focused. For the 4-group calculation, the calculation accuracies of the k-infinity and the pin-by-pin fission rate distribution are improved. On the other hand, for 8-group calculations, the average values of difference of k-infinity become large by the LI correction technique. In order to discuss the reasons for the above observations, I confirm the verification results in Chapter 4. In Chapter 4, the same two dimensional benchmark problems are carried out though the reference calculation results are calculated with the coarse group cross sections, which are obtained by direct collapsing of fine group cross sections in the target colorset assembly geometry. The absolute value of relative difference of k-infinities and the RMS difference of pin-by-pin fission rate distributions are shown in **Tables 5-5** and **5-6**, which are described in Chapter 4.

Table 5-5 Summary of 4-group calculation results only considering spectral interference effect in Chapter 4

Control Rod: Withdrawn		None	LI
Δk_{inf} [pcm]	Average	40	20
	Maximum	143	48
$\Delta R_{f,RMS}$ [%]	Average	0.48	0.13
	Maximum	0.79	0.23
Control Rod: Inserted		None	LI
Δk_{inf} [pcm]	Average	75	23
	Maximum	187	52
$\Delta R_{f,RMS}$ [%]	Average	0.55	0.16
	Maximum	0.86	0.28

Table 5-6 Summary of 8-group calculation results only considering spectral interference effect in Chapter 4

Control Rod: Withdrawn		None	LI
Δk_{inf} [pcm]	Average	17	1
	Maximum	72	4
$\Delta R_{f,RMS}$ [%]	Average	0.29	0.02
	Maximum	0.51	0.04
Control Rod: Inserted		None	LI
Δk_{inf} [pcm]	Average	13	1
	Maximum	73	5
$\Delta R_{f,RMS}$ [%]	Average	0.33	0.02
	Maximum	0.54	0.04

From Tables 5-5 and 5-6, the calculation accuracies of the k-infinity and the pin-by-pin fission rate distribution are improved by the LI correction technique both for 4- and 8-group calculations.

However, by comparing Tables 5-3 to 5-6, the improvements of calculation accuracies in Tables 5-3 and 5-4 are smaller than those in Tables 5-5 and 5-6. Only the error due to the spectral interference effect on coarse group cross sections is included in the "None" of Tables 5-5 and 5-6. On the contrary, the errors due to the spectral interference effect on coarse group cross sections and the energy collapsing are included in "None" of Tables 5-3 and 5-4. Since these two errors (*i.e.*, the spectral interference effect and the energy collapsing) would cancel each other, "None" of Tables 5-3 and 5-4 would show smaller error. Therefore, improvement of calculation accuracies in Tables 5-3 and 5-4 are smaller than those in Tables 5-5 and 5-6. More detail discussion on this matter (cancellation of errors) will be described in section 5.3.3.2.

Secondly, through the comparisons between "None", "SPH", and "DF", the impacts of the SPH factor and the DF are discussed. In these comparisons, only the error due to the energy collapsing of cross sections is focused. For both of 4- and 8-group calculations in Tables 5-3 and 5-4, the calculation accuracies are improved by the SPH factor or the DF. Moreover, the improvements of calculation accuracies by the SPH factor and the DF are similar. Thus, the SPH factor and the DF, which are calculated in single assembly geometries, can consistently remove the energy collapsing errors in colorset assembly geometries.

Finally, the applicability of the present LI correction technique with the SPH factor or the DF is discussed. The differences in "LI+SPH" become smaller than those in "None", "LI", and "SPH". The improvements of calculation accuracies by "LI+SPH" are approximately equal to the summation of those by "LI" and "SPH". Thus, "LI+SPH" can efficiently remove both of the errors due to the spectral interference effect on coarse group cross sections and the energy collapsing. Moreover, the combination of the LI correction technique with the SPH factor does not offset the improvements of calculation accuracies obtained by each correction technique. Similarly tendencies are observed among "None", "LI", "DF", and "LI+DF". Thus, "LI+DF" (i.e., the present LI correction technique with the DF) also can remove both of the errors due to the spectral interference effect on coarse group cross sections and the energy collapsing without the cancellation of these correction performances. From the comparisons of "LI+SPH" and "LI+DF", the difference of k-infinity by "LI+DF" is smaller than that by "LI+SPH" and the difference of pin-by-pin fission rate distribution by "LI+SPH" is approximately a few times larger than that by "LI+DF". Therefore, "LI+DF" reproduces the reference calculation results better than

"LI+SPH". The reason for this difference is discussed in the next section.

Using the calculation results shown in Tables 5-3 to 5-6, breakdown of differences between the reference fine group and the coarse group calculations are analyzed as shown in **Tables 5-7** and **5-8**.

Table 5-7 Breakdown of calculation errors by LI correction technique, SPH factor, and DF in 4-group

Control Rod: Withdrawn	Total	Spectral interference effect		Energy collapsing		
		Uncorrected	With correction by LI	Uncorrected	With correction by SPH	With correction by DF
Δk_{inf} [pcm]	106	40	20	66	17	0
$\Delta R_{f,RMS}$ [%]	1.19	0.48	0.13	0.71	0.36	0.13
Control Rod: Inserted	Total	Spectral interference effect		Energy collapsing		
		Uncorrected	With correction by LI	Uncorrected	With correction by SPH	With correction by DF
Δk_{inf} [pcm]	137	75	23	62	23	8
$\Delta R_{f,RMS}$ [%]	1.28	0.55	0.16	0.73	0.37	0.17

Table 5-8 Breakdown of calculation errors by LI correction technique, SPH factor, and DF in 8-group

Control Rod: Withdrawn	Total	Spectral interference effect		Energy collapsing		
		Uncorrected	With correction by LI	Uncorrected	With correction by SPH	With correction by DF
Δk_{inf} [pcm]	29	17	1	12	7	2
$\Delta R_{f,RMS}$ [%]	0.59	0.29	0.02	0.30	0.18	0.05
Control Rod: Inserted	**Total**	**Spectral interference effect**		**Energy collapsing**		
		Uncorrected	With correction by LI	Uncorrected	With correction by SPH	With correction by DF
Δk_{inf} [pcm]	36	13	1	23	5	5
$\Delta R_{f,RMS}$ [%]	0.62	0.33	0.02	0.29	0.19	0.06

Values shown in Tables 5-7 and 5-8 are estimated by the averaged differences of k-infinity and pin-by-pin fission rate distribution, which are represented as “Average” in Tables 5-3 to 5-6. Details of estimations are described as follows:

(1) Total differences between the reference fine group and the coarse group calculations are represented as “Total”, which correspond to “None” in Tables 5-3 and 5-4.

(2) Errors due to the spectral interference effect on coarse group cross sections are represented as “Uncorrected” in “Spectral interference effect”, which correspond to “None” in Tables 5-5 and 5-6.

(3) Residual errors after the LI correction are represented as “With correction by LI”. These values correspond to “LI” in Tables 5-5 and 5-6.

(4) Errors due to the energy collapsing are represented as “Uncorrected” in “Energy collapsing”, which are calculated by subtracting “Uncorrected” in “Spectral interference effect” from

"Total".

(5) Residual errors after the SPH correction are represented as "With correction by SPH". These values are calculated by subtracting "LI" in Tables 5-5 and 5-6 from "LI+SPH" in Tables 5-3 and 5-4.

(6) Residual errors after the DF correction are represented as "With correction by DF". These values are calculated by subtracting "LI" in Tables 5-3 and 5-4 from "LI+DF" in Tables 5-3 and 5-4.

The errors due to the spectral interference effect on coarse group cross sections and the energy collapsing are not generally independent. Moreover, they would cancel out each other as described previously. Thus, the breakdown in Tables 5-7 and 5-8 cannot be rigorously estimated. However, in this Chapter, I approximately estimate the breakdown of errors in Tables 5-3 and 5-4 in order to compare the performances of improvements of calculation accuracies by each correction technique.

From Tables 5-3 and 5-4, firstly, the errors due to the spectral interference effect on coarse group cross sections (*i.e.*, "Uncorrected" in "Spectral interference effect") are reduced by the LI correction technique. The degree of freedom for the LI correction technique in 8-group is greater than that in 4-group, which can be found from Equation (5.3) and is also discussed in Chapter 4. Thus, as the number of energy group becomes larger, the residual errors after the LI correction (*i.e.*, "With correction by LI") become smaller. Next, the errors due to the energy collapsing (*i.e.*, "Uncorrected" in "Energy collapsing") are removed by the SPH factor or the DF. Similar to the above, the residual errors (*i.e.*, "With correction by SPH" or "With correction by DF") become smaller when the number of energy group becomes larger. In this Chapter, the SPH factor and the DF, which are calculated in single assembly geometries, are used in colorset assembly geometries. Namely, the variations of the SPH factor and the DF due to the spectral interference effect are assumed to be small in this Chapter. Since the impact of this assumption in 4-group calculations typically becomes larger than that in 8-group calculations, the SPH factor and the DF obtained in single assembly geometries would show better performance as the number of energy group becomes larger.

In 4-group calculations, the improvements by the SPH factor are approximately 60 to 70% of those by the DF as shown in Table 5-7. Moreover, in 8-group calculations shown in Table 5-8, the improvements by the SPH factor are approximately 50% of those by the DF. In other words, the DF

shows better performance than the SPH factor. The reason is discussed in the next section together with the reason for better performance of "LI+DF" than "LI+SPH" in Tables 5-3 and 5-4.

5.3.3.2. Comparisons of detailed pin-by-pin fission rate distribution

In order to discuss the improvements of calculation accuracies by the LI correction technique, the SPH factor, and the DF in more detail, I compare the pin-by-pin fission rate distributions on 2×2 colorset assembly geometry with the periodic boundary condition shown in **Figure 5.5**. I use the 2×2 colorset assembly geometry shown in Figure 5.5 in this section for simplicity.

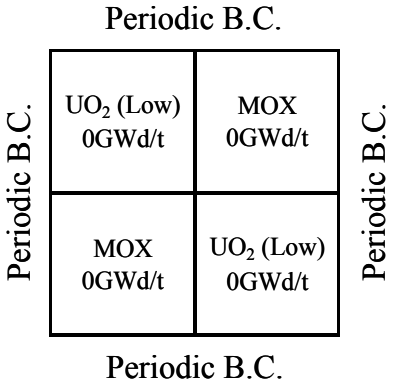

Figure 5.5 Geometry of 2×2 colorset assemblies

As shown in Figure 5.5, the 2×2 colorset assembly geometry consists of the low-enrichment UO_2 (1.0wt% ^{235}U) and the MOX (4.0wt% Pu-fissile) fuel assemblies, in which large spectral interference effect can be observed. In the 2×2 colorset assembly geometry, the control rod is withdrawn and the assembly-averaged exposure is 0GWd/t. Thus, the RMS differences of pin-by-pin fission rate distribution in the 2×2 colorset assembly geometry, which are shown in latter, become larger than those in the 4×4 colorset assembly geometry shown in Tables 5-3 and 5-4. The energy collapsing of cross sections from 47 to 8 energy groups is considered.

Firstly, I discuss that the improvements of calculation accuracies in Tables 5-3 and 5-4 are smaller than those in Tables 5-5 and 5-6. The following four types of difference of pin-by-pin fission rate distribution are discussed in order to address the differences in calculation accuracies.

Case 1 Difference of "None" in Tables 5-5 and 5-6.

Case 2 Difference of "LI" in Tables 5-5 and 5-6.

Case 3 Difference of “None” in Tables 5-3 and 5-4.

Case 4 Difference of “LI” in Tables 5-3 and 5-4.

It would be reminded that only errors of coarse group cross sections due to the spectral interaction are included in Tables 5-5 and 5-6, but not only errors of coarse group cross sections due to the spectral interaction but also errors due to the energy collapsing are also included in Tables 5-3 and 5-4. These calculation results are shown in **Figures 5.6** and **5.7**. Note that the reference calculation results used in “Case 1” and “Case 2” (*i.e.*, “Reference fission rate” in Figure 5.6) are obtained with the reference coarse group cross sections and those used in “Case 3” and “Case 4” (*i.e.*, “Reference fission rate” in Figure 5.7) are obtained with the reference fine group cross sections, respectively.

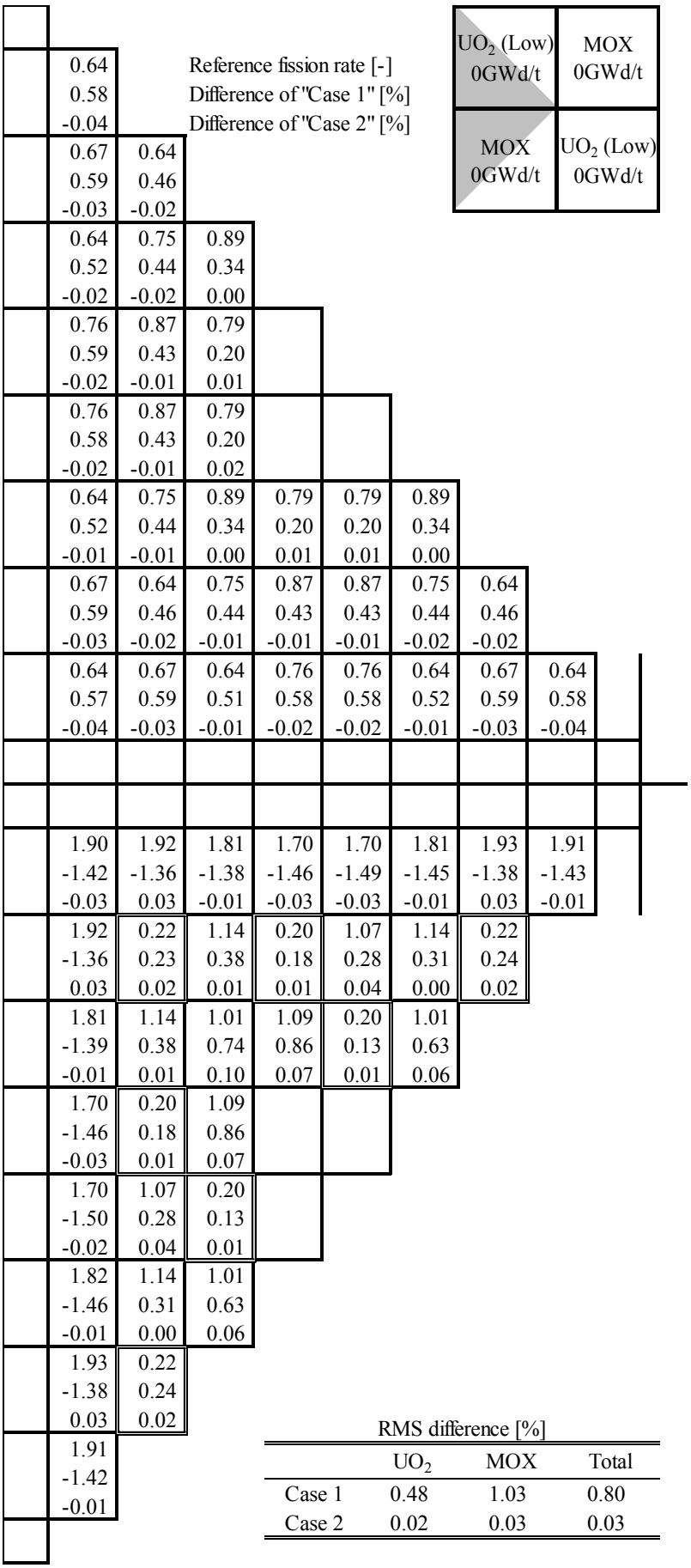

Figure 5.6 Difference of pin-by-pin fission rate distribution (Cases 1 and 2)

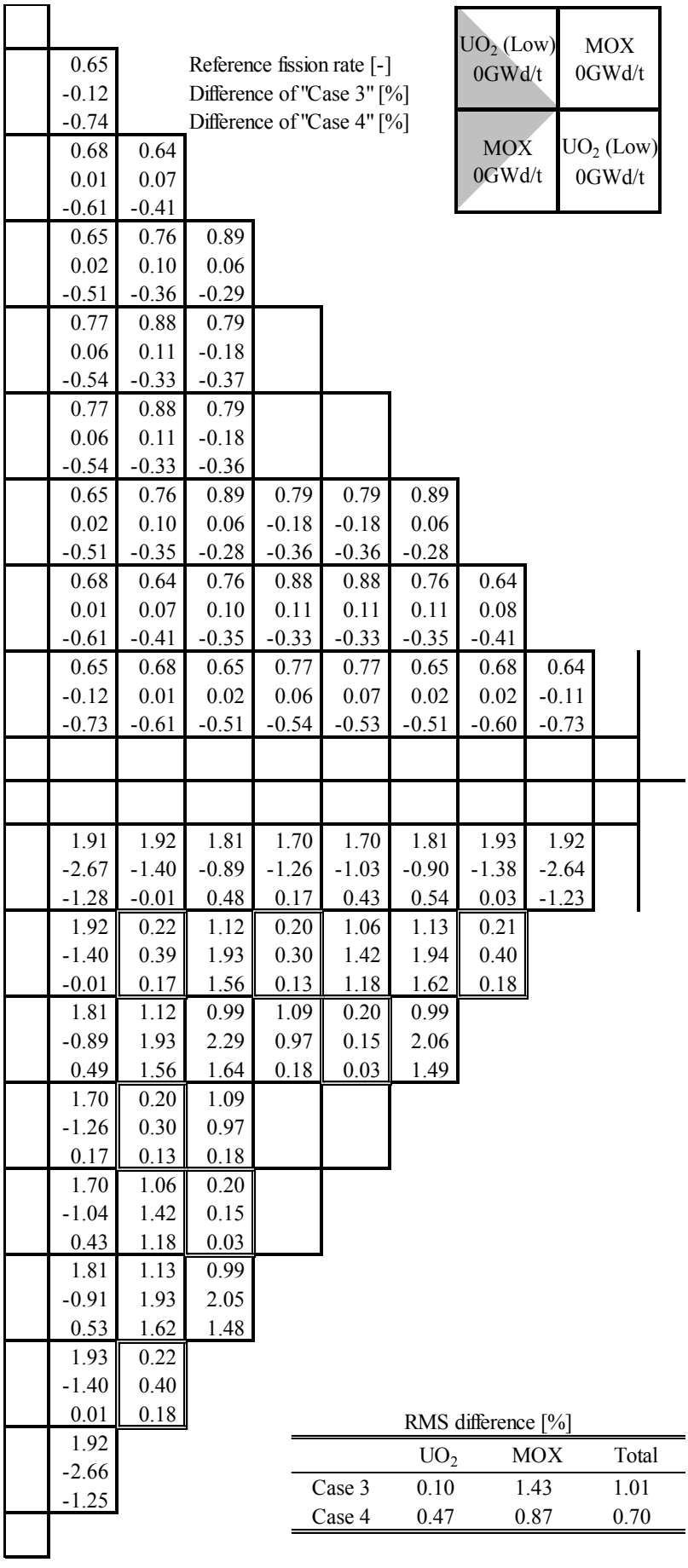

RMS difference [%]

	UO_2	MOX	Total
Case 3	0.10	1.43	1.01
Case 4	0.47	0.87	0.70

Figure 5.7 Difference of pin-by-pin fission rate distribution (Cases 3 and 4)

In Figure 5.6, from the comparison of “Case 1” and “Case 2”, the differences due to the spectral interference effect on coarse group cross sections are mainly observed in the assembly peripheral regions and they are reduced by the LI correction technique on both of UO_2 and MOX fuel assemblies. On the other hand, while the RMS difference on MOX fuel assemblies in “Case 3” becomes larger than that in “Case 4”, the RMS difference on UO_2 fuel assemblies in “Case 3” becomes smaller than that in “Caser 4” in Figure 5.7. From this result, in UO_2 fuel assemblies, errors due to the spectral interference effect on coarse group cross sections and the energy collapsing would cancel out each other. This cancellation is also confirmed by the comparison of “Case 1”, “Case 2”, and the differences of “SPH” and “DF” in Tables 5-3 and 5-4. In UO_2 fuel assemblies, though the differences of pin-by-pin fission rates of “Case 2” generally show negative values, those of “SPH” and “DF” in Tables 5-3 and 5-4 show positive values. Thus, the errors due to the spectral interference effect on coarse group cross sections and the energy collapsing cancel out each other. Let us focus on the differences of several meshes located around Gd-bearing fuels framed by double line in MOX fuel assemblies. Improvements of these differences in Figure 5.7 become smaller than those in Figure 5.6. Namely, the several meshes located around the Gd-bearing fuels would have larger impact by the energy collapsing error than other meshes. Therefore, the improvements of calculation accuracies by the LI correction technique in Tables 5-3 and 5-4 become smaller than those in Tables 5-5 and 5-6. Similar tendencies caused on fuel meshes located around the Gd-bearing fuels are observed in other 2×2 colorset assembly geometries (*e.g.*, 2×2 colorset assembly geometries, which consist of the low-enrichment and the high-enrichment UO_2 fuel assemblies).

Next, I discuss that the LI correction technique with the DF performs better than the LI correction technique with the SPH factor in Tables 5-3 and 5-4. I compare the following two types of difference of pin-by-pin fission rate distribution in addition to “Case 3” and “Case 4” as described the above. By comparing the four types of differences, I address the difference in the performances of the SPH factor and the DF.

Case 5　Difference of “LI+SPH” in Tables 5-3 and 5-4.

Case 6　Difference of “LI+DF” in Tables 5-3 and 5-4.

These calculation results are shown in **Figure 5.8**. Note that the reference calculation results used in the above two cases (*i.e.*, “Reference fission rate” in Figure 5.8) are obtained with the reference fine group cross sections.

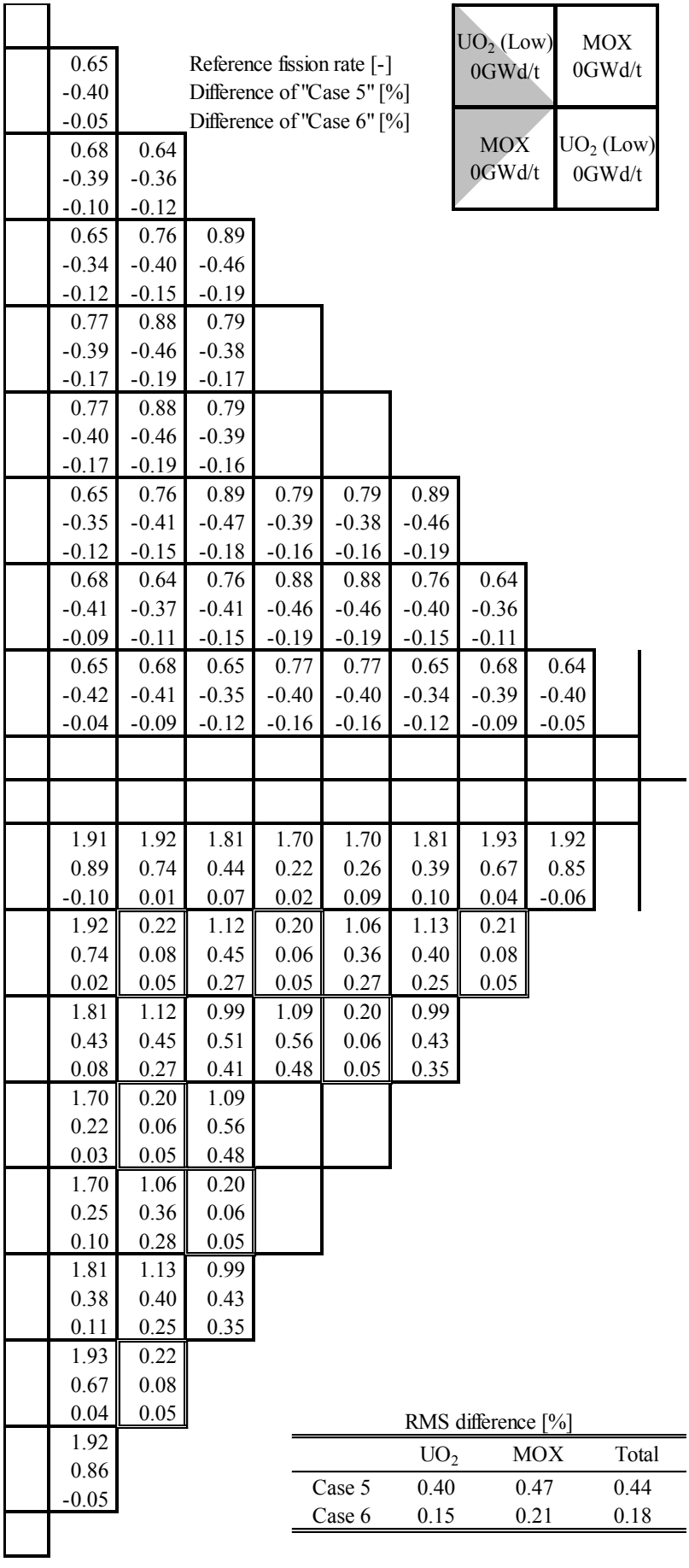

RMS difference [%]

	UO_2	MOX	Total
Case 5	0.40	0.47	0.44
Case 6	0.15	0.21	0.18

Figure 5.8 Difference of pin-by-pin fission rate distribution (Cases 5 and 6)

From the comparison among “Case 3”, “Case 4”, and “Case 5”, the calculation accuracies are improved by the SPH factor. Thus, the application of the SPH factor can reduces the errors due to the energy collapsing. By comparing “Case 3”, “Case 4”, and “Case 6”, the differences also become smaller thus the DF also can reduce the energy collapsing errors. Furthermore, the improvements of calculation accuracies in “Case 6” are larger than that in “Case 5” for every fuel meshes.

The assembly-averaged SPH factor, which is calculated in single assembly geometries, is approximately unity [1]. However, in general, that calculated in colorset assembly geometries is different from unity (i.e., the assembly-averaged SPH factor is perturbed by the spectral interference effect). As discussed in the reference [8], even though the spatial shape of pin-by-pin fission rate distribution on each fuel assembly can be approximately reproduced in “Case 5”, the assembly-averaged fission rate distribution cannot be accurately reproduced since the variation of SPH factor due to the spectral interference effect is assumed to be small in this Chapter. Therefore, it is indicated that the LI correction technique with the SPH factor would not be useful to accurately reproduce the calculation results of the reference fine group calculations as long as the variation of SPH factor due to the spectral interference effect is not taken into account.

On the other hand, though the variation of DF due to the spectral interference effect is also assumed to be small, the DF has larger degree of freedom than that of the SPH factor (*i.e.*, the SPH factor and the DF are calculated in each pin-cell mesh and in every surface of pin-cell mesh, respectively). Furthermore, for the spatial homogenization, the DF at the fuel assembly surface depends on the type of fuel assembly. Thus, the “level” of surface flux at the heterogeneous calculations is approximately preserved in the homogeneous calculations by the DF. Similar to the spatial homogenization, for the energy collapsing, the “level” of surface flux at the fine group calculations is approximately preserved in the coarse group calculations by the DF. These would contribute to the robustness of the DF to the spectral interference effect.

From the above discussions, the combination of the LI correction technique with the DF reproduces the reference fine group calculation results better than that of the LI correction technique with the SPH factor. The application of DF for the pin-by-pin core analysis would have difficulty from the viewpoint of the computational load since the DF requires larger memory storage than that of the SPH factor. However, the computational performance becomes higher year by year. In this context,

difficulty on the memory requirement is reducing and the usefulness of the LI correction technique with the DF is increasing from the viewpoint of calculation accuracies.

5.4. Conclusions

In this Chapter, I combine the LI correction technique, which can consider the spectral interference effect on coarse group cross sections, with the SPH factor or the DF, which can reduce the errors due to energy collapsing.

In the LI correction technique, the variations of coarse group cross sections due to the spectral interference effect are represented by the linear combination of variations of coarse group LIs and the reference coarse group cross sections are well reproduced. However, though the reference coarse group calculation results are well reproduced, errors due to the energy collapsing of cross sections still exist (*i.e.*, the reference fine group calculation results are not reproduced). In order to reduce the energy collapsing errors, it is necessary to combine other correction methods to reduce the energy collapsing errors with the LI correction technique. In this Chapter, I focus on the SPH factor and the DF. In general, similar to coarse group cross sections, the SPH factor and the DF are also perturbed by the spectral interference effect in core geometries. However, our investigations suggested that if the variations of SPH factor and DF due to the spectral interference effect are considered in the calculation procedure of LI correction technique, the LI correction technique would be more complicated and become unstable from the viewpoint of numerical calculations. Thus, in this Chapter, the SPH factor and the DF calculated in single assembly geometries are used with the LI correction technique.

In order to verify the combination uses of the LI correction technique, the SPH factor, and the DF, 4×4 colorset assembly calculations including the control cell, which consist of typical BWR fuel assemblies, are carried out. The energy collapsing from 47 to 4 and 8 energy groups is considered. The pin-by-pin fine mesh calculations based on the diffusion theory are performed and the k-infinity and the pin-by-pin fission rate distribution are compared. In the present verification, the calculations results obtained with fine group cell-homogeneous cross sections are considered as the reference. The calculation results indicate that the energy collapsing errors are reduced by the SPH factor or the DF. Moreover, the reference calculation results are well reproduced by the combination of the LI correction technique, the SPH factor, and the DF. The LI correction technique with the SPH factor or the DF shows

similar improvement for the k-infinity. However, from the viewpoint of the pin-by-pin fission rate distribution, the LI correction technique with the DF outperforms the LI correction technique with the SPH factor. Namely, error reduction of “LI+DF” is a few times larger that of “LI+SPH”.

In order to discuss the difference between the SPH factor and the DF, I carry out the 2×2 colorset assembly calculations and compare the pin-by-pin fission rate distribution. The calculation results indicate that though the spatial shape of pin-by-pin fission rate distribution on each fuel assembly can be reproduced in “LI+SPH”, the assembly-averaged fission rate distribution cannot be well reproduced. In general, the assembly-averaged SPH factor calculated in colorset assembly geometries is different from unity due to the spectral interference effect. However, in this Chapter, I use the SPH factor calculated in single assembly geometries and the variation of SPH factor due to the spectral interference effect is assumed to be negligible. Similar to the SPH factor, the variation of the DF due to the spectral interference effect is also assumed to be negligible (i.e., the DF calculated in single assembly geometries is used). However, since the SPH factor and the DF are calculated in each pin-cell mesh and in every surface of pin-cell mesh, respectively, the DF has larger degree of freedom than the SPH factor. Furthermore, since the DF depends on the type of fuel assembly, the “level” of surface flux at the fine group calculations is approximately preserved in the coarse group calculations by the DF (i.e., the DF is more robust over the spectral interference effect than the SPH factor). Therefore, “LI+DF” reproduces the reference calculation results better than “LI+SPH”.

Consequently, the LI correction technique with the DF is useful to capture the spectral interference effect on coarse group cross sections and to reduce the energy collapsing errors on pin-by-pin BWR core analysis.

References

[1] A. Hébert, "A Consistent Technique for the Pin-by-Pin Homogenization of A Pressurized Water Reactor Assembly," *Nucl. Sci. Eng.*, **113**, pp. 227-238, (1991).

[2] K. S. Smith, "Assembly Homogenization Techniques for Light Water Reactor Analysis," *Prog. Nucl. Energy*, **17**, pp. 303-335, (1986).

[3] H. Okuno, Y. Naito, K. Suyama, *OECD/NEA Burnup Credit Criticality Benchmarks Phase IIIB: Burnup Calculations of BWR Fuel Assemblies for Storage and Transport*, JAERI-Research 2002-001, Japan Atomic Energy Research Institute (JAERI), (2002).

[4] A. Yamamoto, T. Ikehara, T. Ito *et al.*, "Benchmark Problem Suite for Reactor Physics Study of LWR Next Generation Fuels," *J. Nucl. Sci. Technol.*, **39**[8], pp. 900-912, (2002).

[5] *HELIOS Methods (Version 1.11)*, Studsvik Scandpower, 2009.

[6] T. Ama, H. Hyoudou, T. Takeda, "Effect of Radial Void Distribution within Fuel Assembly on Assembly Neutronic Characteristics," *J. Nucl. Sci. Technol.*, **39**[1], pp. 90-100, (2002).

[7] T. Kozlowski, T. J. Downar, *PWR MOX/UO_2 Core Transient Benchmark*, NEA/NSC/DOC(2006)20, OECD/NEA, (2007).

[8] A. Yamamoto, M. Tatsumi, Y. Kitamura *et al*, "Improvement of the SPH Method for Pin-by-Pin Core Calculations," *J. Nucl. Sci. Technol.*, **41**[12], pp. 1155-1165, (2004).

Chapter 5 is based on an Accepted Manuscript of an article published by Taylor & Francis in Journal of Nuclear Science and Technology on September 3rd, 2014, available online: http://wwww.tandfonline .com/10.1080/00223131.2014.948520.

Chapter 6. Conclusions

The pin-by-pin fine mesh core calculation method for BWR core analysis has been studied as a candidate of the next generation core analysis method. In this method, since cross sections are homogenized in a fuel pin-cell, the pin-by-pin power distribution can be directly estimated and thus can reduce the error with the homogenization of cross sections. Therefore, the important core parameters, (*e.g.*, power peaking factor), would be more accurately calculated.

However, in order to practically apply the pin-by-pin fine mesh core calculation method for BWR core analysis, there are several unresolved issues from the viewpoints of treatment of cross sections for core analyses, which are evaluated through lattice physics calculations.

In this thesis, the following three topics for the BWR pin-by-pin fine mesh core calculation are studied:

(1) An optimization approach to establish an appropriate energy group structure.

(2) A macroscopic depletion model to tabulate pin-cell averaged cross sections.

(3) A spectral interference correction technique for coarse group cross sections.

(1) An optimization approach to establish an appropriate energy group structure (Chapter 2):

In order to establish an appropriate energy group structure, firstly, I investigate two different methods to establish an appropriate energy group structure (*i.e.*, the successive collapsing and expanding methods), which are based on the steepest descent method. In these methods, energy group boundaries, which provide the n smallest differences of the k-infinity or the pin-by-pin fission rate distribution between the coarse group calculation and the reference (40-group) calculation in the 2×2 multi-assembly, are successively removed or added.

Then, I carry out the sensitivity analyses of these approaches by focusing on the following points:

- Approach to establish energy group structure (collapsing or expanding),
- Optimization index (difference of k-infinity or pin-by-pin fission rate distribution),
- Number of candidates considered in the successive collapsing/expanding procedure.

From the results of the sensitivity analyses, I decide the calculation conditions of the present approach as follows:

- Cross sections are successively collapsed.
- Pin-by-pin fission rate distribution is used as the optimization index.
- Only the best candidate of the energy group structure is considered during the optimization.

On these calculation conditions, I simultaneously apply the present approach to the various spectral interference conditions in order to establish unified coarse energy group structures, which are suitable for BWR pin-by-pin core analysis. Then the performance of the established coarse energy group structures is confirmed through the statistical analyses on the differences of the k-infinity and the pin-by-pin fission rate distribution in the various configurations, which simulate typical BWR core conditions in the beginning of cycle. From the comparison of statistical analysis results with the coarse energy group structure, the calculation accuracies of the 8-group structure determined in this thesis is better than that obtained by the 8-group structure used in the previous study.

Moreover, since the present approach is based on the steepest descent method, energy group structures of arbitrary number of energy groups can be generated. Therefore, the relationship between the number of energy groups and the calculation accuracy is obtained and the number of energy groups and the energy group structure suitable for the pin-by-pin core analysis can be decided considering significant energetic and spatial distribution of neutron spectrum in BWR fuel assemblies due to complicated geometries.

Consequently, the optimization approach in this thesis is useful to establish an appropriate energy group structure for BWR pin-by-pin core analysis.

(2) A macroscopic depletion model to tabulate pin-cell averaged cross sections (Chapter 3):

The macroscopic cross section model for BWR pin-by-pin core analysis is studied. The macroscopic cross sections are basically approximated by a linear combination of those on the base condition and their correction terms to capture the instantaneous and the history effects.

In order to capture the cross term of instantaneous effects among the core state variables, several branch calculations are carried out and are used to calculate the variations of cross sections. In the branch calculations, some core state variables are simultaneously changed from those on the base condition.. For the history effect, the exposure-averaged core state variables are used as the history indices and their cross term effects is discussed similar to those of the instantaneous effect.

Verification calculations are carried out for typical BWR fuel assemblies and the calculation results obtained by the reference and the tabulated cross sections are compared. The reference cross sections are obtained by the lattice physics calculations, in which core state variables are explicitly specified. The tabulated cross sections are reconstructed through the present macroscopic cross section model. Several benchmark calculations

are carried out with the present macroscopic cross section model in order to confirm treatment of exposure and the cross term effects for the instantaneous and the history variables.

Firstly, the treatment of exposure (*i.e.*, the interpolation of macroscopic cross sections by exposure) is discussed. In this study, macroscopic cross sections are interpolated for the exposure using the CSI. From the benchmark calculations results, it is confirmed that the interpolation for exposure using the CSI can well reproduce the target cross sections.

Then, the calculation results obtained by the tabulated cross sections are compared with or without the cross term effect among the core state and the depletion history variables. When the cross term effect among the core state and the depletion history variables is taken into account, the calculation results obtained by the tabulated cross sections achieve the target accuracies on the differences of k-infinity and pin-by-pin fission rate distribution. Thus, the present macroscopic cross section model well reproduces the target (or the reference) cross sections.

The impacts of cross term effects (*e.g.*, the cross term effect among the void fraction and the fuel temperature) are discussed. The impacts of some cross term effects are small or almost zero; thus such cross term effects could be negligible in the present macroscopic cross section model. However, it is confirmed that the cross term effects among the control rod history (or the void history) and other depletion history variables have large impacts. Therefore, the consideration of such cross term effects is crucial in order to accurately reproduce the target cross sections and accurately estimate the k-infinity and the pin-by-pin fission rate distribution.

Consequently, the present cross section model for BWR pin-by-pin core analysis can be a candidate for practical applications on normal operations of BWR.

(3) A spectral interference correction technique for coarse group cross sections (Chapters 4 and 5):

Firstly, in order to propose a new cross section correction technique for the pin-by-pin core calculations considering the spectral interference effect, I focus on the perturbation of neutron leakage and newly introduce the LI. The LI is defined as the macroscopic cross section of volume-averaged neutron leakage value. From theoretical discussion utilizing the generalized perturbation theory suggests that the variations of coarse group cross sections are approximately described as the linear combination of coarse group LIs.

Preliminary calculations are carried out using the new correction technique (*i.e.*, the LI correction technique) in order to verify the reproducibility of reference coarse group cross sections. The reference coarse group cross sections are directly collapsed in colorset assembly geometries.. The verification results indicate that

the calculation accuracies of k-infinity and pin-by-pin fission rate distribution are improved by applying the LI correction technique. Therefore, it is confirmed that the LI correction technique well reproduces the reference coarse group cross sections by considering the spectral interference effect.

Then, I combine the LI correction technique with the SPH factor or the DF in order to reduce the errors due to energy collapsing and to reproduce the fine group calculation results in colorset assembly geometries.

By the LI correction technique, the reference coarse group cross sections are well reproduced. However, though the reference coarse group calculation results are well reproduced, errors due to the energy collapsing of cross sections still exist (*i.e.*, the reference fine group calculation results are not reproduced by the reference coarse group calculations). Thus, I focus on the SPH factor and the DF in order to reduce the errors due to energy collapsing.

In general, similar to coarse group cross sections, the SPH factor and the DF are also perturbed by the spectral interference effect in core geometries. However, our investigations suggested that if the variations of SPH factor and DF due to the spectral interference effect are considered in the calculation procedure of LI correction technique, the LI correction technique would be more complicated and would become unstable from the viewpoint of numerical calculations. Thus, the SPH factor and the DF calculated in single assembly geometries are used with the LI correction technique.

Colorset assembly calculations are carried out in order to verify the reproducibility of reference fine group calculation results in colorset assembly geometries. For the k-infinity, the calculation results indicate that the energy collapsing errors are reduced by the SPH factor or the DF. Moreover, the reference calculation results are well reproduced by the combination of the LI correction technique and the SPH factor or the LI correction technique and the DF. The LI correction technique with the SPH factor or the DF shows similar improvement. However, for the pin-by-pin fission rate distribution, the LI correction technique with the DF outperforms the LI correction technique with the SPH factor. Namely, error reduction of “LI+DF” is a few times larger than that of “LI+SPH”. Therefore, “LI+DF” reproduces the reference calculation results better than “LI+SPH”.

Consequently, the LI correction technique with the DF is useful to capture the spectral interference effect on coarse group cross sections and to reduce the energy collapsing errors on pin-by-pin BWR core analysis. Through the above efforts, the results of this study would contribute the practical utilizations of the pin-by-pin fine mesh core calculation method for BWR core analysis.

Acknowledgement

My heartfelt gratitude goes to my advisor, Professor Akio Yamamoto of Nagoya University, whose precise advice and invaluable suggestions were of inestimable value for my study.

I am really indebt to Emeritus Professor Yoshihiro Yamane and Assistant Professor Tomohiro Endo of Nagoya University for their helpful comments on my study.

I express my thanks to Professor Akira Uritani, Professor Yoshiyuki Tsuji, Associate Professor Takahiro Ito, and Associate Professor Kenichi Watanabe of Nagoya University and Associate Professor Takanori Kitada of Osaka University. Their lots of comments are really helpful for my study.

I would like to thank Dr. Shinya Kosaka, Dr. Go Hirano, and Mr. Kenichiro Nozaki for their helpful suggestions and warm encouragements.

I would also like to thank Dr. Kenichi Tada, Mr. Kazuma Ohori, and Mr. Yuichiro Ban for lots of discussions with them and their warm encouragements.

Finally, I would also like to express my gratitude to my family. Their understanding and generous support make it possible to complete my study.

List of publication

Journal

[1]. **T. Fujita**, K. Tada, T. Endo, A. Yamamoto *et al*, "An Optimization Approach to Establish An Appropriate Energy Group Structure for BWR Pin-by-Pin Core Analysis," *J. Nucl. Sci. Technol.*, **49**[7], pp. 689-707 (2012).

[2]. **T. Fujita**, T. Endo, A. Yamamoto, "A Macroscopic Cross-Section Model for BWR Pin-by-Pin Core Analysis," *J. Nucl. Sci. Technol.*, **51**[3], pp. 282-304 (2014).

[3]. **T. Fujita**, T. Endo, A. Yamamoto, "A New Technique for Spectral Interference Correction on Pin-by-Pin BWR Core Analysis," *J. Nucl. Sci. Technol.*, **51**[6], pp.783-797 (2014).

[4]. **T. Fujita**, T. Endo, A. Yamamoto, "Application of Correction Technique Using Leakage Index Combined with SPH and Discontinuity Factors on Pin-by-Pin BWR Core Analysis," *J. Nucl. Sci. Technol.* [published on online].

Proceeding of international conference

[1]. **T. Fujita**, K, Tada, A. Yamamoto, Y. Yamane *et al*, "Investigation on Macroscopic Cross Section Model for BWR Pin-by-pin Core Analysis," *Proc. Int. Conf. on Physics of Reactors (PHYSOR 2010)*, May 9-14, 2010, Pittsburgh, Pennsylvania, (2010). [CD-ROM].

[2]. **T. Fujita**, K. Otsuka, K. Tada *et al*, "Investigation of Theoretical Approach to Establish Energy Group Structure for BWR Pin-by-Pin Core Analysis," *Trans. Am. Nucl. Soc.*, **103**, pp. 721-723, (2010).

[3]. **T. Fujita**, T. Endo, A. Yamamoto, "Correction of Spectral Interference Effect on Pin-by-Pin BWR Core Analysis," *Trans. Am. Nucl. Soc.*, **107**, pp. 1141-1143, (2012).

[4]. **T. Fujita**, T. Endo, A. Yamamoto, "Correction Technique for Coarse Group Cross Sections Considering Spectral Interference Effect on Pin-by-Pin BWR Core Analysis," *Proc. 2013 Int. Congress on the Advances in Nuclear Power Plants (ICAPP 2013)*, Apr. 14-18, 2013, Jeju, Korea, (2013). [CD-ROM].